Electromechanical Behavior of Relaxor Ferroelectric Crystals

A Thesis
Presented to
The Academic Faculty

by

Tieqi Liu

In Partial Fulfillment
of the Requirements for the Degree
Doctor of Philosophy in Mechanical Engineering

Georgia Institute of Technology
October 2004

Electromechanical Behavior of Relaxor Ferroelectric Crystals

Approved by:

Dr. Christopher S. Lynch, Advisor

Dr. Jianmin Qu

Dr. Kenneth A. Cunefare

Dr. Rosario A. Gerhardt

Dr. D. Stefan Dancila

Date Approved: October 29, 2004

ACKNOWLEDGEMENTS

I am full of gratitude to my advisor, Dr. Christopher S. Lynch, for his invaluable support, guidance and encouragement throughout this research work. It has been my pleasure working with him. I greatly appreciate the time he spent with me in the past few years. I would like to thank Dr. Jianmin Qu, Dr. Kenneth A. Cunefare, Dr. Rosario A. Gerhardt and Dr. D. Stefan Dancila, for their support and insightful suggestions.

Thanks are due to Elizabeth A. McLaughlin *et al.* at Naval Undersea Warfare Center (NUWC) Division Newport for providing important experimental data in Chapter 4 and Chapter 6. Thanks also go to Shan Wan and William S. Oates for their contributions in Chapter 8. I would like to acknowledge the support of TRS Technologies and DARPA/ONR for this research.

I would like to thank my fellow graduate students for their kindness and cooperation. I am grateful to my friends, they have helped me and shared with me a lot in these years. There has been more than fun and joy with them. I am especially indebted to my parents and family for their love and persistent support. Without them I never would have made it through.

TABLE OF CONTENTS

LIST OF TABLES

LIST OF FIGURES

SUMMARY

Single crystals of relaxor ferroelectric $[Pb(Zn_{1/3}Nb_{2/3})O_3]_{(1-x)}$-$[PbTiO_3]_x$ (PZN-xPT) and $[Pb(Mn_{1/3}Nb_{2/3})O_3]_{(1-x)}$-$[PbTiO_3]_x$ (PMN-xPT) exhibit extraordinary electromechanical properties. They are under development for sensors, actuators and transducers. The polarization switching and phase transition behavior of these crystals under external loading are currently under investigation. The primary task of this research is to investigate the nonlinear behavior of relaxor ferroelectric PZN-xPT and PMN-xPT crystals by a combination of experiments and modeling.

Experimental investigation elucidates the polarization switching and phase transition behavior of relaxor ferroelectric crystals at different orientation cuts under different temperature, electric field and stress loading. <001> and <110> oriented rhombohedral relaxor single crystal properties have been measured. External fields including temperature, stress and electric field all strongly affect the poling and phase states of the crystals. Fracture behavior of relaxor single crystals under non-uniform electric fields at a partial electrode edge has also been measured and analyzed.

Based on experimental investigation, crystal variant based modeling is developed to compute the physical properties of multi-domain crystals at different orientation cuts from a set of properties for the single domain. Experimental measurements provide data for thermodynamics analysis of the polarization switching and phase transitions of relaxor ferroelectric single crystals. Work-energy analysis of field induced phase transitions sheds light on the mechanism of structural phase transitions of these crystals.

This leads to an energy based phase transition criterion, which is not only essential for theoretical modeling, but also desirable for directing experimental investigation.

The results of this research provide an improved understanding of field induced polarization switching and phase transition behavior of relaxor ferroelectric crystals. The crystal variant modeling and thermodynamics analysis give theoretical insight and numerical capability for future research and applications of ferroelectric materials. By including polarization switching and phase transition criteria, the crystal variant modeling leads to a mesoscopic constitutive model for the nonlinear behavior of ferroelectric single crystals. Such a model can be implemented in finite element codes as a numerical tool to simulate, predict and design engineered multi-domain ferroelectric materials.

Keywords: piezoelectric, relaxor ferroelectric, single crystals, PZN-PT, PMN-PT, polarization, phase transition.

CHAPTER 1

INTRODUCTION

Piezoelectrics are crystalline materials that exhibit an electromechanical coupling effect. Common piezoelectric materials include quartz, barium-titanate ($BaTiO_3$), lead-titanate ($PbTiO_3$) and lead-zirconate-titanate (PZT). They are widely used in sensors, actuators and transducers, converting mechanical energy to electrical energy and vice versa (Figure 1-1). The direct piezoelectric effect is used to generate an electrical voltage from mechanical stress (generator), and the converse piezoelectric effect is used to generate mechanical movement by the application of an electric field (motor) [1]. For example, piezoelectric microphones and pickups for electrically amplified guitars turn an acoustical pressure into a voltage, while piezoelectric speakers in electronic devices and computers turn voltage into beeps. In this chapter the basics of piezoelectrics and ferroelectrics, their history and applications, the features of relaxor based ferroelectric single crystals and the contents of this dissertation are introduced.

1.1 Piezoelectric and Ferroelectric Materials

1.1.1 Piezoelectricity

Piezoelectricity was discovered by Pierre and Jacques Curie (Curie brothers) in 1880 [2]. Then In 1881, the converse piezoelectric effect was first predicted by Lippmann

based on thermodynamic principles and soon verified by the Curie brothers. “Piezo” is derived from the Greek word for pressure. Piezoelectricity is usually described as the generation of electricity as a result of mechanical pressure. It was defined by W. Hankel in 1881 as “electric polarization produced by mechanical strain in crystals belonging to certain class, with the polarization being proportional to the strain and changing sign with it”. Electric polarization can be reflected by surface charge.

Piezoelectricity is attributed to the lack of a center of symmetry of the crystallographic unit cell [1,3]. Deformation of such a unit cell leads to formation of polarization. Figure 1-2 provides an explanation of why the piezoelectric effect exists. In Figure 1-2a, deformation of a unit cell with a center of symmetry does not induce polarization. In Figure 1-2b, relative displacements of the ions under stress leads to a net polarization. Application of an electric field also induces deformation of such a unit cell (the converse piezoelectric effect). Note that of the 21 classes that do not possess a center of symmetry, 20 are piezoelectric but one is not piezoelectric because of the combination of other symmetry elements.

Quartz (SiO_2) is one of the most important natural piezoelectric crystals. It is a common mineral (Figure 1-3a) covering nearly 25% of the Earth's surface. Due to the converse piezoelectric effect, quartz vibrates when an alternating electrical current is applied to it, therefore it can be used for oscillators and resonators. In Quartz clocks a combination of direct and converse piezoelectricity is used to generate a regularly timed series of electrical pulses. Figure 1-3b is a picture of man-made PZN-9.5%PT single crystals [4] with ultrahigh piezoelectric effect.

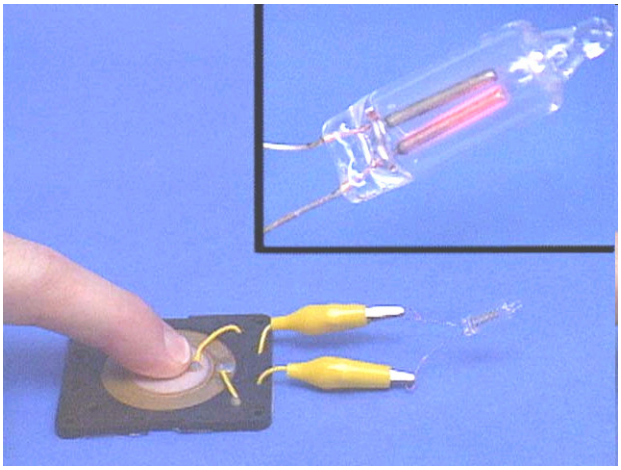

(a)

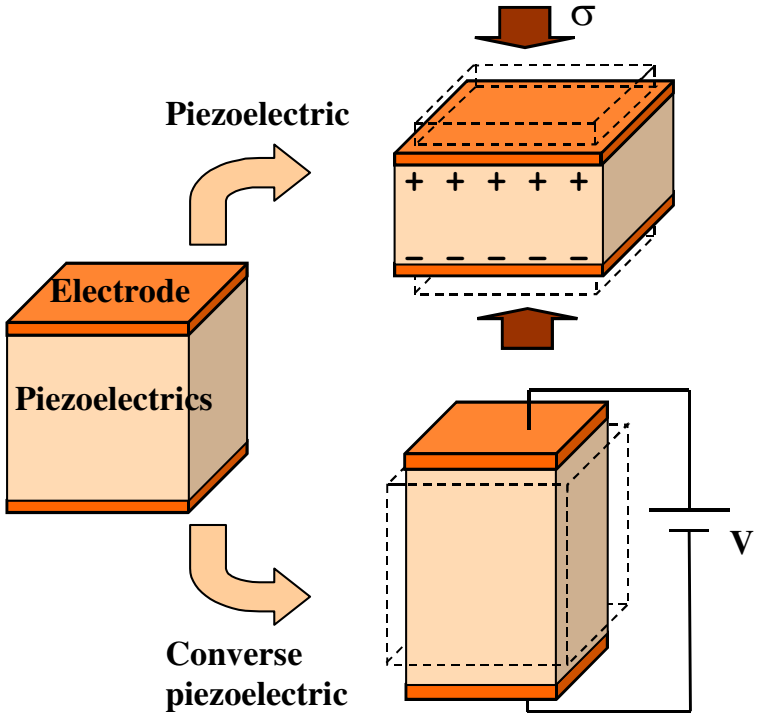

(b)

Figure 1-1. Direct and converse piezoelectric effect. (a) The direct piezoelectric effect (Division of Chemical Education, Inc., American Chemical Society); (b) Illustration of the electromechanical coupling in piezoelectric materials.

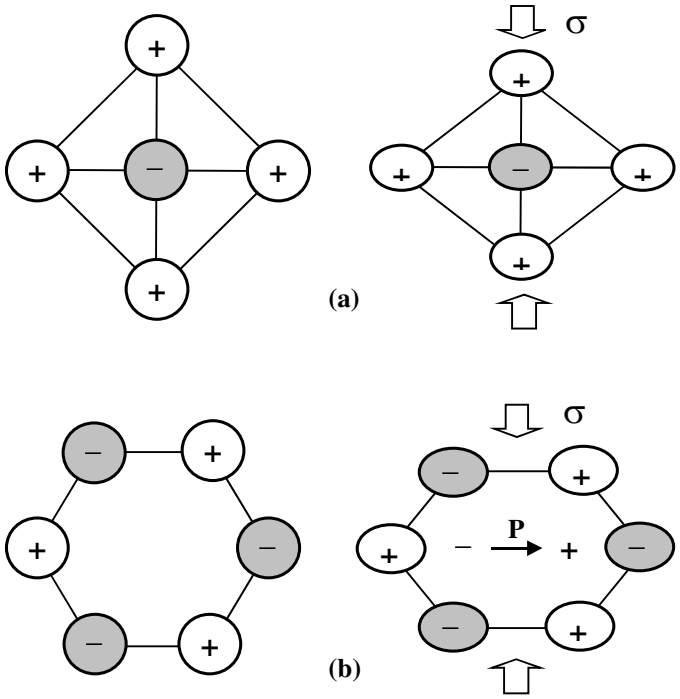

Figure 1-2. Origin of piezoelectricity. (a) No piezoelectric effect with a centrosymmetric unit cell; (b) Piezoelectric due to a lack of center of symmetry.

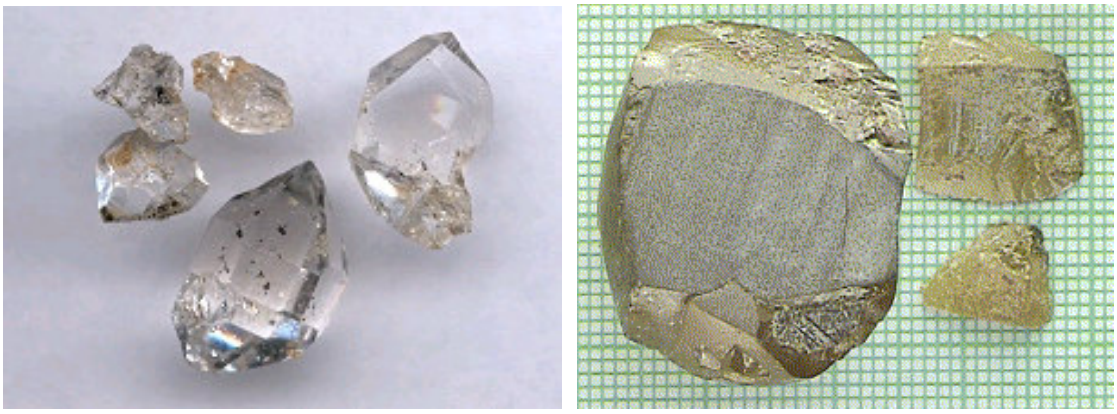

(a) (b)

Figure 1-3. Piezoelectric crystals. (a) Naturally grown Quartz (About.com, Inc.); (b) Man-made PZN-9.5%PT (on 1 mm × 1 mm) grown by the gradient cooling method [4].

A small strain of quartz can produce a very high voltage or electric field. Conversely, an electric field of 1 MV/m applied on quartz produces a strain of only 10^{-6}. Most piezoelectric materials in applications provide much larger piezoelectric strain, which is one of the key achievements of piezoelectric material development. The direct and converse piezoelectric effects are typically linear and reversible.

Besides single crystals and ceramics, the piezoelectric effect also exists in some kinds of polymers (piezoelectric polymers). In piezoelectric polymers there are groups of molecules linked as orderly crystallites. Piezoelectricity is found in many polymer materials including rubber, wool, hair, wood fiber and silk. Polyvinylidene fluoride (PVDF) is the most common piezoelectric polymer material for sensor and transducer applications [5].

1.1.2 Ferroelectricity

Ferroelectrics are a special subset of piezoelectric materials. They exhibit a spontaneous polarization that can be reversed or reoriented (by application of stress or electric field). Most popular piezoelectric ceramics are ferroelectrics. They are very attractive because of their switchable polarizations. Ferroelectric ceramics have been widely used as transducers. Some materials are piezoelectric but not ferroelectric: they belong to non-polar crystal classes and a meta-stable polarization is induced under applied field.

Although each unit cell of ferroelectric materials has a spontaneous polarization, these polarizations are randomly orientated. Therefore unpoled ferroelectric materials have no net remnant polarization, they must be polarized to exhibit a bulk piezoelectric

effect. In addition, when heated above their Curie temperature (T_c), they lose polarization due to a phase change to a non-ferroelectric (paraelectric) phase. Application of stress can also change their poling state. Therefore it is important to control the external field and temperature of ferroelectric devices within appropriate ranges.

Polarization reversal (switching) is a characteristic of ferroelectricity. It is a thermodynamic process of nucleation, growth, and coalescence of domains. It can be observed by measuring the polarization versus electric field curve (D-E hysteresis loop). A typical D-E hysteresis loop of ferroelectrics is shown in Figure 1-4 [6].

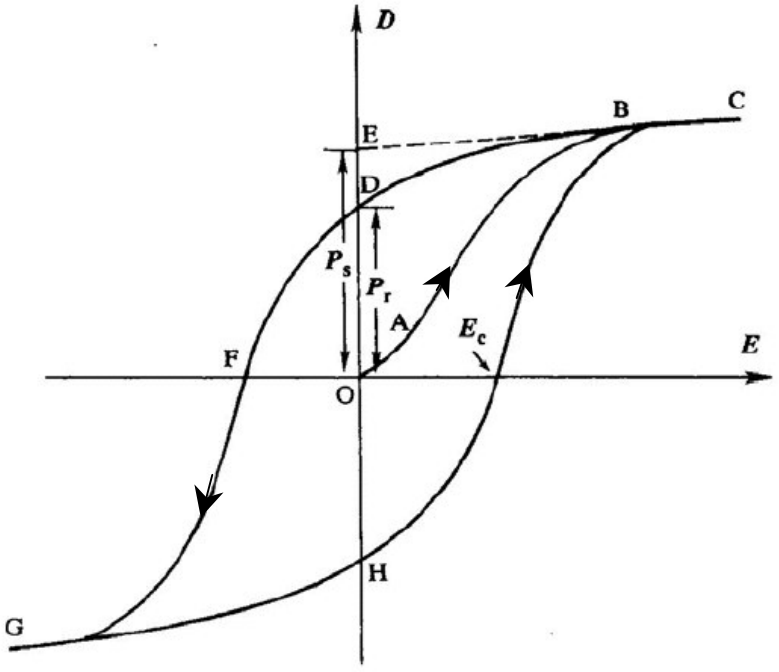

Figure 1-4. A typical *D*-*E* hysteresis loop of ferroelectric materials [6].

As shown in Figure 1-4, initially the unpoled ferroelectric materials have zero polarization (origin point O). As the electric field increases, the spontaneous polarization directions of domains will be forced to switch towards the field direction, resulting in a rapid increase in polarization (segment OAB). A saturation state is reached (BC) when all the domains are aligned as close as possible to the field direction. The linear extrapolation of the segment BC back to the polarization axis (CBE) represents a linear dielectric and piezoelectric response. Appropriately oriented single crystals may provide such a stable polarization state. The polarization value at point E (P_s) is the saturated polarization. Note this is the volume averaging of the spontaneous polarization of all domains. As the field strength decreases, the polarization will actually decrease to point D (BD). This value is called the remanent polarization (P_r). This value is smaller than P_s but nonzero because for piezoceramics some of the domains will remain aligned and some will be reoriented due to grain and domain interaction. The remanent polarization (poling state) holds until the applied field in the opposite direction reaches a certain value (at the point F in the figure). The strength of the field required to reduce the polarization back to zero is called the coercive field (E_c). Further increase of the field will cause an alignment of the dipoles in this direction. Reversing the field direction once again lead to a cycle, and the relation of D and E is represented by a hysteresis loop (CDFGHC) as shown in the figure.

1.2 Relaxor Ferroelectrics

Piezoelectric materials have numerous applications including signal filters, capacitors, sensors, actuators and transducers. Recent developments include medical

ultrasonic imaging, underwater communication, high-displacement piezoelectric actuators, microelectronics and MEMS applications. The development of high performance piezoelectric materials is also in progress.

Lead magnesium niobate [$Pb(Mg_{1/3}Nb_{2/3})O_3$, PMN] was discovered shortly after the discovery of PZT. It is called a "relaxor" ferroelectric material because of its dispersive (frequency dependent) dielectric response and diffuse phase transition (over a wide range of temperature) around the Curie point T_{max} (temperature of the maximum dielectric permittivity) [7]. PMN exhibits extraordinary electromechanical properties and small hysteresis. Another important relaxor is [$Pb(Zn_{1/3}Nb_{2/3})O_3$, PZN]. PMN and PZN single crystals provides very large piezoelectric, dielectric and electromechanical coupling coefficients [8]. For actuators, the squares of electromechanical coupling coefficients give the ratios of output (mechanical) energy to input (electrical) energy. High electromechanical couplings imply low energy loss and low heat generation, which are essential for piezoelectric transducers and actuators.

A solid solution of PMN (or PZN) and $PbTiO_3$ (PT) forms complex perovskite type relaxor ferroelectric PMN-xPT (or PZN-xPT). They combine the properties of both relaxors PZN/PMN and ferroelectric PT, exhibiting extraordinary electromechanical properties. They emerged in the 1990s as a promising group, showing dramatically higher piezoelectric strain than PZT [8,9]. Their single crystal forms were fabricated, which exhibit unusually high piezoelectric effects compared to their ceramic forms (Figure 1-5). Relaxor based ferroelectric single crystals are being considered as the next generation transducer materials. They are attractive in applications such as medical imaging, telecommunication and ultrasonic devices [8,10].

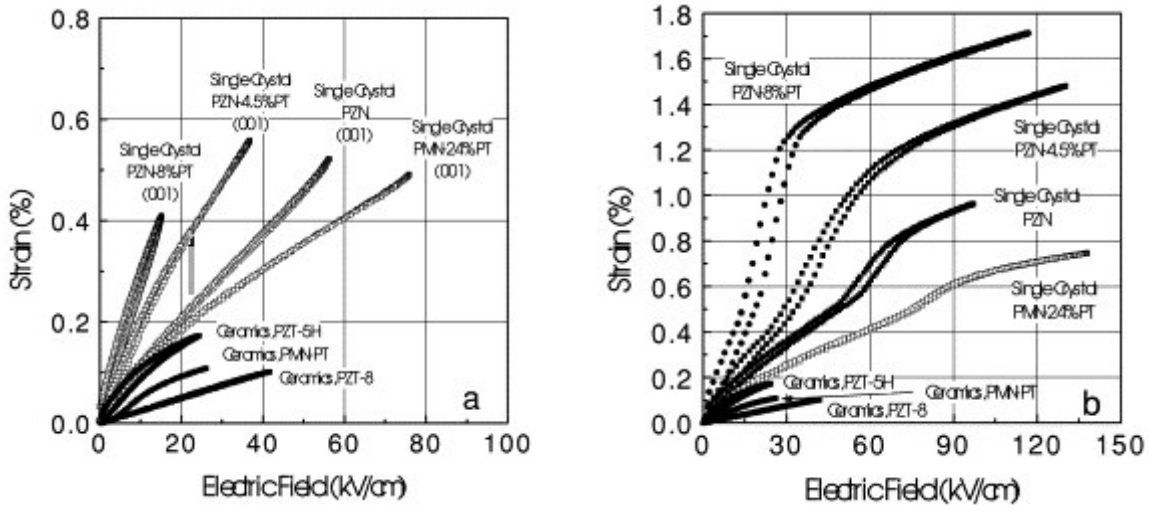

Figure 1-5. Comparison of E-field induced strains for relaxor single crystals versus electroactive ceramics. (a) Non-hysteretic strain behavior at relatively low E-fields; (b) Strain behaviors associated with E-field induced phase transitions [17].

Relaxor ferroelectric single crystals can be grown by the flux method, the top seeded solution growth or the modified Bridgman method [11-13]. Currently it is still difficult and expensive to grow large-size PMN-xPT and PZN-xPT single crystals. A relatively large single crystal PMN-24%PT with the size of φ40 mm × 80 mm was recently grown by a modified Bridgman method [14]. To overcome the difficulty of growing large single crystals, textured relaxor ferroelectric ceramics, with single crystal pieces embedded in a certain direction as growing seeds, have also been proposed and fabricated in recent years. They show enhanced piezoelectric coefficients relative to normal ceramics and approach the single crystal properties with increasing texture [15,16].

Much of the published literature has focused on the properties of <001> oriented and poled PZN-xPT and PMN-xPT crystals due to their high electromechanical coupling

coefficient (k_{33} > 90%), high piezoelectric constant (d_{33} > 2500 pC/N) and extremely large piezoelectric strains (ε_{33} ~ 1.7%) [8,18,19]. Such excellent performance is leading to a revolution in electromechanical applications. These crystals have been used for electromechanical transducers and actuators in a broad range of advanced applications such as medical ultrasonic imaging and high-performance underwater communication [10,20,21].

The outstanding properties of the relaxor-based ferroelectric crystals are closely related to their domain and phase states. These domain structures and phase states, at the same time, make their electromechanical behavior very complicated [22]. Furthermore, hysteresis, fracture and fatigue become the main reliability issues deteriorating their performance. Their poling behavior is rate dependent and sensitive to mechanical loads. The low elastic stiffness, low coercive field and low Curie temperature place limits on the stress, electric field and temperature range of operation and device fabrication processing. Research on the domain and phase structures, electromechanical response, field induced polarization switching and phase transitions, hysteresis, fracture, fatigue, and rate effects etc, therefore, is demanded along with the development of these materials and their applications.

1.3 **Contents of Dissertation**

There are physics interests as well as application needs to understand the mechanism of complex polarization switching and phase change behavior of relaxor ferroelectric single crystals under applied temperature and external field. Due to their

simple microstructure and uniform crystal orientation relative to ceramics, relaxor ferroelectric single crystals are the ideal candidates for the study of ferroelectricity and the mechanism of electromechanical behavior.

This research investigated the nonlinear polarization and phase transition behavior of relaxor ferroelectric PZN-xPT and PMN-xPT single crystals. Complex polarization switching and phase change behavior of PZN-4.5%PT and PMN-32%PT crystals at different orientation cuts under different temperature, stress and electric field loading were observed. The electromechanical properties of engineered domain single crystals were studied by multi-variant modeling. Work-energy analysis and generalized energy based phase change criteria were investigated.

In Chapter 2 the related background and previous research on relaxor ferroelectric crystals, including piezoelectric constitutive relation, domain structures and phase states of the materials, field induced polarization and phase transition, are reviewed.

In Chapter 3, a combination of modeling and experimental work has led to the identification of a <110> orientation of PZN-4.5%PT single crystals with enhanced piezoelectric coefficients and direct evidence of a rhombohedral-orthorhombic phase transformation under <110> electric field loading. A crystal variant model enables computation of the physical properties of engineered multi-domain single crystals from the properties of the single domain <111> poled rhombohedral phase. Implemented with criteria for variant and phase evolutions, the model reproduces the observed hysteresis loops, remanent strain and remanent polarization.

Chapter 4 reports the experimental investigation of the field induced phase transition behavior of <110> oriented relaxor PMN-32%PT single crystals. The single

crystals were subjected to combined stress, electric field and thermal loading. The electric field induced polarization and strain for a series of bias stresses and the stress induced polarization and strain for a series of bias electric fields were measured. The results demonstrate that combinations of stress and electric field drive a phase transformation and that the driving force for this transformation decreases with increasing temperature. The threshold for the phase transformation at each temperature is used to generate a stability map for the material.

In Chapter 5, a thermodynamics based analysis of the measured material behavior in <110> orientated PZN-4.5%PT (Chapter 3) and PMN-32%PT (Chapter 4) crystals under combined stress, electric field and temperature loading conditions leads to a direct measurement of the relative phase energy levels. The approach demonstrates how different fields contribute to the phase transition, and that a small number of experiments are sufficient to characterize the multi-field driven phase transformations.

In Chapter 6, phase transformations of an <001> oriented PMN-32%PT single crystal induced by combinations of stress, electric field, and temperature loading are mapped experimentally. Stress, strain, electric displacement, electric field and temperature are varied and measured. The results indicate that combinations of stress and electric field drive several phase transformations, and the driving force for the transformations decreases with increasing temperature.

In Chapter 7, compressive stress and electric field were applied to relaxor single crystal PZN-4.5%PT in a series of crystal orientations between <001> and <111>, and the corresponding strain and electric displacement were measured. The remnant strain, remnant electric displacement, and piezoelectric coefficients are discussed in terms of

volume averages of crystal variant volume fractions. The bipolar electro-mechanical response of the crystals, including hysteresis and nonlinear phenomena, rate effect related to polarization reorientation and phase transition, are discussed.

In Chapter 8, partial electrodes and specimen geometry were studied in single crystal PZN-4.5%PT to characterize the fracture behavior near an electrode edge. Crack growth was characterized by varying the specimen thickness (t = 0.7 mm and 2 mm) and electrode coverage (50~95%). Linear elastic finite element modeling was used to determine the field singularity near the electrode edge and evaluate the internal energy density.

Conclusions are made in the last chapter of the dissertation. This research provides direct experimental data as well as analytical and numerical results for field induced polarization switching and phase change behavior of relaxor ferroelectric single crystals. These results are essential for understanding and manipulating the nonlinear electromechanical behavior of these crystals.

CHAPTER 2

BACKGROUND AND LITERATURE REVIEW

In recent years development of crystal growth techniques have provided larger and lower cost relaxor ferroelectric single crystals for characterization and applications. There has been a deeper understanding of the domain and phase structures of the rhombohedral, tetragonal, orthorhombic and monoclinic phases, their polarization switching and the phase change mechanism of relaxor single crystals [23]. In this chapter the macroscopic piezoelectric constitutive relation and microscopic crystal phases and domain structures are introduced; experimental characterization of the polarization switching and phase transition behavior of relaxor ferroelectrics under external field, theory modeling and simulation of these materials are reviewed.

2.1 Piezoelectric Constitutive Relation

By choosing stress and electric field, which are usually the controlled variables in experiments, as the independent variables, a formulation based on enthalpy leads to the following linear piezoelectric constitutive equations:

$$\varepsilon_{ij} = s_{ijkl}^{E}\sigma_{kl} + d_{nij}E_n \tag{2-1a}$$

$$D_m = d_{mkl}\sigma_{kl} + K_{mn}^{\sigma}E_n \tag{2-1b}$$

where σ_{kl} and E_n are applied stress and electric field, ε_{ij} and D_m are the strain and the electric (charge-density) displacement, and s^E_{ijkl}, d_{mkl} and K^σ_{mn} are the elastic (at constant electric field), piezoelectric, and dielectric (at constant stress) coefficients, respectively.

Polarization (P_i) is the electric dipole moment per unit volume, it is related to electric displacement (D_i) though a linear expression:

$$D_i = P_i + \varepsilon_0 E_i \tag{2-2}$$

where ε_0 is the permittivity of free space. When the term $\varepsilon_0 E_i$ in the above expression is negligible compared to P_i (as is the case for most ferroelectric materials), D_i is nearly equal to P_i, the electric displacement and polarization are therefore often referenced without distinction.

As reflected in Equation 2-1, the piezoelectric coefficients relating an electric field and the induced strain are termed the strain constants (**d** coefficients, a third-order tensor). There are also the piezoelectric coefficients relating a stress and the induced electric displacement. It is defined as the ratio of the electric charge generated per unit area to an applied stress, and its units are Coulombs per Newton (C/N). Higher piezoelectric **d** coefficients indicate that larger amount of strain can be induced from the same electric field. It is these coefficients that describe the electromechanical coupling.

Due to the electromechanical coupling effect, the elastic coefficients are dependent on the electric boundary conditions; therefore their values are given along with the specific electric condition, i.e. constant electric field (such as short circuit) or constant

electric displacement (open circuit). Accordingly the dielectric coefficients are dependent of the mechanical boundary conditions, i.e. constant stress (free of mechanical clamping) or constant strain (clamped) condition.

The four state variables (σ, ε, **D**, and **E**) can be rearranged to give three other forms of piezoelectric constitutive equations [24]. Accordingly instead of **d** coefficients, there are **e**, **g**, or **q** coefficients. The coefficients in the constitutive relation can be transformed from one form to another.

2.2 Microstructure, Phases and Domains

Most synthetic piezoelectric materials are in ceramic (poly-crystal) form with mesoscopic grain structures [25]. Each grain is a tiny single crystal, in which there is uniform arrangement of atoms. Such an arrangement can be represented by a representative volume element (RVE), with the behavior dictated by that of a unit cell of atoms. Inside a grain of the ferroelectric materials there are domain structures. A domain is a region with a uniform polarization, surrounded by regions with other polarization directions. Domain structures in a ferroelectric single crystal are correlated to its electromechanical properties. Between domains are the interfaces called domain walls. Such a poly-domain system results from free energy minimization during the thermodynamic process.

2.2.1 Perovskite Structure

Perovskite is the mineral name of calcium titanate ($CaTiO_3$). It has a cubic high temperature phase (space symmetry P*m3m*). Many mixed oxides of the ABO_3 type (or $AB^{I}B^{II}O_3$) share such perovskite structure. In fact most of the common ferroelectrics, including barium titanate ($BaTiO_3$), lead titanate ($PbTiO_3$), lead zirconate titanate (PZT) and lead lanthanum zirconate titanate (PLZT), have the perovskite structure. Shown in Figure 2-1a, the perovskite structure (unit cell) of lead titanate ($PbTiO_3$) can be viewed as a cubic arrangement of Pb ions with O ions at the face centers and smaller Ti ions filling the cubic centers.

Due to a centrosymmetric structure, the high temperature cubic phase is paraelectric. It may become ferroelectric when undergoing a structural phase transition upon cooling. Figure 2-1 compares the unit cells of the paraelectric cubic phase and the ferroelectric tetragonal phase. Ferroelectricity is observed in certain temperature regions below Curie points (T_C), in which the materials exhibit one or more polar phases associated with specific lattice parameters and polarizations.

The tetragonal phase may undergo 90° or 180° polarization switching among the six equivalent polarization directions (Figure 2-2). The polarization switching induced by an electric field is called ferroelectric switching (90° or 180°), and that induced by a stress is called ferroelastic switching (90°) [26]. A stress does not induce 180° switching because 180° switching doesn't accompany a change of spontaneous strain.

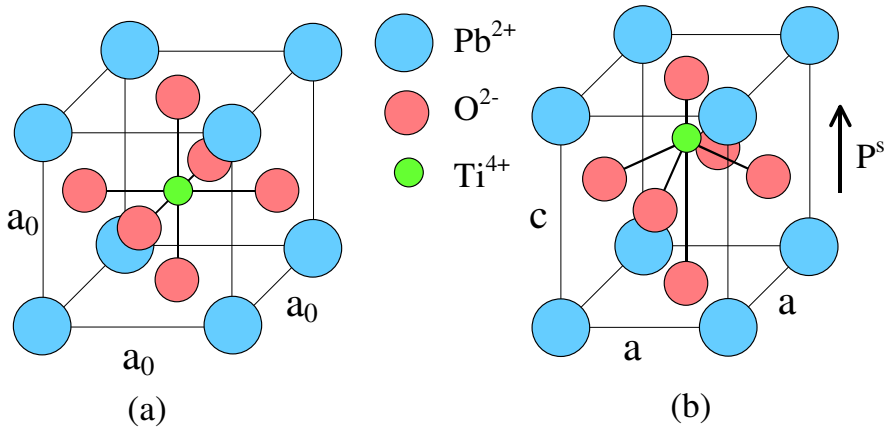

Figure 2-1. Perovskite structure of $PbTiO_3$ (ABO_3 type) mixed oxides. (a) Paraelectric cubic phase above Curie temperature; (b) ferroelectric tetragonal phase below Curie temperature.

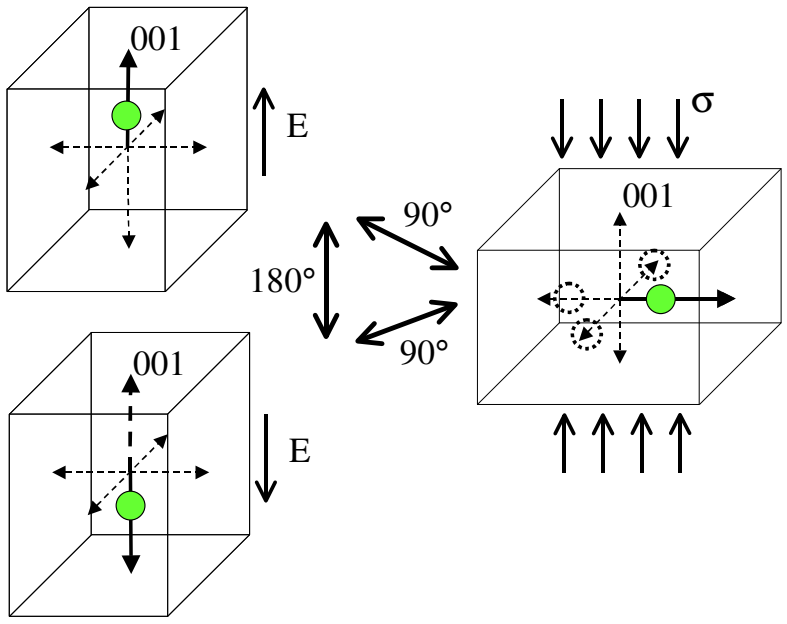

Figure 2-2. Polarization switching of the tetragonal phase. A stress induces 90° ferroelastic switching; an electric field induces 90° or 180° ferroelectric switching.

2.2.2 Structural Phases

Relaxor PZN-xPT and PMN-xPT crystals share the same perovskite structure. A transformation from the high temperature cubic phase to the tetragonal, rhombohedral or orthorhombic phase results in a spontaneous polarization in <001>, <111> or <110> direction as well as a small shape and volume change (spontaneous strain) of the cubic structure. Figure 2-3 shows the structure symmetry and spontaneous polarization directions of the cubic, tetragonal, rhombohedral and orthorhombic phases. The tetragonal phase has 6 equivalent spontaneous polarization directions corresponding to 6 kinds of domains (or 6 crystal variants). Accordingly the rhombohedral phase has 8 variants, and the orthorhombic phase has 12 variants. For the three kinds of monoclinic phases, the domain configuration becomes even more complicated with 24 domain states for each kind [27]. Increasing crystal variants means increasing complexity of polarization switching and domain patterns under different external fields.

In mesoscopic models, it may be assumed that each crystal variant of a given phase follows the same ferroelectric constitutive law described in its own (local) coordinates:

$$\varepsilon_{ij} - \varepsilon_{ij}^{s} = s_{ijkl}^{E}\sigma_{kl} + d_{nij}E_{n} \tag{2-3a}$$

$$D_{m} - D_{m}^{s} = d_{mkl}\sigma_{kl} + K_{mn}^{\sigma}E_{n} \tag{2-3b}$$

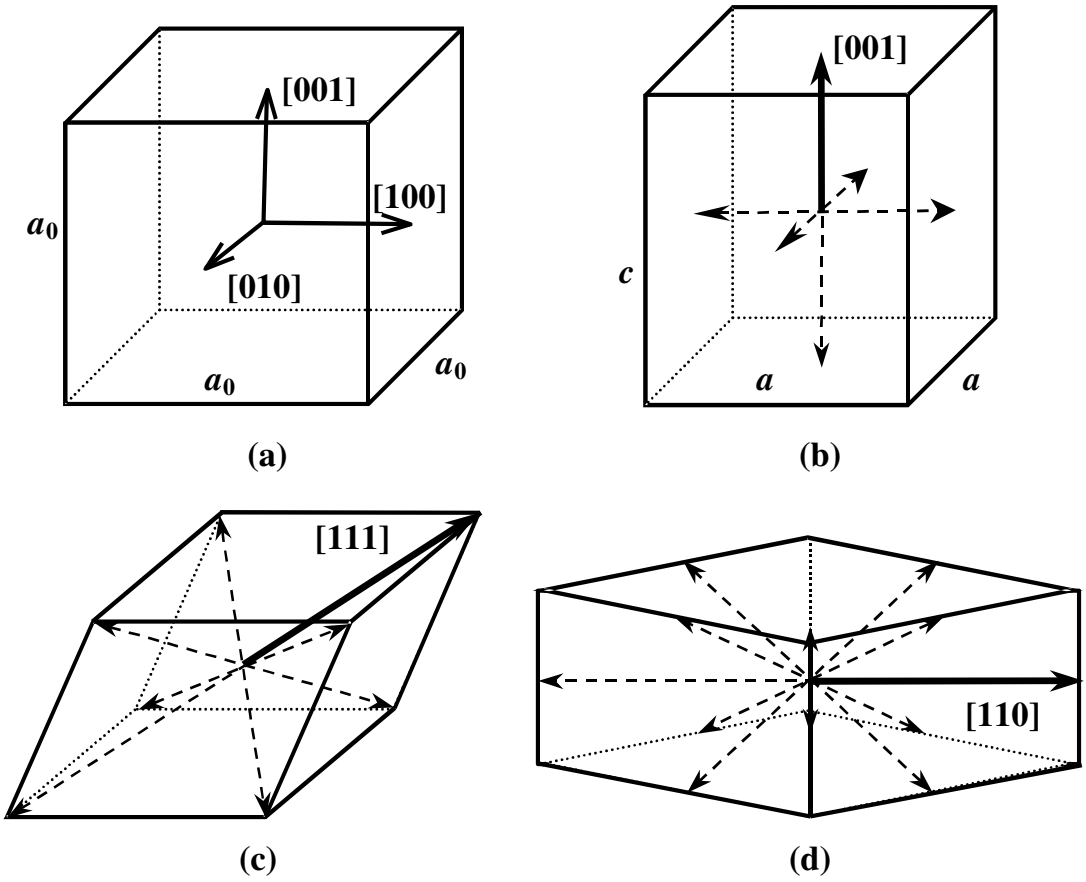

Figure 2-3. Phases and crystal variants. (a) Cubic phase, (b) Tetragonal phase with 6 variants, (c) Rhombohedral phase with 8 variants, (d) Orthorhombic phase with 12 variants.

Equations 2-3 differ from the linear piezoelectric equations 2-1 by additional terms ε_{ij}^{s} and D_{m}^{s} representing respectively the spontaneous strain and the spontaneous electric displacement. Furthermore, coefficients s_{ijkl}^{E} , d_{mkl} and K_{mn}^{σ} are functions of loads, polarization and phase state.

The symmetries of the elastic, dielectric and piezoelectric tensors for each phase are associated with the crystal symmetry of that phase [28]. For example, the tetragonal phase has *4mm* symmetry and the nonzero piezoelectric components are $d_{31} = d_{32}$, d_{33} and

$d_{15} = d_{24}$; the rhombohedral phase has trigonal class *3m* symmetry with associated nonzero $d_{31} = d_{32}$, d_{33}, $d_{15} = d_{24}$ and $d_{16} = 2d_{21} = -2d_{22}$; the orthorhombic phase has *mm2* symmetry with five nonzero components: d_{31}, d_{32}, d_{33}, d_{15}, d_{24}.

2.2.3 Phase Transitions

High-resolution diffraction studies revealed the intricate nature of the morphotropic phase boundary (MPB), which involves the rhombohedral, tetragonal, orthorhombic and monoclinic phases [29,30]. As shown in Figure 2-4, the coexistence of both rhombohedral and tetragonal domains in PZN-9%PT crystals at room temperature has been observed [31,32]. The growth of the tetragonal domains upon heating reflects the R-T morphotrophic phase transition. Noheda *et al.* [33] demonstrated the presence of multiple phases using synchrotron radiation and discussed the contributions of a monoclinic phase to the <001> piezoelectric response. Recently both the orthorhombic phase and monoclinic phase have been observed for PZN-xPT and PMN-xPT single crystals [33-37].

Figure 2-5 shows the phase diagrams of PZT, PZN-xPT and PMN-xPT around the MPB [38]. Three kinds of monoclinic phases in PMN-xPT have been experimentally confirmed [39-41].

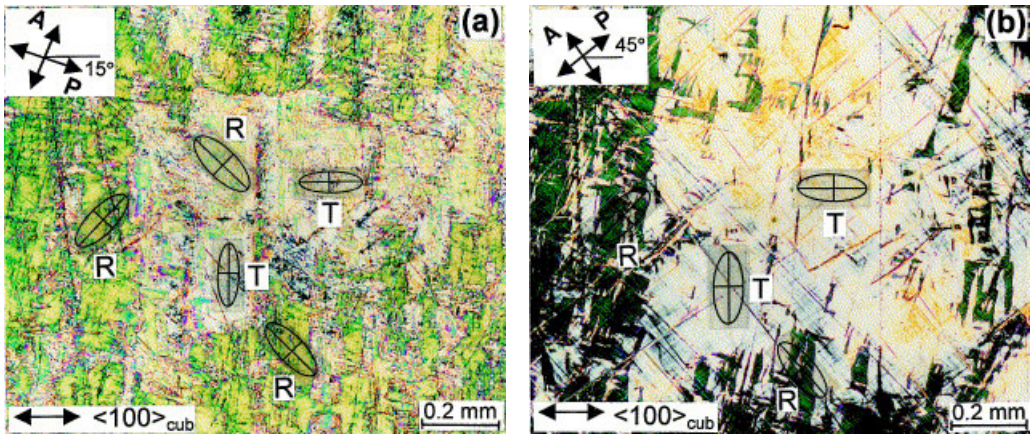

Figure 2-4. Morphotropic domain structures and phase transition. (a) Coexistence of the rhombohedral domains (R, with extinction ∥ <110>$_{cub}$) and the tetragonal domains (T, with extinction ∥ <100>$_{cub}$) at 25 °C in a <001> PZN-9%PT crystal platelet; (b) Domain structure at 70 °C. [31,32].

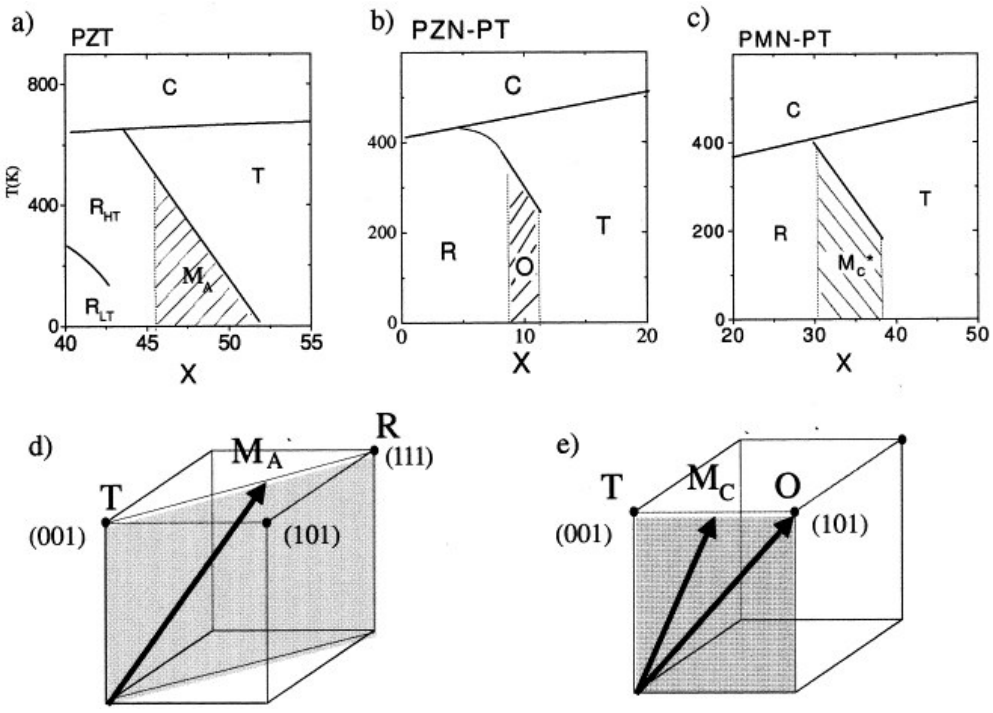

Figure 2-5. Phase diagrams of PZT, PZN-PT and PMN-PT [38]. (a) PZT [36]; (b) PZN-xPT [42]; (c) PMN-xPT [43]; (d) The monoclinic M_A phase rotating between the rhombohedral (R) and tetragonal (T) phases; (e) The monoclinic M_C and orthorhombic (O) phases rotating in the (010) plane (shaded).

2.2.4 Domain Structures

One characteristic feature of the relaxor-based ferroelectric crystals is their complex domain structure. Multi-domain structure as well as multi-phase coexistence around the morphotropic phase boundary (MPB) make major contributions to the enhanced electromechanical properties of relaxor single crystals [44,45].

New domains are formed through nucleation and growth. Direct microscopic domain observation techniques combined with macroscopic property measurements (such as switching current data, dielectric coefficients) are employed to understand the process of polarization switching and phase transitions. Various methods including polarized light microscopy (Figure 2-4, 2-6), scanning electron microscopy (SEM), transmission electron microscopy (TEM), atomic force microscope (AFM), scanning force microscopy (SFM) and piezoelectric force microscopy (PFM) have been used for imaging ferroelectric domain structures [46-48]. By applying pulsed electric fields, Yu *et al.* [49,50] observed dendritic domain structures (Figure 2-7) in PZN-8%PT single crystals by AFM on etched surfaces. These observations are very helpful in understanding domain nucleation and growth.

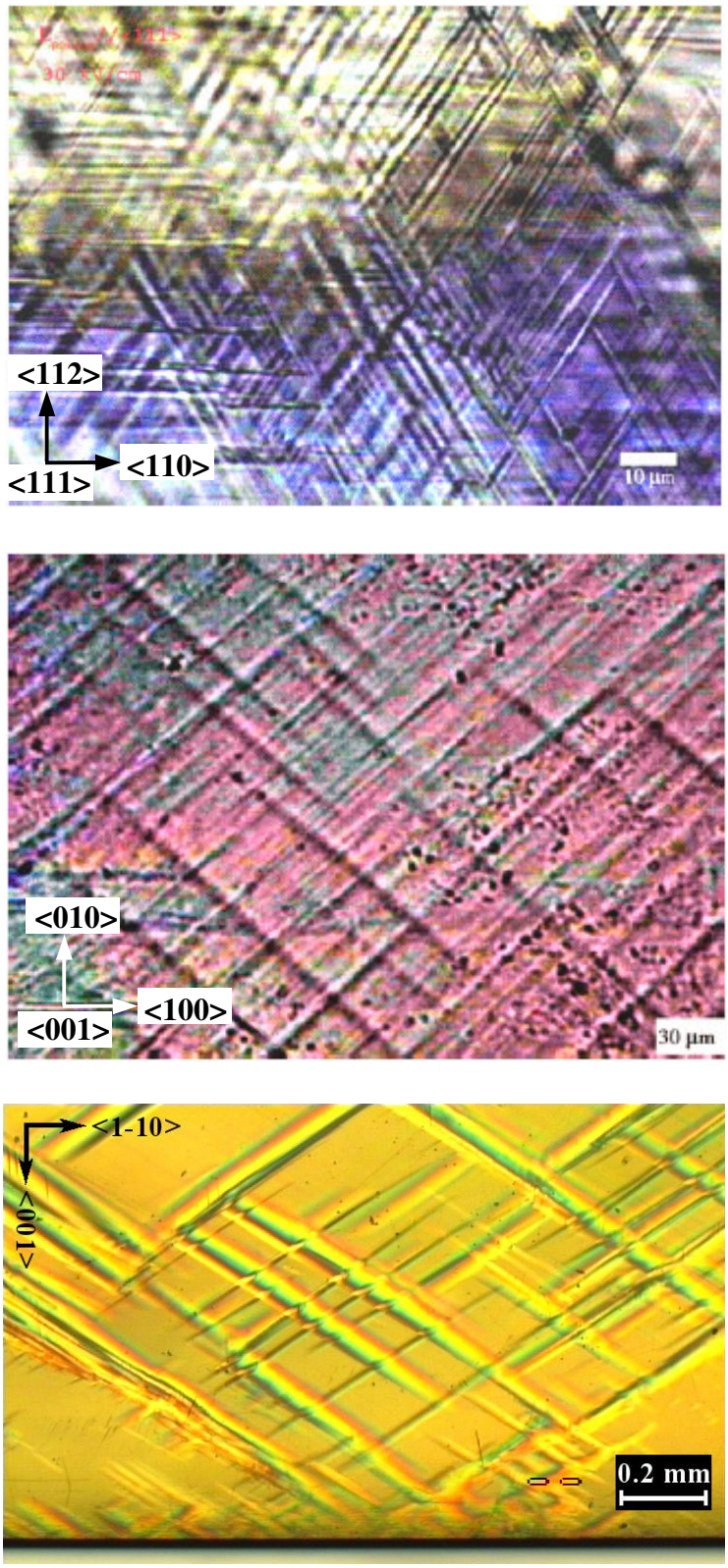

Figure 2-6. Domain patterns observed in PZN-4.5%PT single crystals under polarizing microscope. (a) <111> poled [51], (b) <001> poled [51], (c) <110> poled [52].

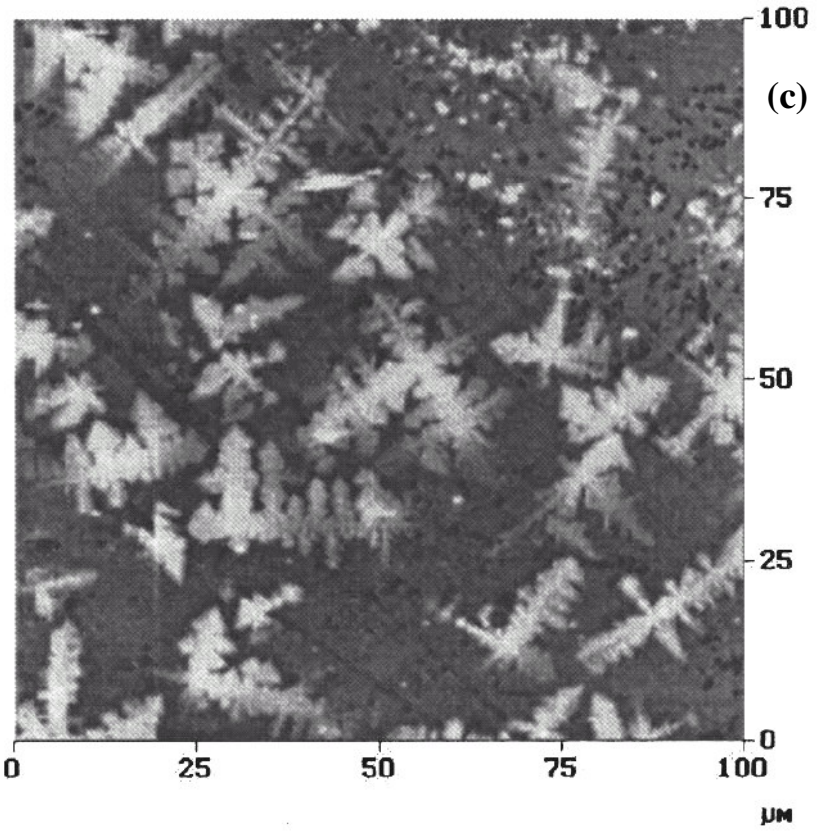

Figure 2-7. Dendritic domain structure in PZN-8%PT single crystals under <001> pulsed electric fields [49,50].

2.3 Polarization Switching and Phase Transitions under External Field

Application of temperature, stress and electric field to ferroelectric materials changes the energy of the materials and leads to polarization switching and phase transitions. Each material has a particular operating limit for temperature, voltage, and stress in order to prevent unwanted polarization switching or phase transitions. The chemical composition of a material determines the limits. Operating a material outside of these limitations may cause partial or total depolarization of the material, and a diminishing or loss of piezoelectric properties.

2.3.1 Temperature and Rate Effects

As reviewed by Jaffe *et al.* [25] and Lines & Glass [53], temperature and rate dependence are two significant features of ferroelectric material behavior. Dielectric coefficients of relaxor ferroelectrics vary over a large temperature range, in which a diffuse phase transition occurs. Their dielectric coefficients also show strong dependence of field frequency. Furthermore, the coercive field, strain and electric displacement response to stress and electric field are also dependent of loading rate [54], and the rate effect itself is affected by crystal orientations and some other conditions. Increasing temperature introduces significant effects including decrease of the strain and electric displacement response, reduction of switching energy (or coercive field), and change of the compliance, piezoelectric and the dielectric coefficients [55]. Mukherjee *et al.* [56] made extensive measurements of these coefficients as functions of temperature, frequency, applied electric field and stress.

2.3.2 Electric Field Effect

There have been many research efforts directed at understanding polarization switching and phase transitions under applied electric field in relaxor single crystals. A single-domain state of ferroelectric crystals may be obtained through the polarization process by application of an electric field in an appropriate direction. Rhombohedral PZN-xPT and PMN-xPT crystals can be polarized into a single domain state with an electric field in <111> direction. Ujiie and Uchino [57] observed domain reversal in relaxor ferroelectrics PZN-xPT under <111> electric field using a CCD microscope system. Depolarization and subsequent domain reorientation occur under <111> electric

field. The electromechanical coupling properties of <111>-cut PZN-xPT crystals are relatively low.

Electric field cycling produces butterfly shaped strain-electric field (ε-E) curve (butterfly hysteresis loops) associated with the polarization-electric field (D-E) hysteresis loop. The process is described in Figure 2-8 [58]. Properties of these crystals along different orientations are greatly different. Figure 2-9 shows the difference of the polarization and strain versus E-field (bipolar) curves for PZN crystals oriented along <111> and <001> [8]. Shown in the figure, the remnant polarization of the <111> cut is much higher than that of the <001> cut, and the two "butterflies" are clearly of two different "styles". When the crystals are poled along the non-polar direction <001>, an engineered domain state forms [8,59], providing superior electromechanical properties. In addition, with such an engineered domain state, fatigue properties were greatly improved in PZN-xPT single crystals [60-62].

In addition to the high performance <001> orientation cuts, <110>-oriented rhombohedral crystals were later found to also show enhanced electromechanical performance. Viehland *et al.*'s [63] investigations of <110>-oriented PZN-xPT and PMN-xPT crystals showed very high piezoelectric constants and electromechanical coupling coefficients. For tetragonal PMN-38%PT crystals, Cao *et al.* [64] reported the enhancement of piezoelectric and dielectric properties of engineered-domain <110> and <111> orientation cuts. In addition, they observed a possible tetragonal to orthorhombic phase transition in both <110> and <111> poled crystals.

Relaxor PZN-xPT and PMN-xPT single crystals display both temperature and field dependent phase transformations. An electric field induced phase change between the

rhombohedral phase and tetragonal phase has been reported [59,65]. Fu and Cohen [66] discussed polarization rotation paths based on first principle calculations. Noheda *et al.*'s [36] experimental results make clear that once the crystal has been driven through the rhombohedral to tetragonal phase transition by application of a large electric field in the <001> direction, there is a permanent phase change in the crystal. This was also suggested by Viehland's [67] experimental results which indicate a change of coercive field for 180° switching after the material has been driven through the phase change and back. He believed that there was an intermediate orthorhombic phase in the <001> oriented crystal. Phase instability was observed for <110> oriented crystals at a critical transformation temperature and/or electric field [63]. Phase changes during reorientation switching induce additional heterogeneity in the crystals.

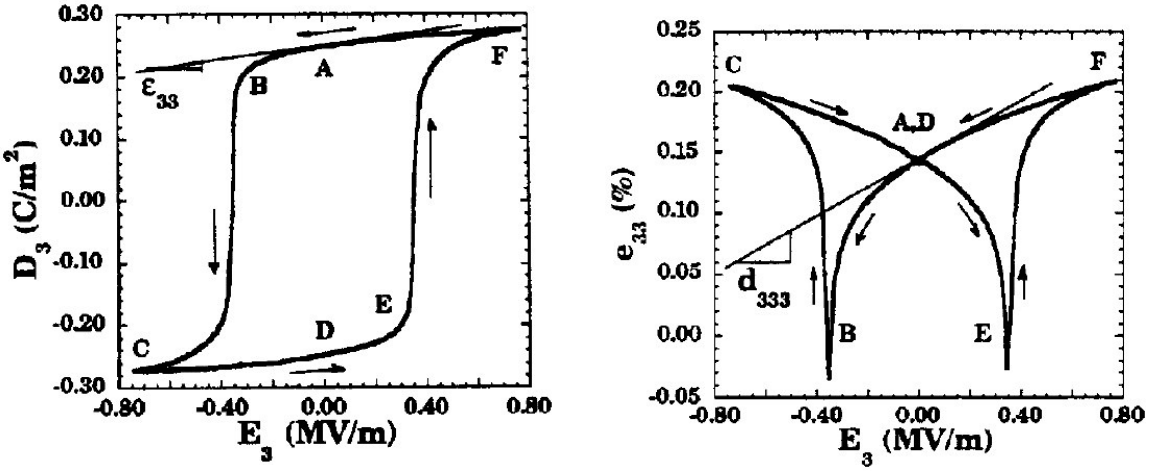

(a) **(b)**

Figure 2-8. Electric field induced polarization switching in 8/65/35 PLZT [58]. (a) Electric displacement hysteresis loop; (b) Strain hysteresis loop.

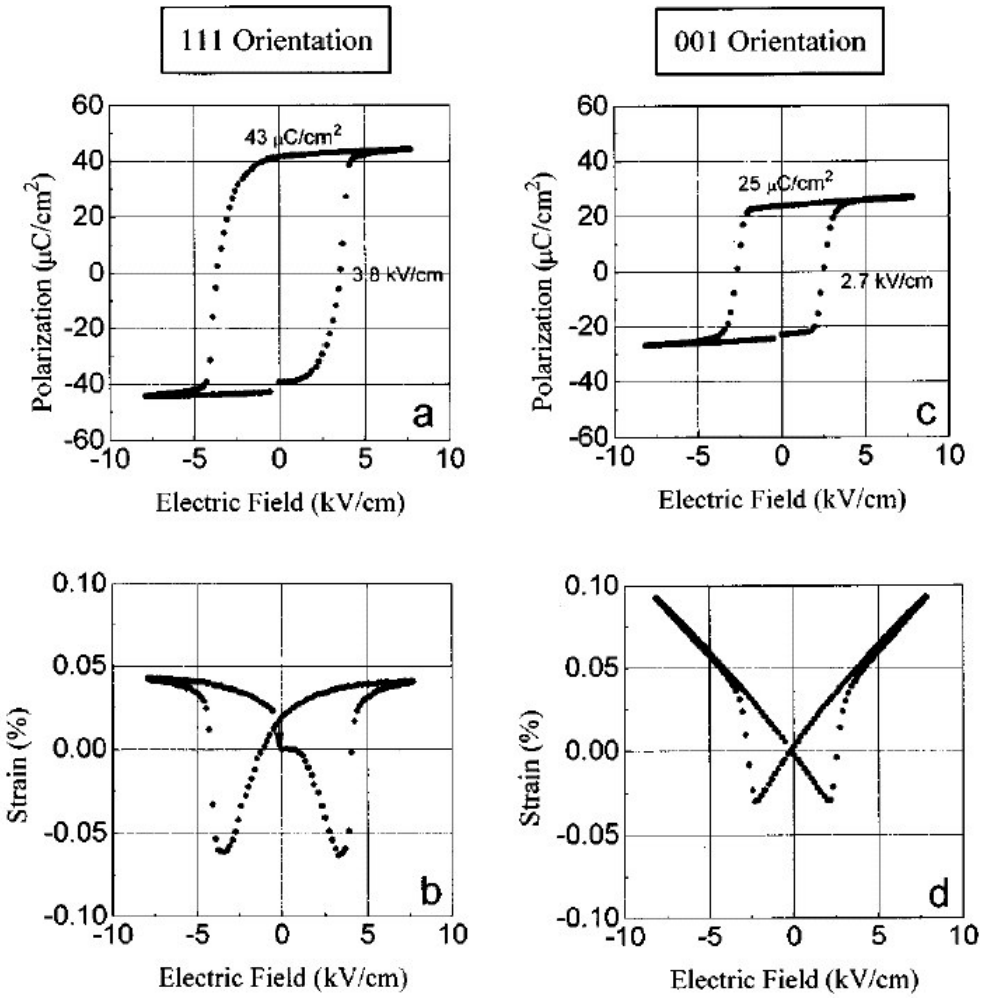

Figure 2-9. Polarization and strain response of PZN single crystals under electric field [8]. (a)(b) <111> oriented; (c)(d) <001> oriented.

2.3.3 Stress Effect

In operation of actuators and transducers, the piezoelectric elements are subject to both electric field and stress. Application of stress also leads to polarization switching and phase transitions. In the 1960s Krueger and Berlincourt [68-70] began to study the nonlinear behavior of ferroelectric materials due to high value pre-stress. Meeks and

Timme [71] had a comparative study of the effects of high stress on PZT ceramics. In their study they observed a tetragonal to rhombohedral phase transition. Cao and Evans [72] measured the stress-strain curves of PZT with the compressive stress along the polar axis. They found that the non-linearity and hysteresis vary with the material compositions. Lynch [58] recorded the stress-strain curves (Figure 2-10) as well as electric field cycling data with pre-stress (Figure 2-11). The non-linearity in Figure 2-10 is associated with the ferroelastic polarization switching (depolarization). In Figure 2-11 it is shown that both the remnant polarization and remnant strain (in the loading direction) decrease with increasing compressive stress, and the critical stress for domain switching of 8/65/35 PLZT was 20~30 MPa. Schaufele and Hardtl [73] in their study of PZT ceramics showed that the coercive stress of ferroelectrics is linearly dependent on the electric field when both stress and electric field are parallel to the polarization direction. Stoll and Lynch [74] characterized four different PZT compositions under uniaxial stress and electric loading, in which similar results were obtained. Generally, similar to the effect of increasing temperature, increase of the compressive mechanical load during electric field cycling tends to reduce the hysteresis of the switching process. Chaplya and Carman [75] also studied the effect of bias electric field on the nonlinear stress-strain response of ferroelectric ceramics. They explained the observed phenomena based on non-180° domain-wall motion and balance of mechanical and electrical energies.

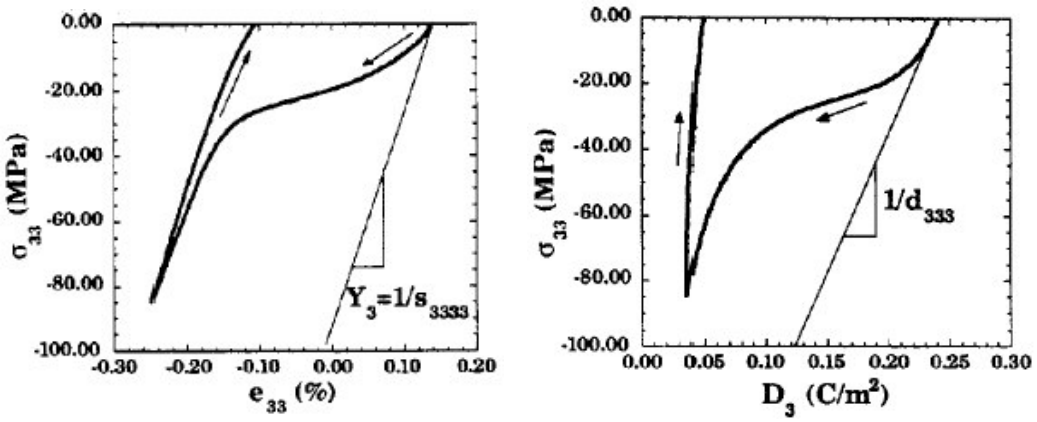

(a) (b)

Figure 2-10. Stress induced polarization switching in 8/65/35 PLZT [58]. (a) Stress vs. strain; (b) Stress vs. polarization.

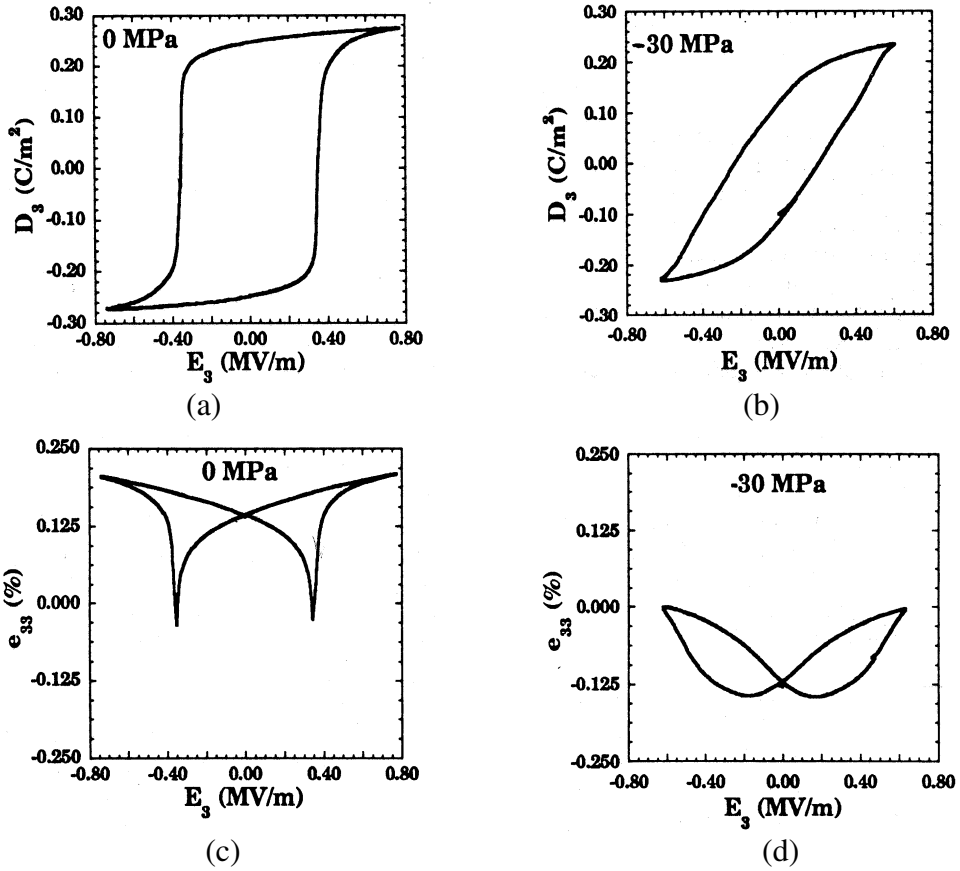

(a) (b)

(c) (d)

Figure 2-11. Responses of 8/65/35 PLZT under electric field cycle at different prestresses [58]. (a)(b) Electric displacement vs. electric field; (c)(d) Strain vs. electric field.

There are still very limited investigations on the effects of stress to the polarization switching and phase transformations of PZN-xPT and PMN-xPT single crystals. Samara *et al.* [76] found that application of high pressure greatly shifted the paraelectric-ferroelectric transition temperature of PZN-9.5%PT single crystals and even caused the tetragonal phase to disappear. Viehland and Powers [77] investigated the electromechanical coupling coefficient of PMN-30%PT <001>-oriented crystals under uniaxial stress and temperature. Their results demonstrated that the electromechanical coupling coefficient is insensitive to stress and temperature. On the other hand, Viehland and Powers [78] also showed that uniaxial compressive stresses significantly altered the electromechanical properties of the <001> oriented PMN-30%PT crystals. They observed a partial depolarization when the crystal was compressed along <001>. A dramatic drop of polarization was observed at the same electric field when the crystal was compressed along <001> at 30 MPa. Their results showed that the remanent polarization and remanent strain shift with stress. There is little information in the literature concerning the effects of combined thermal, stress and electric field loading.

Indentation techniques have been applied to study the stress effects on domain switching of ferroelectric single crystals. Shang and Tan [79] observed the stress induced domain switching in a <001> oriented PMN-35%PT crystal by applying a micro-indentation and proposed a critical shear stress criterion for the 90° domain switching. Fang and Yang [80] observed the domain switching patterns and indenting crack orientations in $BaTiO_3$ single crystals.

2.4 Theory, Modeling and Simulation

Along with experimental observation and measurements, theoretical and numerical models are needed to simulate the nonlinear response of ferroelectrics, especially when they are subjected to arbitrary stress and electric field. It is also important to adequately describe the dynamic response of relaxor ferroelectrics over a wide range of frequency and temperature.

Linear piezoelectricity is well understood. It has been implemented in commercial finite element packages including ABAQUS, ANSYS and NASTRAN for structural analysis and simulation. Yet linear piezoelectric relation is valid only for a limited range of loading for most ferroelectric materials. As reviewed above, ferroelectric materials show strong non-linearity and hysteresis (irreversibility) due to complex polarization switching and phase changes [53,58]). Models and numerical methods for complex loading and boundary conditions are currently under development.

Constitutive models can be grouped into phenomenological modeling and micro-mechanics modeling, covering length scales from unit cell level to device level. Phenomenological (macroscopic) models [81-83] try to capture the macroscopic behavior of ferroelectric materials using macroscopic state variables and thermodynamic potential functions. For example, by means of an eighth-order expansion of Devonshire theory, Vanderbilt and Cohen [84] developed a thermodynamic framework to describe three possible monoclinic phases (M_A, M_B, M_C). Micro-mechanics models [85,86], particularly at the mesoscopic level, select a single domain (or a unit cell) as the representative volume element (RVE) and model its response. The macroscopic response is then obtained by volume averaging of numerous unit cells. Micro-mechanics models allow

considerations of the mechanism and contributions of domain wall structures, grain boundaries, interaction of domains and grains [55]. Micro-electromechanical models may be used together with experimental data to fine tune phenomenological models in order to achieve both accuracy of description and speed of computation [87].

A number of theoretical studies on the mechanism of polarization and phase transitions in ferroelectrics have been performed. A constitutive model for $PbTiO_3$ was obtained by constructing an effective Hamiltonian based on ab initio calculations [88]. The Monte Carlo method was used to simulate the dielectric and ferroelectric behaviors of relaxor ferroelectrics based on Ginzburg-Landau theory [89,90]. By considering the contributions to the free energy, numerical simulations of the formation of domain structures can be performed [91-95]. Recently random field theory was used to describe relaxor ferroelectric properties [96]. Along with theoretical modeling, there were many research effects on nonlinear finite element techniques for electrostrictive ceramics and nonlinear ferroelectric materials [97-102].

Criteria for polarization switching and phase transitions are needed in models. Based on experimental measurements (such as coercive field), energy based polarization switching criteria have been used to simulate the behavior of ferroelectric ceramic PZT [85,103-105], electrostrictive PMN-xPT [106] and antiferroelectric PLSnZT [107]. The modeling approach assumes that switching between variants occurs when an applied stress or electric field provides sufficient driving force to overcome an energy barrier (as shown in Figure 2-12). An energy criterion can handle multi-axial problems and unify the work done by both stress and electric field. An energy based criterion may also be used for phase transformations [86].

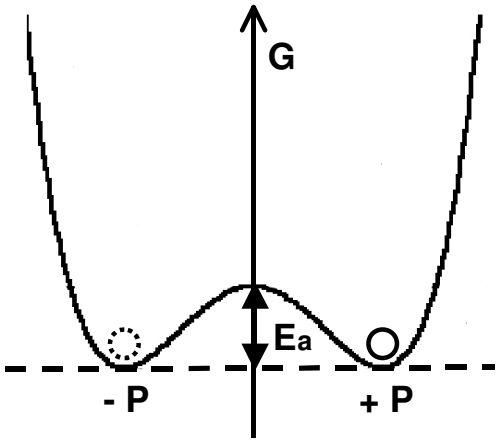

Figure 2-12. Energy wells of a 180° polarization switching.

Complex domain and phase activities in ferroelectric materials lead to nonlinear electromechanical response as well as reliability issues such as hysteresis loss, fracture and fatigue. In addition to change of electromechanical coefficients and modeling complexity, hysteresis during polarization switching and phase transition leads to energy loss, heat generation and other problems. Fracture is a major reliability issue in piezoelectric devices such as multi-layer piezoelectric actuators [108-110]. Another one is fatigue, which is accompanied with decay of the remnant polarization and a collapse of the polarization hysteresis loop. Observed polarization switching and fatigue phenomenon in ferroelectrics suggests complex mechanisms behind fatigue [111].

Research on the electromechanical behavior of relaxor ferroelectric PZN-4.5%PT and PMN-32%PT single crystals under external fields is presented in the following chapters, in which additional reviews of previous research regarding specific topics will be given.

CHAPTER 3

MEASUREMENT AND MODELING OF ENGINEERED DOMAIN RELAXOR SINGLE CRYSTALS

A combination of modeling and experimental work has led to the identification of a <110> crystal orientation cut of PZN-4.5%PT with enhanced piezoelectric coefficients (d_{31} = 690 pC/N, d_{32} = -1670 pC/N, which are excellent for bending mode applications) and direct evidence of a rhombohedral-orthorhombic phase transformation under <110> electric field loading. A crystal variant model enables the calculation of the piezoelectric coefficients of the engineered multi-domain single crystals from the properties of the single domain <111> poled rhombohedral phase. As not all of the <111> piezoelectric coefficients have been directly measured, the modeling approach is used to compute the missing coefficients, d_{15} and d_{16} of the <111> poled crystal from <001> and <110> properties. Implemented with criteria for variant and phase evolutions in the model, simulations reproduce the observed hysteresis loops, remanent strain and remanent polarization. The results have been published at *Acta Materialia* [52].

3.1 Introduction

Single crystals of relaxor rhombohedral $[Pb(Zn_{1/3}Nb_{2/3})O_3]_{(1-x)}$-$[PbTiO_3]_x$ (PZN-xPT, 0<x<0.1) and $[Pb(Mn_{1/3}Nb_{2/3})O_3]_{(1-x)}$-$[PbTiO_3]_x$ (PMN-xPT, 0<x<0.35) have been used for electromechanical transducers and actuators in a broad range of advanced applications such as medical ultrasonic imaging and underwater communication

[18,20,22,112,113]. There have recently been many research efforts directed at understanding polarization and its reorientation (switching) in these single crystals. Much of the published literature has focused on the properties of <001> oriented and poled rhombohedral crystals due to their high electromechanical coupling coefficient (k_{33} > 90%) and high piezoelectric constant (d_{33} > 2000 pC/N) [8,9,114-116]. Ujiie and Uchino [57] observed domain reversal in PZN-xPT under <111> electric field using a CCD microscope system. The electromechanical properties of <111> cuts are relatively low [59]. Jie Chen *et al.* [117] measured the electromechanical and dielectric properties of <110> oriented PMN-31%PT single crystals and reported a coupling constant as high as 0.91.

Relaxor PZN-xPT and PMN-xPT single crystals display temperature and field dependent phase transformations [9,65]. Fu and Cohen [66] discussed polarization rotation paths based on first principles calculations. Vanderbilt and Cohen [84] developed a thermodynamic framework to describe three possible monoclinic phases by means of an eighth-order expansion from Devonshire theory. Noheda *et al*. [33] demonstrated the presence of multiple phases in PZN-8%PT using synchrotron radiation and discussed the contributions of a monoclinic phase to the <001> piezoelectric response. Their experimental results show that once the <001> crystal has been driven through the rhombohedral to tetragonal phase transition, there is a permanent phase change in the crystal. This is also suggested by Viehland's experimental results [67], which indicate a change of coercive field for 180° polarization reorientation after the material has been driven through the phase change and back. Lu *et al.* [34] and Priya *et al.* [118] reported observations of the orthorhombic ferroelectric phase in PZN-8%PT and PMN-33%PT

single crystals. Optical observation [34] showed that a <110> (or <011>) oriented crystal can be poled to a <111> twinned multi-domain state (rhombohedral phase) or a <110> mono-domain state (orthorhombic phase).

This work attempts to clarify questions regarding the source of the enhanced electromechanical behavior. It could be the direct result of the engineered rhombohedral domain state or that the engineered domain state crystal comprises a multiphase system. The results of this work present evidence that the extraordinarily large <001> coefficients do not require contributions from other than the rhombohedral phase. Understanding the switching behavior and field induced phase transitions, however, is still an important aspect of understanding and manipulating the behavior of these crystals.

In Chapter 2 the crystal variants and their evolution upon field induced polarization reorientations and phase transitions were reviewed. This approach to describing the crystals was used to construct a model of the macroscopically observed crystal behavior based on the volume average microscopic behavior. The predicted macroscopic behavior was used to design experiments that enable the determination of the full set of <111> piezoelectric coefficients. Response of <110> orientation cut of PZN-4.5%PT single crystals under electric field cycles was measured, and the measured coefficients provide sufficient information to compute the piezoelectric properties of the <001> and the <110> crystal cuts. A computational model was then used to reproduce the major hysteresis loops including phase changes, for the <001> and <110> cuts. The energy threshold for switching and phase transformations gives insight into the role of the domain state in the process.

3.2 Experimental Measurement

3.2.1 Specimen Preparation and Test Procedure

PZN-4.5%PT single crystals were grown and cut along specified crystallographic planes (by TRS Technologies, State College, PA) for characterization. TRS provided a complete set of measured piezoelectric coefficients for <001> poled PZN-4.5%PT and partial measured <111> piezoelectric coefficients. They provided several <110>-cut crystals for additional measurements of piezoelectric behavior and coefficients. Three specimens of PZN-4.5%PT transparent rhombohedral single crystals 5mm×5mm×10mm were used in this study. The specimens were cut with the two 5mm×5mm faces perpendicular to the <001> crystal direction and one of the 5mm×10mm faces perpendicular to the <110> direction. The specimens were initially unpoled with random domain orientations (equal volume fractions of all variants). This was taken as the reference state of zero remanent polarization and zero remanent strain.

Unpolished for the first specimen and polished for the other two, the two opposite <110> faces were sputtered with gold electrodes. The other 4 faces were polished with 1-micron diamond. Tests of the first two specimens involved using strain gages to measure strain and application of electric field to induce a piezoelectric response. For the first specimen, 0-45-90° strain gage rosettes were bonded to the two <1-10> faces, with gages parallel to the <110> direction, the <001> direction, and 45° between. Polyimide film of 25-micron thick was bonded between the specimen and the strain gage rosettes to prevent short circuit under high voltage. All bonding was done with M-bond 200, Measurements Group, Vishay. For the second specimen, strain gage rosettes were bonded to the grounded gold electrode, with gages parallel to <1-10> direction and <001> direction.

For the third specimen, as shown in Figure 3-1, a linear variable differential transducer (LVDT) was used to measure displacement in the loading direction (<110> direction). The specimen with strain gages attached was placed in a fluorinent (3M) bath to prevent high voltage arcing.

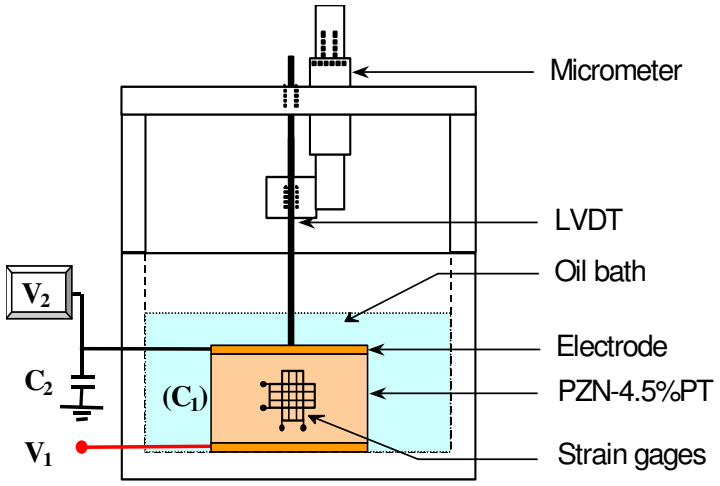

Figure 3-1. Measurement of PZN-4.5%PT single crystals under electric field loading.

The experiments were to measure the strain-field and polarization-field relations under <110> electric field. The electric field was applied using a high voltage amplifier driven by a function generator in triangle wave mode, linearly increased from zero then decreased back to zero at a frequency of 0.1 Hz. Strain gages were connected to the Wheatstone bridge based signal conditioners and the output recorded. High frequency noise in the strain gage circuits was blocked using capacitor-resistor filters. The bridges were each calibrated and balanced prior to the initial loading. Refer to Figure 3-1, the

electric displacement was measured using a modified Sawyer-Tower circuit with a 10 μF series capacitor (C_2), which is much larger than the capacity of the specimen (C_1). Voltage on the capacitor (V_2, which is much smaller than the applied voltage, V_1) was monitored using an electrometer. Output of the electrometer was recorded. Electric displacement was determined by the charge on the series capacitor ($Q_2 = C_2V_2$, which equals to the charge on the specimen, Q_1) divided by the specimen electrode area. Data were recorded using a 16-bit digital data acquisition system.

3.2.2 Experimental Results

The results of three different tests are combined and shown in Figure 3-2. Also plotted in the figure are results from a crystal variant model, which will be discussed in the next section. The results of these tests were surprising and somewhat remarkable, therefore TRS produced additional crystals and repeated the measurements. The results were independently confirmed. According to the strain data in Figure 3-2a, the piezoelectric coefficient d_{33} (in <110> loading direction) is positive, and d_{31} (<110> to <001> direction) is large and negative. Figure 3-2a shows the remnant strain in the <001> direction is close to zero and in the <1-10> direction is about 0.07%. Figure 3-2b shows the *D-E* hysteresis curve in the loading direction. When the applied electric field was higher ($E_{r\text{-}o}$), a second jump of strain and electric displacement occurred. This is believed to be due to a rhombohedral to orthorhombic phase change. A reverse jump occurred when the electric field was unloaded to $E_{o\text{-}r}$, which was slightly smaller than $E_{r\text{-}o}$. The phase change induces only a small change of remanent electric displacement in the <110> direction while a large change of remanent strain.

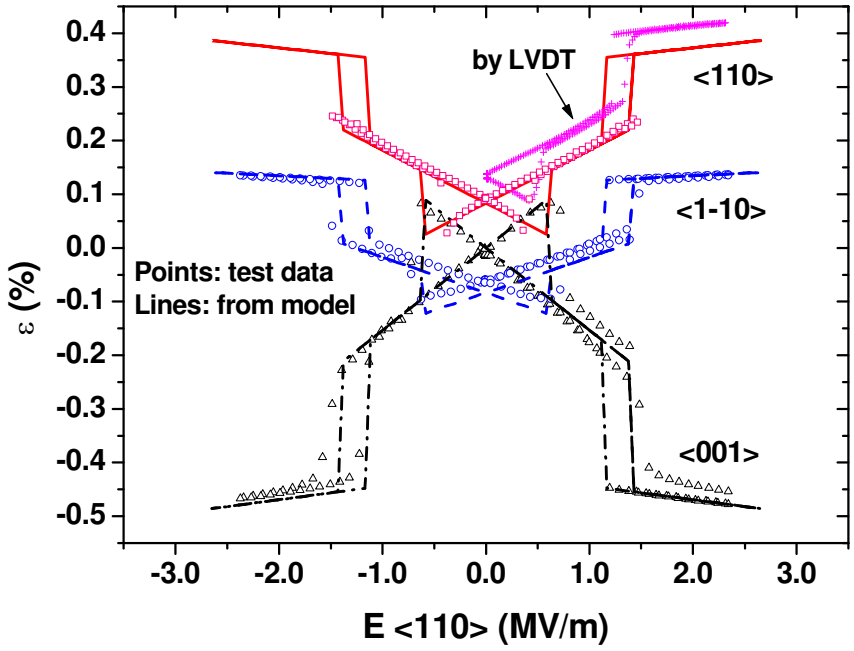

(a)

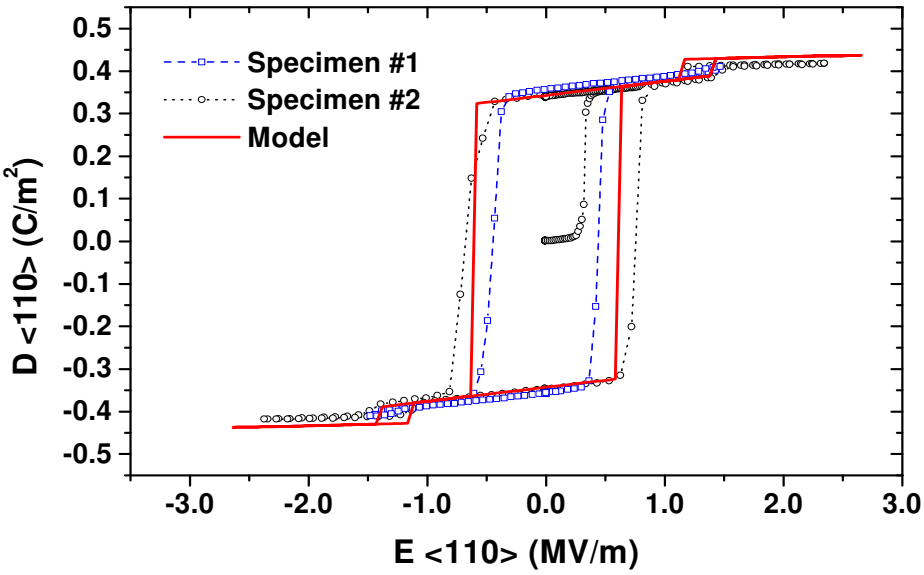

(b)

Figure 3-2. Polarization switching and phase change under <110> electric field. (a) Strain versus electric field (the LVDT gave a little higher strain value); (b) Electric displacement versus electric field.

Figure 3-2 shows an increase of coercive field after polarization switching and phase change. When a reverse electric field was applied to the specimen after it had undergone a phase change, it revealed a coercive field almost twice of the initial coercive field value. This seems to indicate a permanent change of domain state or a permanent introduction of a second phase.

The specimens were translucent prior to application of electric field and transparent after they were polarized. Cracks developed beneath the unpolished electrodes, parallel to the applied electric field, as shown in Figure 3-3a. When the surfaces were polished before gold sputtering, cracks were only found at the edge of the electrode (Figure 3-3b). It is likely that electric field caused stress concentrations at the unpolished electrode surfaces. The gold electrodes were removed from the third specimen after test, and domain structure was observed in the poling direction as shown in Figure 2-6c. The two <110> surfaces of the first specimen were polished after the test and domains interacting with cracks were also observed (Figure 3-4). Such domain structure was observed only in the <110> poling direction.

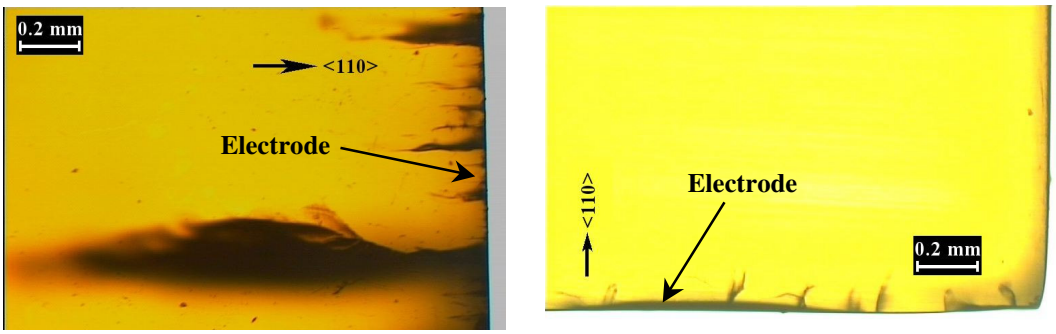

(a) (b)

Figure 3-3. Cracking under electric field (viewed in the <1-10> direction). (a) Cracks along the electric field direction beneath the electrode with unpolished surface; (b) Short cracks at the edge of the electrode with polished surface.

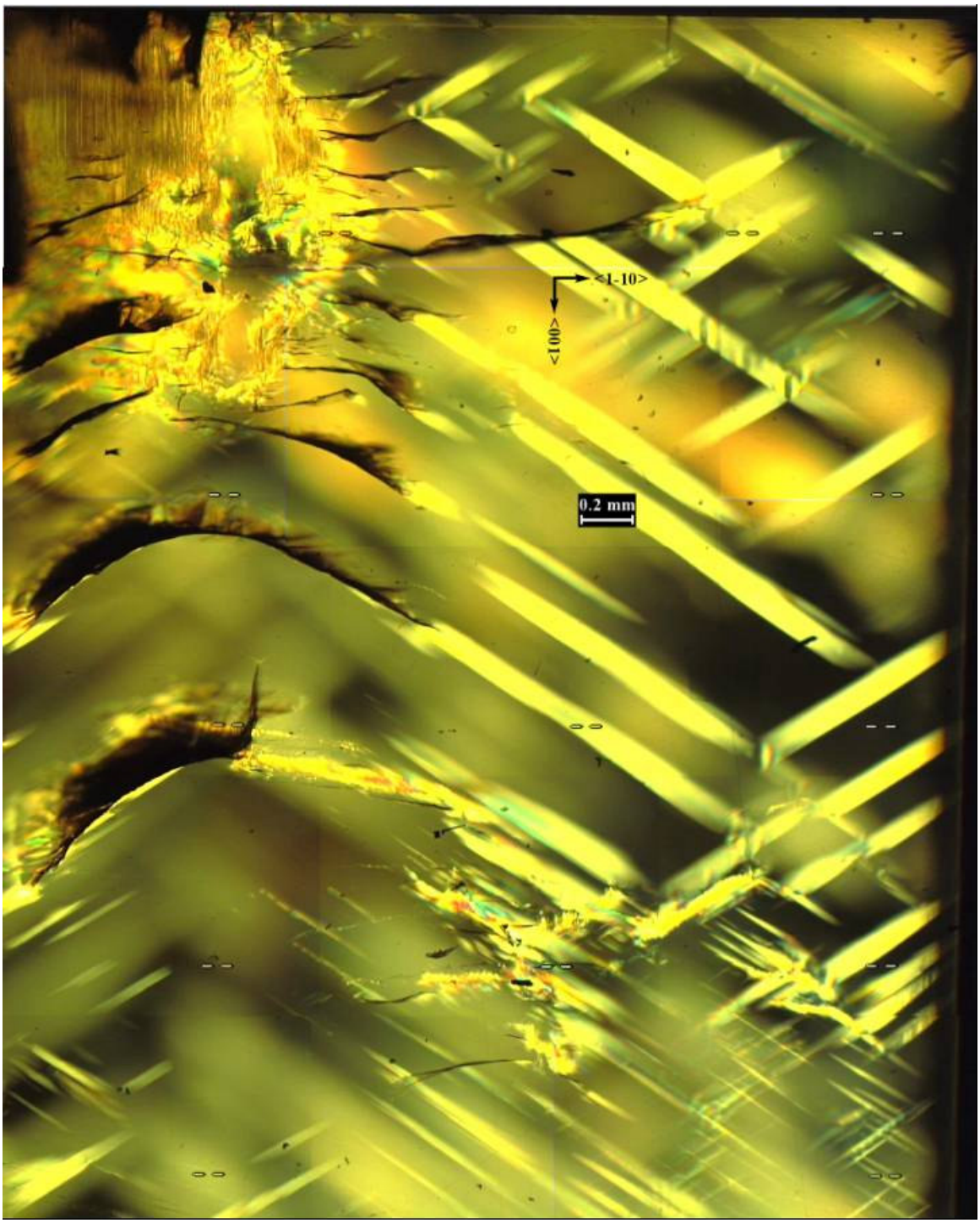

Figure 3-4. Domain structure and cracks observed along the <110> poling direction.

The piezoelectric properties of <110> cut PZN-4.5%PT obtained from all tests are combined and listed in Table 3-1 as properties of the rhombohedral phase and orthorhombic phase. d_{31} , d_{32} and d_{33} for the rhombohedral phase were obtained from test data at small electric field. Values for the orthorhombic phase were obtained by linear regression of the data at high electric field.

Table 3-1. Measured electromechanical properties of PZN-4.5%PT single crystals.

	Rhombohedral, <110> cut	Orthorhombic, <110> cut
d_{31} (10^{-12} C/N)	690	97
d_{32} (10^{-12} C/N)	-1670	-256
d_{33} (10^{-12} C/N)	980	209
E_c^{180} (MV/m)	0.32, 0.63*	N/A
$E_{r\text{-}o}$ / $E_{o\text{-}r}$ (MV/m)	1.41	1.12
$\varepsilon_{11}^r, \varepsilon_{22}^r, \varepsilon_{33}^r$ (με)	-78, -629, 956	-4180, 1150, 3480
D^r (C/m^2)	0.36	0.40
K_{33}^{σ} (ε_0)	3727	700

* after the rhombohedral-orthorhombic phase change

3.3 Crystal Variant Based Modeling

A computational model was developed to simulate the behavior of the single crystals with an engineered multi-domain state based on the properties of crystal variants (domains) and the volume fraction of each crystal variant present in the crystals.

3.3.1 Engineered Domain State and Crystal Variants

A crystal variant is defined by the local polarization direction of a domain in the crystal. Given the tensor properties of a variant (elastic, dielectric, and piezoelectric, its spontaneous polarization and spontaneous strain), its properties in any other direction can be computed using orthogonal transformations for tensors. If the volume fraction of each variant within the crystal is known and variant interaction can be neglected, the overall properties of the single crystal can be calculated by volume averaging. This leads to a method for predicting the properties of the engineered domain state single crystal from the properties of the variants.

The calculation of the <111> single domain properties is based on the assumption that the <001> poled rhombohedral crystal comprises equal volume fractions of four crystal variants (<111>, <-111>, <1-11>, <-1-11>), and the <110> poled crystal comprises equal volume fractions of two crystal variants (<111>, <11-1>), as shown in Figure 3-5. Orthogonal transformations and volume averaging of the crystal variant properties are used to relate the electromechanical tensors of the <111> poled single domain crystal to those of multi-domain crystals poled in other directions.

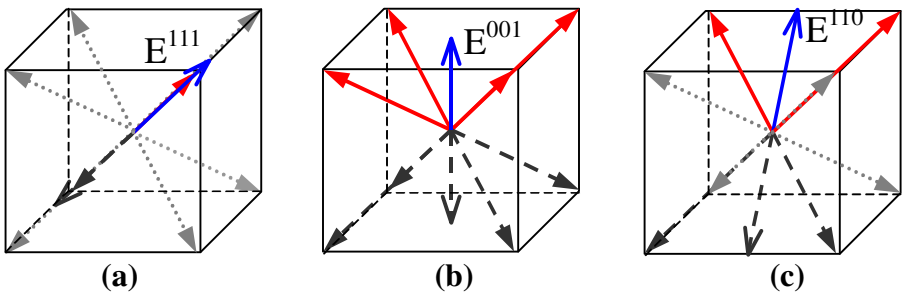

Figure 3-5. Multi-domain models. (a) Single domain with electric field (**E**) in <111> direction; (b) 4-domain state with **E** in <001> direction; (c) 2-domain state with **E** in <110> direction.

The phases present in relaxor PZN-xPT and PMN-xPT single crystals depend on their composition and temperature [34,42]. Applied electric field or stress also induce phase changes. Transformations from the cubic to the tetragonal, rhombohedral or orthorhombic phase result in a spontaneous polarization in <001>, <111> or <110> direction, associated with shape and volume change of the parent cubic structure. A region in the single crystal with the same polarization direction is called a domain (or a crystal variant). The *4mm* tetragonal phase has 6 equivalent polarization directions, or 6 variants. Accordingly the *3m* rhombohedral phase has 8 variants and the *mm2* orthorhombic phase has 12 variants.

Local coordinates for the variants are defined as in Figure 3-6. Under these coordinates the components of the elastic, dielectric and piezoelectric tensors for each phase are uniquely defined. The constitutive law for a crystal variant can be expressed in local coordinates as:

$$\varepsilon_{ij} - \varepsilon_{ij}^{s} = s_{ijkl}^{E}\sigma_{kl} + d_{nij}E_{n} \tag{3-1a}$$

$$D_{m} - D_{m}^{s} = d_{mkl}\sigma_{kl} + K_{mn}^{\sigma}E_{n} \tag{3-1b}$$

where σ_{ij} and E_i are applied stress and electric field, ε_{ij} and D_i are the total strain and the total electric displacement, ε_{ij}^{s} and D_i^{s} are the spontaneous strain and electric displacement, s_{ijkl}^{E}, d_{ijk} and K_{ij}^{σ} are the elastic, piezoelectric and dielectric tensors.

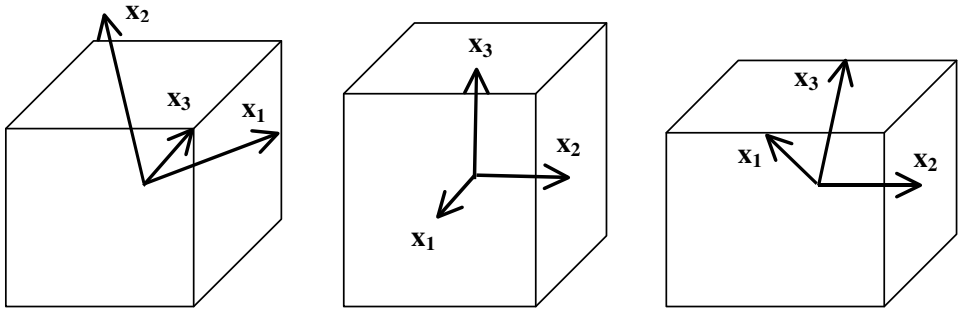

Figure 3-6. Local coordinates of crystal variants. The x_3 direction lies parallel with the spontaneous polarization. (a) For a <111> rhombohedral variant, with x_1-x_2-x_3 in <-110>-<-1-12>-<111> directions; (b) For a <001> tetragonal variant, with x_1-x_2-x_3 in <100>-<010>-<001> directions; (c) For a <101> orthorhombic variant, with x_1-x_2-x_3 in <10-1>-<010>-<101> directions.

3.3.2 Orthogonal Transformation and Volume Averaging

The properties of the crystal comprised of multiple variants are defined with respect to a global coordinate system. Elastic, piezoelectric and dielectric tensors are respectively fourth, third and second order tensors. The spontaneous strain is a second order tensor and the spontaneous electric displacement is a vector. The orthogonal transformations of these physical properties between two coordinate systems are given by:

$$s_{ijkl}^{(2)} = a_{ip} a_{jq} a_{kr} a_{ls} s_{pqrs}^{(1)} \tag{3-2a}$$

$$d_{ijk}^{(2)} = a_{ir} a_{js} a_{kt} d_{rst}^{(1)} \tag{3-2b}$$

$$K_{mn}^{(2)} = a_{mp} a_{nq} K_{pq}^{(1)} \tag{3-2c}$$

$$\varepsilon_{ij}^{s(2)} = a_{ip} a_{jq} \varepsilon_{pq}^{s(1)} \tag{3-2d}$$

$$D_{m}^{s(2)} = a_{mn} D_{n}^{s(1)} \tag{3-2e}$$

The superscripts (1) and (2) in Equation 3-2 refer to two coordinate systems, and $a_{ir} = \cos\theta_{ir}$ are the direction cosines between these two coordinate systems. Summation on repeated indices is implied.

The modeling approach assumes that the interactions between variants can be neglected and the overall elastic, piezoelectric, dielectric coefficients, the remanent strain the remanent electric displacement of the engineered domain state crystal can be calculated by volume averaging from the properties of each variant present using the following equations:

$$\hat{s}_{ijkl} = \frac{1}{V}\int_V s_{ijkl}\,dv = \sum_{\alpha=1}^{n} f_\alpha s_{ijkl}^{(\alpha)} \tag{3-3a}$$

$$\hat{d}_{ijk} = \frac{1}{V}\int_V d_{ijk}\,dv = \sum_{\alpha=1}^{n} f_\alpha d_{ijk}^{(\alpha)} \tag{3-3b}$$

$$\hat{K}_{ij} = \frac{1}{V}\int_V K_{ij}\,dv = \sum_{\alpha=1}^{n} f_\alpha K_{ij}^{(\alpha)} \tag{3-3c}$$

$$\hat{\varepsilon}_{ij}^{r} = \frac{1}{V}\int_V \varepsilon_{ij}^{s}\,dv = \sum_{\alpha=1}^{n} f_\alpha \varepsilon_{ij}^{(\alpha)} \tag{3-3d}$$

$$\hat{D}_{m}^{r} = \frac{1}{V}\int_V D_{m}^{s}\,dv = \sum_{\alpha=1}^{n} f_\alpha D_{m}^{(\alpha)} \tag{3-3e}$$

where n is the number of variants, and f_α is the volume fraction of variant α.

According to Equation 3-3d and 3-3e, if the spontaneous polarization and spontaneous strain for the <111> variant are respectively D^s and ε^s, then the remanent polarization for the 4-variant <001> poled state and the 2-variant <110> poled state are accordingly $\sqrt{\frac{1}{3}}D^s$ and $\sqrt{\frac{2}{3}}D^s$, there is no remanent strain for the <001> poling state,

while the strains for the <110> poling state in the three coordinate directions are -0.5ε^s : 0 : 0.5ε^s . Experimental results are in good agreement with these relations [8].

3.3.3 Evolution of Variant Volume Fractions

External loading causes polarization reorientation among possible poling directions. There are 90°/180° possible polarization reorientations in the tetragonal phase, 109.5°/70.5°/180° reorientations in the rhombohedral phase and 60°/90°/120°/180° reorientations the orthorhombic phase. Energy based switching criteria have been used to simulate the behavior of ferroelectric ceramics [103-105]. A general energy based switching criterion under external loading (stress and electric field) was established as follows [103]:

$$w = \sigma_{ij}\Delta\varepsilon_{ij} + E_i\Delta D_i = 2E_cD^s \tag{3-4}$$

where σ_{ij} and E_i are applied stress and electric field, $\Delta\varepsilon_{ij}$ and ΔD_i are the change of strain and electric displacement during switching.

Energy based criteria may also be used in the model for phase transformations. It is reasonable to consider a criterion for external field induced phase change as a function of applied electric field and stress [86]:

$$\sigma_{ij}\Delta\varepsilon_{ij}^s + E_i\Delta D_i^s = k_p \cdot E_cD^s \tag{3-5}$$

where $\Delta\varepsilon_{ij}^{s}$ is the spontaneous strain change between two variants, ΔD_i^s is the spontaneous electric displacement change between two variants, E_c is the coercive field of polarization switching, and k_p is a factor related to the energy level of that phase.

This model assumes that all variants experience the same external stress and electric field during switching, i.e., no local inter-variant fields, and that reorientation associated changes in anisotropy make a negligible contribution to the energy change. The model doesn't consider the role of domain walls in the reorientation process. Improved modeling of the behavior of the crystals will require more detailed variant evolution laws based on the underlying process of domain wall motion and inter-domain strain and polarization compatibility. This requires a better description of the criteria for different kinds of switching and phase changes between crystal variants.

This approach leads to the prediction of hysteresis loops with steps as shown in Figure 3-7. E_c, ε^s, D^s represent respectively the coercive field, spontaneous strain and spontaneous electric displacement of a <111> variant. The simulation begins with equal volume fractions of each crystal variant. When electric field is applied in the <111> direction, the variants on which the maximum external work would be done by a reorientation reorient first (180° switching). This is followed, at a higher applied field, by reorientation of the remaining variants (109.5° then 70.5° reorientation). Similar effects are seen for the <110> oriented crystals. For the <001> oriented crystals, all reorientation occurs at the same field level.

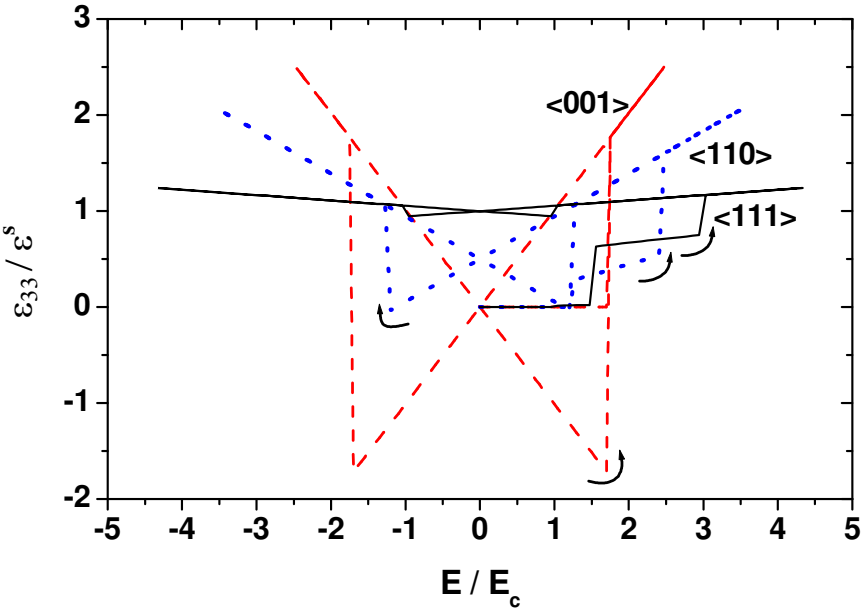

(a)

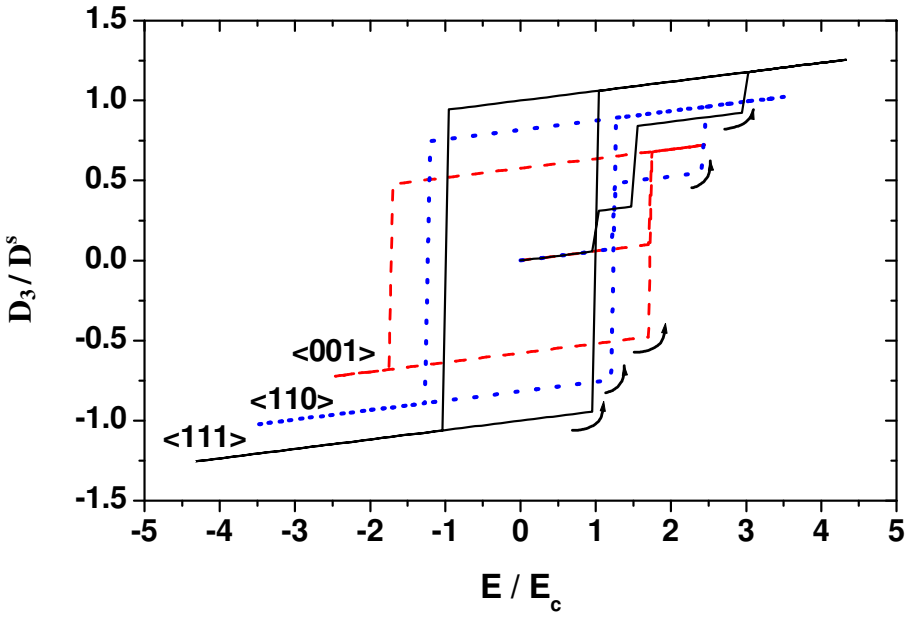

(b)

Figure 3-7. Repolarization of the rhombohedral crystal under electric field with a work criterion $w = w_c$. (a) Strain versus electric field; (b) Electric displacement versus electric field.

A trend is observed in this simulation with respect to the coercive field that is inconsistent with experimental observation. In this simulation, the coercive field is lowest for the <111> oriented crystal and becomes successively higher for the <110> and <001> orientations. This is due to reorientation driving force being proportional to the component of electric field aligned with the rhombohedral directions. The observed behavior follows the opposite trend [8,60]. This gives some insight onto the role of domain walls in the reorientation process. The <111> crystal is polarized into a single domain since the electric field is aligned with a polar direction. Subsequent 180° reorientation requires the initiation of a domain wall and its subsequent sweeping through the entire crystal. The <110> crystal is polarized into a poly-variant state. In this case, reorientation only requires existing domain walls to move the length of existing domains. This reduces possible energy barriers associated with nucleation of domain walls and reduces the distance domain walls must move to fully reorient the polarization of the crystal. The <001> oriented crystal has an incompatible domain state. Two of the variants can coexist, being separated by domain walls across which the normal component of electric displacement is zero and the displacement jump is zero. This type of wall has no associated local stress or electric field. Introduction of the second two variants cannot be accomplished without introduction of some incompatible domain walls. This may play a role in the further reduction of the observed coercive field. It was also observed that once the <110> cut crystal has been driven through a rhombohedral to orthorhombic phase change the coercive field nearly doubles. It is possible that there are two distinct domain states: The first, the micro-polar state of the relaxor and the second, the macro-domain state.

Although this simple model produced reasonable results for the behavior of a ceramic, its limitations are evident when modeling single crystals. Exact <001> orientation results in four equivalent energy states for the four variants. An obvious choice would be to then set each of the four associated volume fractions equal. A slight tilt in one direction would give one of the variants a slightly lower energy state and result in this state being assigned a volume fraction of one with markedly different crystal properties. This is not consistent with experimental observations and points to the need to develop more accurate evolution laws based on the underlying process of domain wall motion. Accurate modeling of the behavior of the crystals requires that the evolution law be modified to include a different coercive field for different crystal orientation cuts.

3.3.4 Calculation of Piezoelectric Coefficients for Different Orientation Cuts

Here Equation 3-3b is used to calculate the unknown properties of the single domain <111> poled rhombohedral phase from measurements of other orientation cuts. The <001> poled crystal is assumed to comprise equal volume fractions of four rhombohedral crystal variants and the <110> poled crystal comprises equal volume fractions of two rhombohedral crystal variants. This provides a system of linear equations from which the <111> properties can be computed. The resulting computed <111> properties are compared with measured <111> properties and discrepancies are found to be within the uncertainty of the measurements. After the full set of <111> properties are available, the model is used to compute the properties of crystals with different orientation cuts as long as the crystal variant volume fractions can be determined.

The components of the third-order piezoelectric tensor are often represented in matrix notation according to the following correlation:

Matrix notation	d_{31}	d_{32}	d_{33}	d_{24}	d_{15}	d_{16}
Tensor notation	d_{311}	d_{322}	d_{333}	d_{223}	d_{113}	d_{112}

The symmetry of the elastic, dielectric, and piezoelectric tensors and the spontaneous strain and polarization for each phase are associated with the crystal symmetry of that phase [28]. Under the local coordinates described in Figure 3-6, the tetragonal phase (with a *4mm* symmetry) has 5 nonzero piezoelectric coefficients $d_{31} = d_{32}$, d_{33}, and $d_{15} = d_{24}$, the properties in x_1 and x_2 directions are identical by symmetry. The rhombohedral phase has a trigonal class *3m* symmetry with associated 8 nonzero components $d_{31} = d_{32}$, d_{33}, $d_{15} = d_{24}$ and $d_{16} = 2d_{21} = -2d_{22}$. The orthorhombic phase has *mm2* symmetry with 5 nonzero components: d_{31}, d_{32}, d_{33}, d_{15}, d_{24}. The piezoelectric tensors for these three phases can be expressed in matrix format as:

$$[d_{ij}]^T = \begin{bmatrix} 0 & 0 & 0 & 0 & d_{15} & 0 \\ 0 & 0 & 0 & d_{15} & 0 & 0 \\ d_{31} & d_{31} & d_{33} & 0 & 0 & 0 \end{bmatrix}$$

$$[d_{ij}]^R = \begin{bmatrix} 0 & 0 & 0 & 0 & d_{15} & d_{16} \\ 0.5d_{16} & -0.5d_{16} & 0 & d_{15} & 0 & 0 \\ d_{31} & d_{31} & d_{33} & 0 & 0 & 0 \end{bmatrix}$$

$$[d_{ij}]^O = \begin{bmatrix} 0 & 0 & 0 & 0 & d_{15} & 0 \\ 0 & 0 & 0 & d_{24} & 0 & 0 \\ d_{31} & d_{32} & d_{33} & 0 & 0 & 0 \end{bmatrix}$$

As shown in Figure 3-5, the 4-variant <001> poling state has *4mm* symmetry and the 2-variant <110> poling state has *mm2* symmetry, therefore the global coordinates are

chosen as described in Figure 3-6b,c. For the 4-variant <001> poling model, the orthogonal transformations for the four rhombohedral variants from their local coordinates to the <001> coordinate system and volume averaging (equal volume fractions $f_1 = f_2 = f_3 = f_4 = 1/4$) give three equations:

$$d_{31}^{001} = d_{32}^{001} = 0.385 d_{31}^{111} + 0.192 d_{33}^{111} - 0.192 d_{15}^{111} + 0.136 d_{16}^{111} \quad \text{(3-6a)}$$

$$d_{33}^{001} = 0.385 d_{31}^{111} + 0.192 d_{33}^{111} + 0.385 d_{15}^{111} - 0.272 d_{16}^{111} \quad \text{(3-6b)}$$

$$d_{24}^{001} = d_{15}^{001} = -0.192 d_{31}^{111} + 0.192 d_{33}^{111} + 0.096 d_{15}^{111} + 0.136 d_{16}^{111} \quad \text{(3-6c)}$$

The superscripts of the piezoelectric coefficients refer to the poling directions. For the two-variant <110> poling model with volume fractions $f_1 = f_2 = 1/2$, there is another set of equations:

$$d_{31}^{110} = 0.816 d_{31}^{111} - 0.289 d_{16}^{111} \quad \text{(3-7a)}$$

$$d_{32}^{110} = 0.544 d_{31}^{111} + 0.272 d_{33}^{111} - 0.272 d_{15}^{111} + 0.192 d_{16}^{111} \quad \text{(3-7b)}$$

$$d_{33}^{110} = 0.272 d_{31}^{111} + 0.544 d_{33}^{111} + 0.272 d_{15}^{111} + 0.096 d_{16}^{111} \quad \text{(3-7c)}$$

$$d_{24}^{110} = -0.272 d_{31}^{111} + 0.272 d_{33}^{111} + 0.136 d_{15}^{111} + 0.192 d_{16}^{111} \quad \text{(3-7d)}$$

$$d_{15}^{110} = 0.408 d_{15}^{111} - 0.289 d_{16}^{111} \quad \text{(3-7e)}$$

These equations give the relations between the volume average piezoelectric coefficients of the multi-variant states and those of the single <111> variant. Equations 3-6a~c are linearly independent equations with experimental results for the left hand side terms for many relaxor crystals. For the two-variant <110> poling model, only three of the equations 3-7a~e are linearly independent (equations 3-7a~c). Unfortunately none of equations 3-6a~c is linearly independent of equations 3-7a~c. For these reasons, one of the <111> piezoelectric coefficients is needed in the calculations.

The piezoelectric coefficients for <001> oriented relaxor crystals PZN-4.5%PT, PZN-8%PT and PMN-30%PT are available [44,119,120]. Some of the piezoelectric coefficients for these crystals poled along <111> and <110> are also available. The measured data is listed in Table 3-2. These crystals are in rhombohedral phase close to the morphotropic phase boundary (MPB) at room temperature [42,43]. Here we use the model to compute the unknown piezoelectric coefficients of these three kinds of crystals from the measured piezoelectric coefficients.

Table 3-2. Measured piezoelectric properties of relaxor single crystals (pC/N) (at room temperature)

Specimen orientation		d_{31}	d_{32}	d_{33}	d_{24}	d_{15}	d_h
<111>	PZN-4.5%PT[59]	-35		125			
	PZN-8%PT[121]	-42					
	PMN-30%PT[a]	-60±10		125±25			
<001>	PZN-4.5%PT[44]	-970		2000	140		
	PZN-8%PT [120]	-1455		2890	159		50 [b]
	PMN-30%PT [a]	-921		1981	191		
<110>	PZN-4.5%PT	690	-1670	980			
	PZN-8%PT						
	PMN-30%PT						

[a] from TRS Technologies, State College, PA; [b] from reference [119].

Experimental measurements show that the hydrostatic piezoelectric coefficient d_h is about 55pC/N for both <111> and <001>-poled PZN-4.5%PT, but there is a discrepancy

with $d_h = d_{31} + d_{32} + d_{33}$ from the <001> measurements [59]. Here d_{31}^{111}, d_{33}^{111} together with d_{33}^{001}, d_{15}^{001} (or d_{32}^{110}, d_{33}^{110} for the <110> case) are used to calculate the remaining <111> piezoelectric coefficients. The calculated <111> piezoelectric coefficients are then put back into equations 3-6 and 3-7 to calculate other components. The results are listed in Table 3-3, with the input terms (measured values) in parentheses. The results indicate very large d_{15} and d_{16} coefficients for the <111> single variant, which contribute to the large differences of piezoelectric properties for the three orientations. The variations between the measured and computed data and the variations between the two sets of computed <111> data are consistent with the magnitude of the experimental errors, which include uncertainty in specimen geometry, orientation, non-equal volume fractions of variants, complex domain structures and possible multiphase states.

Table 3-3. Calculated piezoelectric properties of PZN-4.5%PT (pC/N)
(with the input terms in parentheses)

Specimen orientation		d_{31}	d_{32}	d_{33}	d_{24}	d_{15}	d_{16}
<111>	from <001> data	(-35)		(125)	3824		-1902
	from <110> data	(-35)		(125)	4322		-2642
<001>	from <001> data	-984		(2000)	(140)		0
<110>	from <110> data	734	(-1670)	(980)	123	2527	0

The piezoelectric coefficients for the <111> and <110> orientation cuts of PZN-8%PT crystals were also computed from the coefficients of <001> cuts and d_{31}^{111} = -42 pC/N, and the results are listed in Table 3-4. Note that d_h = 50 pC/N in <001> was used

as an input instead of the d_{31}^{001} value in the calculation. Compared to the PZN-4.5%PT, the PZN-8%PT crystal variants have higher piezoelectric coefficients therefore exhibit higher performance in all orientations. This is the result of the composition being very near a morphotropic phase boundary. The result is that the rhombohedral phase is less stable in PZN-8PT. This places additional restrictions of the allowed field levels and temperature range.

Table 3-4. Calculated piezoelectric properties of PZN-8%PT (pC/N)
(with the input terms in parentheses)

Specimen orientation	d_{31}	d_{32}	d_{33}	d_{24}	d_{15}	d_{16}
<111>	(-42)		171	5386		-2941
<001>	-1420 (d_h=50)		(2890)	(159)		0
<110>	815	-2008	1264	225	3048	0

The piezoelectric coefficients were also computed for the <111> and <110> orientation cuts of PMN-30%PT crystals from the coefficients of <001> cuts and $d_{31}^{111}, d_{33}^{111}$ values. The results are listed in Table 3-5. The piezoelectric properties of this crystal are close to those of the PZN-4.5%PT. The measured piezoelectric coefficients of <110> poled PMN-33%PT crystals [34] are much larger than the predictions for the PMN-30%PT. This is possibly due the presence of the monoclinic phase (M_A) in the PMN-33%PT crystals. Additional equations are required to describe the crystal variants of this phase.

Table 3-5. Calculated piezoelectric properties of PMN-30%PT (pC/N)
(with the input terms in parentheses)

Specimen orientation	d_{31}	d_{32}	d_{33}	d_{24}	d_{15}	d_{16}
<111>	(-60)		(125)	3968		-1664
<001>	-989		(1981)	(191)		0
<110>	431	-1399	972	270	2100	0

3.3.5 Simulations of Switching and Phase Changes

The crystal variant model is used to describing the evolution of polarization switching and phase changes by including the polarization switching and phase change criteria. By setting up volume fractions of crystal variants as functions of applied loads (electric field, stress and temperature), a computational model can then reproduce the major hysteresis loops, including polarization switching and phase changes.

Here the model is used to simulate the strain versus electric field curves and electric displacement versus electric field hysteresis loops during polarization switching and phase change. Figure 3-8 shows an overlay of the simulation on the measured hysteresis loops of polarization switching for PZN-4.5%PT with electric field along <001> orientation. This is a simulation of the 4-variant <001> poled model with switching law.

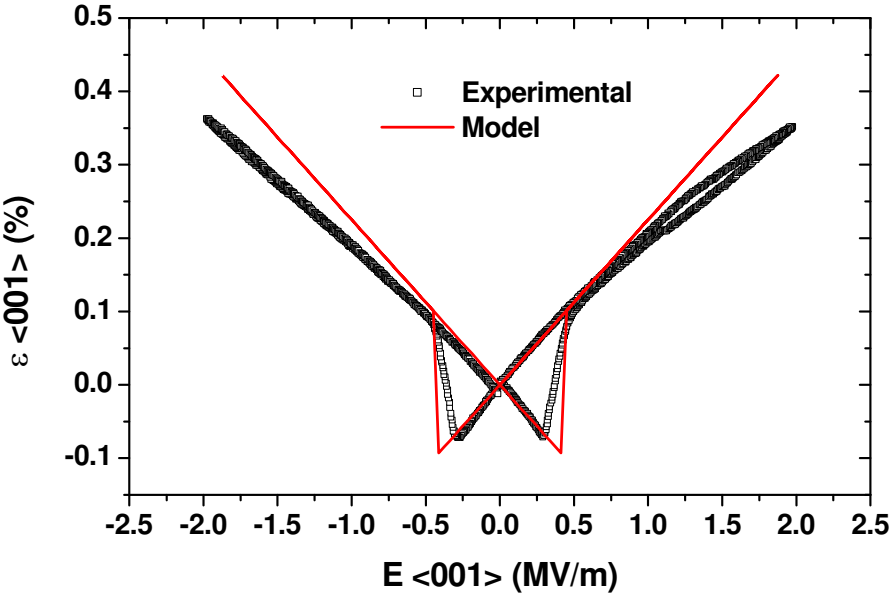

(a)

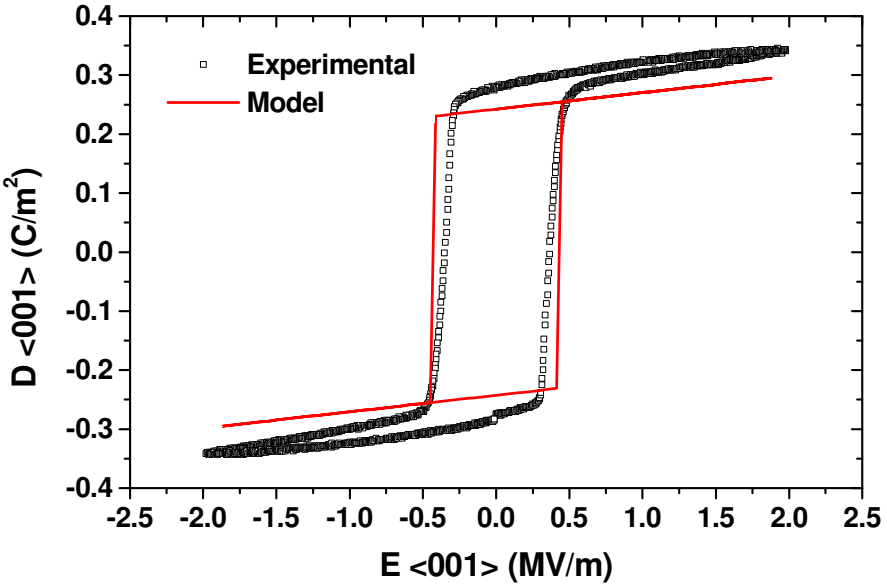

(b)

Figure 3-8. Domain switching under <001> electric field. (a) Strain versus electric field; (b) Electric displacement versus electric field.

At higher field levels the <001> cut and poled crystal undergoes a phase transformation to a tetragonal structure [8] and as observed in last section, the <110> cut undergoes a phase transformation to an orthorhombic structure. During unloading a reverse phase transformation occurs. Figure 3-2 includes the simulation and the experimental results for PZN-4.5%PT with electric field applied in <110> direction. In this case the strains in three directions and the electric displacement during polarization switching and the orthorhombic-rhombohedral phase change were simulated, with implementation of the two-variant <110> model and the polarization switching and phase change criteria. The two relevant field strengths at phase change are the rhombohedral to orthorhombic phase change field $E_{\text{r-o}}$ and orthorhombic to rhombohedral phase change field $E_{\text{o-r}}$. These values are implemented in the model to simulate the phase change.

3.4 Concluding Remarks

Electromechanical properties and phase changes of <110> oriented PZN-4.5%PT single crystals were studied using a combination of experimental, analytical, and numerical techniques. Enhanced piezoelectric coefficients (d_{31} = 690 pC/N, d_{32} = -1670 pC/N) were measured and a rhombohedral to orthorhombic phase transformation was observed under <110> electric field loading. The very large d_{31} and d_{32} values with $d_{32} \cong -\frac{1}{2} d_{31}$ make this crystal cut an excellent candidate for bending mode applications. It was observed that once the <110> cut crystal has been driven through a rhombohedral to orthorhombic phase change, the coercive field nearly doubles. There may be two distinct domain states, one present before and one after the phase change. This would be

consistent with the known behavior of relaxor materials in which a micro-polar relaxor domain state can be coerced into a macro ferroelectric domain state.

A model based on properties of crystal variants and volume averaging was developed and verified. Piezoelectric coefficients for <111> PZN-4.5%PT, PZN-8%PT and PMN-30%PT single variants, for some of which direct measurement was difficult, have been calculated from available measurements of <001> and <011> cut crystals, predicting large values for d_{15} and d_{16} in <111> orientation cuts. Energy based criteria were used in the model to simulate polarization reorientation and phase change. Experimental verification of these predictions is still needed. Additional experimental work is needed to extend the model for the calculation of the anisotropic elastic and dielectric properties.

CHAPTER 4

<110>-ORIENTED PMN-32%PT SINGLE CRYSTALS UNDER STRESS, ELECTRIC FIELD AND TEMPERATURE LOADING

In this study relaxor PMN-32%PT single crystals were subjected to combined stress, electric field, and thermal loading. The electric field induced polarization and strain for a series of prestresses and the stress induced polarization and strain for a series of bias electric fields were measured. These data were used to generate three-dimensional plots of the material responses that clearly show a phase transformation. The results demonstrate that combinations of stress and electric field drive the phase transformation and that the driving force required for this transformation decreases with increasing temperature. The threshold for the phase transformation at each temperature is used to generate a stability map for the material. Material properties are calculated for the linear regions. The results have been published at *Acta Materialia* [122].

4.1 Introduction

Because of their electromechanical coupling, piezoelectric materials have been widely utilized in transducers and actuators [123,124]. Relaxor ferroelectric single crystals have superior dielectric and electromechanical properties compared to piezoelectric ceramics. These crystals are therefore very attractive for designing high

performance actuators and sensors. They have been used in advanced applications such as medical ultrasonic imaging and sonar [10,21,125,125-130].

However, the crystals may experience electrical and mechanical loads during their manufacture and use. The dielectric and piezoelectric properties of these crystals show strong composition and field dependence due to their strong crystal anisotropy, complex domain structures and unstable phase behavior. Therefore, many applications can benefit from a better understanding of the crystal performance under various electrical, mechanical and temperature loading conditions.

Single crystals of relaxor ferroelectrics exhibit excellent electromechanical performance as well as strong anisotropy. Both <001> and <110> poled $[Pb(Zn_{1/3}Nb_{2/3})O_3]_{(1-x)}$-$[PbTiO_3]_x$ (PZN-xPT, $0<x<0.1$) and $[Pb(Mn_{1/3}Nb_{2/3})O_3]_{(1-x)}$-$[PbTiO_3]_x$ (PMN-xPT, $0<x<0.35$) rhombohedral crystals offer extremely high electromechanical coupling and piezoelectric coefficients. The electromechanical properties of these crystals are directly related to their engineered domain structures: an effective 4-domain state for the <001> poled crystals and 2-domain state for the <110> poled crystals. The <001> poled crystals give a high piezoelectric coefficient d_{33}, and the 2-domain <110> poled crystals give high d_{32}. In both cases there are very good domain compatibility and low hysteresis [8,18,19,59,63,64,117].

The physical properties of these crystals depend on composition, orientation, temperature, and applied field [63,131]. They occur in the cubic (C), tetragonal (T), rhombohedral (R), monoclinic (M) or orthorhombic (O) phase. The spontaneous polarization direction for these phases and the zero load phase diagram are shown in Figure 4-1. The high temperature phase has cubic symmetry. The lower temperature

tetragonal (*P4mm* symmetry), rhombohedral (*R3m* symmetry) and orthorhombic (*mm2* symmetry) phases have spontaneous polarization in <001>, <111> and <110> directions, respectively. Other phases can occur near morphotropic boundaries in the phase diagram when stress or electric field is present. There are potentially three kinds of monoclinic phases (M_A, M_B, M_C) [28] between the rhombohedral and tetragonal phases. Evidence of the orthorhombic phase was observed between the rhombohedral and tetragonal phase when PZN-xPT [52,132] or PMN-xPT [34] was loaded with strong electric field along <110>. The stability of the phases depends on the electrical and mechanical boundary conditions.

When the composition is close to the morphotropic phase boundary (MPB), relaxor ferroelectric crystals exhibit maxima in some of their electro-mechanical properties. Investigations have shown that the MPB of the PZN-xPT and the PMN-xPT systems are actually in a multiphase state. Coexistence of R, M, O, or T phases leads to complex phase behavior [23,43,133]. Several researchers [29-31,134,135] have observed the coexistence of rhombohedral and tetragonal domains in PZN-xPT and PMN-xPT crystals at room temperature.

A recent study of the MPB phases of PMN-xPT by means of high-resolution synchrotron X-ray diffraction indicated that a third phase is present in the composition range of 31–37% PT at temperatures around and below 25 °C [23]. Recently the extent of different phases (R, M/O, T) in PZN-xPT and the dependency of their volume fractions on the PT content were observed [136]. It has been postulated that that coexistence of multiple phases and phase instability are critical to the extraordinary crystal properties.

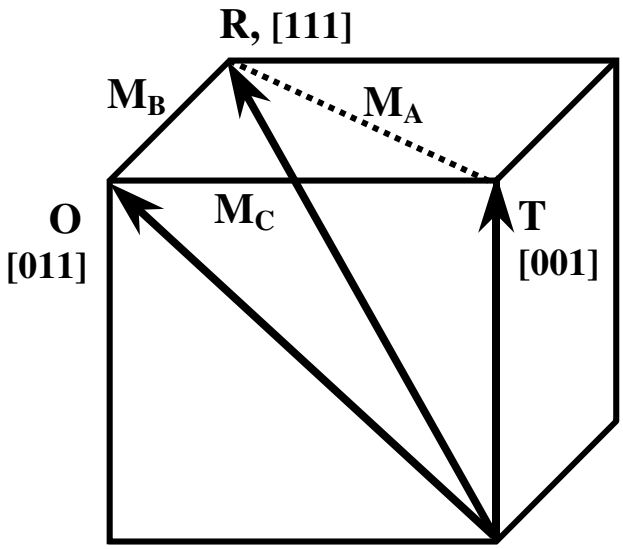

(a)

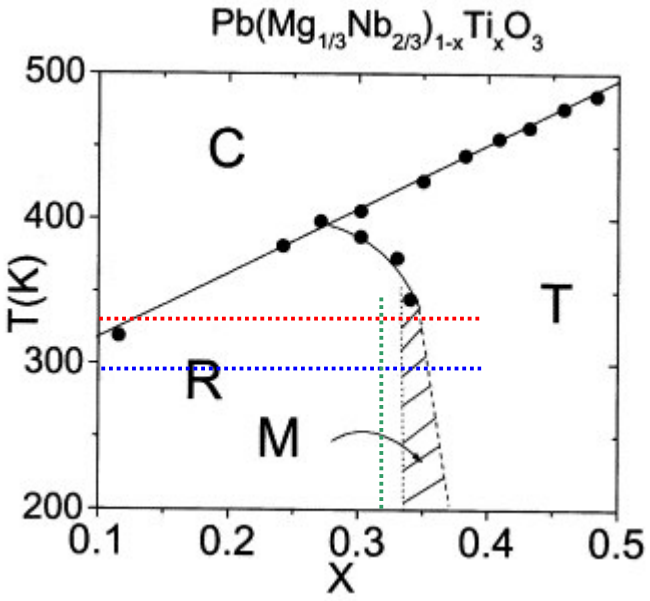

(b)

Figure 4-1. Phases in relaxor ferroelectric crystals. (a) Phases and their spontaneous polarization directions; (b) Phase diagram of PMN-PT [43]. In the temperature range of 20~60 °C, PMN-32%PT is in rhombohedral phase very close to the MPB.

Relaxor PZN-xPT and PMN-xPT crystals display both temperature and field dependent phase transformations. An electric field induced phase transition between the rhombohedral and tetragonal (R-T) phases has been observed by many authors [17,36,59,65,67,137]. An electric field induced R-O phase change has been observed in <110> PMN-0.3PT [138]. This R-O phase change is effectively a <111> to <110> "polarization rotation" as shown in Figure 4-2, with almost complete reversibility.

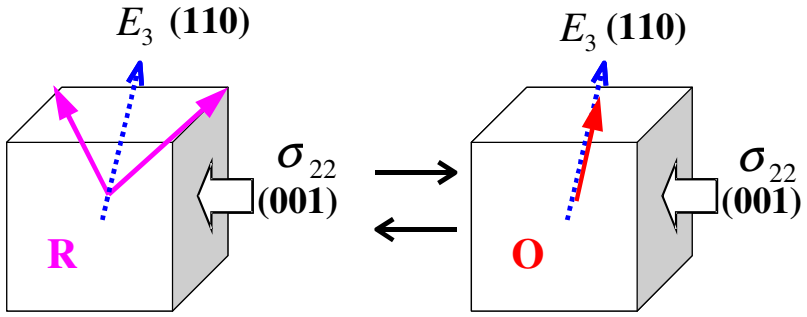

Figure 4-2. Domain structures of a <110> poled single crystal and the rhombohedral-orthorhombic phase change process under electric field and stress loading.

Stress loading also contributes to polarization switching and phase transformation [76-79,139]. Application of temperature, electric field and stress lead to complex polarization switching and phase transitions in these relaxor crystals, which change the crystal phase and domain structures and hence dramatically alter the electromechanical properties of these crystals. Phase changes during reorientation switching induce additional heterogeneity in the crystals [140]. Also, temperature and field induced phase transformations and changes of domain structure alter the properties of the crystals and can induce cracking and fatigue that can lead to premature failure in devices.

The results of experimentally mapping the phase transformations of <011> oriented PMN-32%PT induced by combinations of stress, electric field, and temperature loading are presented below. The experimental work is described in Section 4.2 and the results and data analysis are presented in Section 4.3. Section 4.4 provides concluding remarks.

4.2 Experimental Approach

4.2.1 Test Preparation

TRS Technologies manufactured and prepared the PMN-32%PT specimens used in this study. They were cut from a single boule that was grown, oriented and sliced to the required dimensions. The specimens were then diced with a wire saw to the final dimensions of approximately 4 x 4 x 12 mm and subsequently sent out for Cr/Au electrode sputtering. They were cleaned in alcohol in an ultrasonic bath for 15 minutes and stored in a 35 °C environmental chamber overnight prior to testing. The specimens were oriented as shown in Figures 4-2 and 4-3. The directions of the applied loads are also shown. Figure 4-3 shows the 4 x 12 mm faces (<110> direction) that were sputtered for electrodes and where the leads were attached. Electric field applied along the poling direction <110>, or x_3, leads to large displacement along <001>, or x_2, hence the term "32-mode".

Measurements were performed by a technician using the Stress Dependent Electromechanical Characterization System (SDECS) located at NUWC Division Newport under the supervision of Elizabeth A. McLaughlin. This experimental measurement system provides controlled electrical, mechanical, and thermal loads to

electroactive material specimens. The loading ranges are those commonly experienced in sonar transducers. The system was originally designed to determine the material properties of active materials for sonar projector designers (short-circuit compliance coefficient, constant-stress dielectric coefficient, dielectric loss, piezoelectric coefficient, coupling factor and energy density) under Navy relevant conditions and to provide feedback to crystal manufacturers on the applicability of their materials to sonar applications.

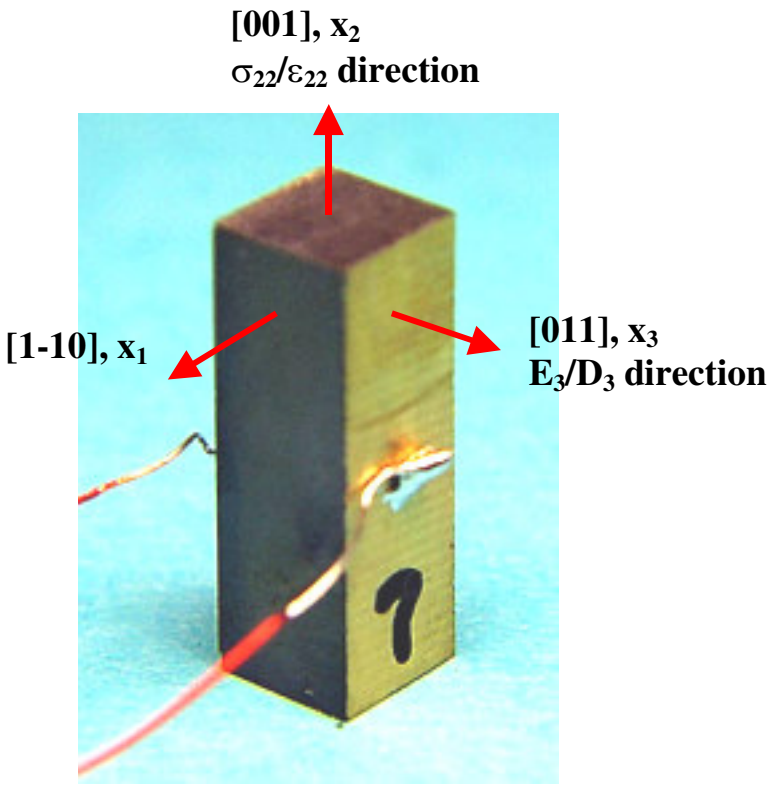

Figure 4-3. 32-mode specimen orientation and direction of applied electric field (E_3) and stress (σ_{22}), measured dielectric displacement (D_3) and strain (ε_{22}).

SDECS measures the electric field and stress induced polarization and strain behavior for a series of prestress and electric bias fields, respectively, over a range of temperatures. The electric field was applied to the specimen using a high voltage power amplifier and the voltage was recorded using a high voltage probe. The polarization (or electric displacement) was measured using modified Sawyer-Tower circuitry. The strain was recorded using foil strain gages connected to a Wheatstone bridge. A pneumatic cylinder was used to apply mechanical stress by applying a soft-spring load to the load train contained in an alignment fixture. The load was monitored using a load cell. The specimen was submerged in Fluorinert for electrical isolation. Once the specimen was placed in the fixture, a minimum -2 MPa preload was maintained throughout the test to maintain electrical contact. The pneumatic cylinder and fixture were in an environmental chamber that controlled the temperature.

4.2.2 Test Procedure

The electric field (E_3) was introduced via the electrodes on the 12 x 4 mm faces in the poling direction (x_3) and the mechanical load (σ_{22}) was applied across the 12 mm dimension. Strain gages were placed in the center of the 4 x 12 mm faces that were not electrodes. Strain (ε_{22}) was measured along the 12 mm longitudinal dimension, i.e. along x_2. The test setup provided controlled stress boundary conditions for the measurement, so that the specimen was not clamped but was free to move longitudinally at constant mechanical load when an electric field was applied. The specimens had a 3-to-1 aspect ratio such that stress components generated by the end constraints were small at the center where the strain gages were located. The electric field, polarization, strain and load

data were low-pass filtered (1000 Hz) and fed into a four-channel dynamic signal analyzer. The entire measurement was automated including temperature, load, and electric field control as well as data acquisition.

Table 4-1 lists the test matrix. The loading sequence was repeated at each temperature, starting with the highest temperature and stepping down to the lowest. The loading sequence is shown schematically in Figure 4-4. A set of stress-induced strain and polarization curves was measured for a series of electric bias fields. The input stress cycle consisted of one half of a 0.07 Hz sine wave from a load of -2 MPa to -28 MPa and back. The first stress-strain curve was measured with zero electric bias. Next, the highest electric bias field was applied to the specimen and the second stress cycle was run. Data was taken during each succeeding stress cycle for each decreasing value of field. Finally, the zero bias field measurement was repeated. Each measurement consisted of three averages. Prior to the three averages, two stress cycles with corresponding biases were run to optimize the voltage range settings for the dynamic signal analyzer.

Table 4-1. Test conditions for the <110>-cut specimen

Test mode	Electric field (MV/m peak)	Compressive load (ksi)	(MPa)	Temperature (°C)
Stress-induced, ½ sine	0, 1, 0.75, 0.5, 0.25, 0, bias	$0.3 \rightarrow 4 \rightarrow 0.3$	$2 \rightarrow 28 \rightarrow 2$	60, 40, 20
Electric field induced, 8 cycles	$0 \rightarrow 1 \rightarrow 0$	0.3, 1, 2, 3, 4, prestress	2, 7, 14, 21, 28, prestress	60, 40, 20

After the stress cycles were completed, electric field induced strain and polarization data were generated. Prior to the data measurement, two electric field signals with

corresponding loads on the specimen were run to optimize the voltage range settings for the measurement system. The first measurement was run under -2 MPa of load and the subsequent measurements under increasing loads. The electric field signal consisted of eight cycles of a 10 Hz sine wave. The sine wave was a biased 0.5 MV/m amplitude waveform that varied from zero to 1 MV/m peak. Each measurement consisted of three averages with the bridge powered and then three with the bridge un-powered. The strain signal recorded with the bridge powered consisted of a combination of specimen strain and apparent strain induced in the strain gage from the proximity of the AC electric field. The undesired apparent strain was measured separately by removing the power to the bridge and re-running the same test. The apparent strain was subtracted from the total strain signal to reveal the specimen strain. The specimen was inspected upon completion of the test with no cracks being apparent under a 7x microscope.

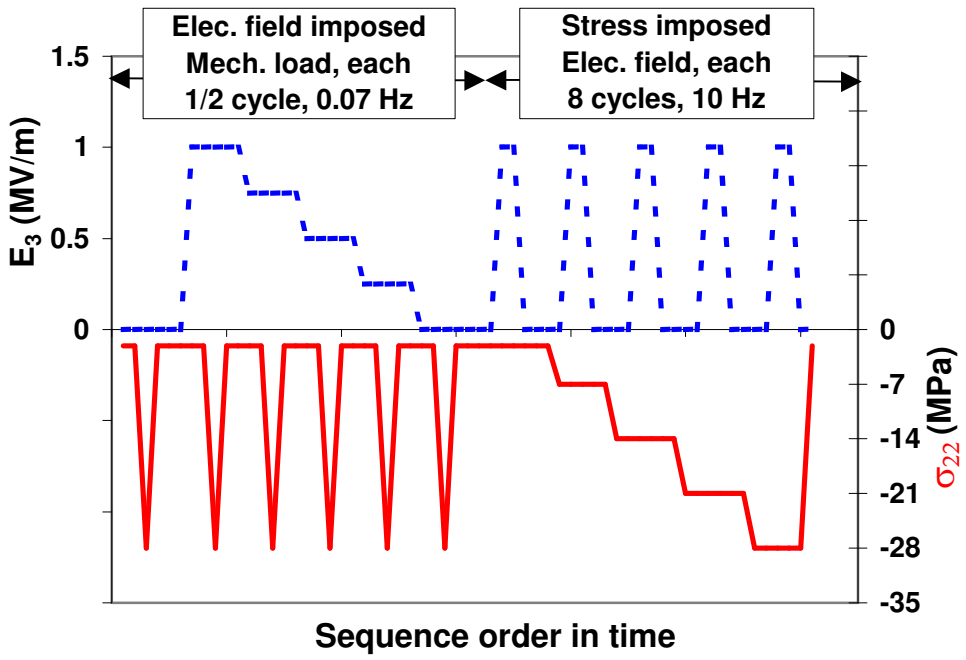

Figure 4-4. Combined electric field and stress loading scheme (test sequence).

4.3 Results and Discussion

4.3.1 Initial Data Analysis

Once the voltage data was recorded it was processed using a MATLAB data analysis routine that applied the calibrations of the various instruments used and factored in the specimen dimensions. The routine also corrected the field-induced polarization data for drift by leveling the peaks of the eight cycles. The central three cycles were output into text files for further analysis. Two types of data were recorded: 1) field-induced strain and polarization data for different pre-stresses and temperatures, and 2) stress-induced strain and polarization for different electric biases and temperatures.

Drift of electric displacement data resulted in a loss of the reference value for polarization. To recover the electric displacement offset, the measured data from both electric field and stress cycling were correlated at common loading points. First the remnant electric displacement for the <110> poled PMN-32%PT is about 0.3 C/m^2 [141]. This was set as the initial value for -2 MPa prestress AC electric field loading data. Then the starting points for stress loading data were adjusted based on the results for -2 MPa prestress AC electric field loading data. Now the starting points for AC field loading with -7 MPa or higher prestress were adjusted according to 0 V bias stress loading data. The electric displacement data from stress loading shows signs of drift that were induced by the instrumentation. These data sets were adjusted to meet those from AC electric field loading, which seems to be more accurate.

4.3.2 Strain and Electric Displacement Responses

Figure 4-5 shows two-dimensional plots of the room temperature data. Strain in the x_2 direction (ε_{22}) vs. electric field in the x_3 direction (E_3), electric displacement in the x_3 direction (D_3) vs. E_3 for different pre-stresses and stress in the x_2 direction (σ_{22}) vs. ε_{22} as well as σ_{22} vs. D_3 for different electric biases are plotted. Figure 4-5a shows the strain as a function of electric field. Superimposed are vertical line plots of the stress induced strain response at fixed electric bias fields. Markers on these lines are for the data points of -2, -7, -14, -21, and -28 MPa. They match the electric fielding loading curves very well, showing that the data from independent measurements is internally consistent. Note the onset of non-linearity marked by the dashed lines and the suspected phases shown schematically. Figure 4-5b shows the electric displacement plotted as a function of electric field. In this case the vertical lines are produced by the electric displacement change when stress is applied at fixed electric fields. This plot makes clear the adjustment made to the electric displacement offset. Arrows in Figure 4-5a,b indicate the direction for increasing prestress. Figure 4-5c shows the stress vs. strain curves. In this case the horizontal lines are the result of the strain variation with field at constant stress. Figure 4-5d shows the stress vs. electric displacement curves. In this case, the horizontal lines are the result of electric displacement changes induced by electric field at constant stress. The electric displacement drifts during stress loading. Similar instrumentation error exists at other temperatures. Arrows in Figure 4-5c,d indicate the direction for increasing electric bias.

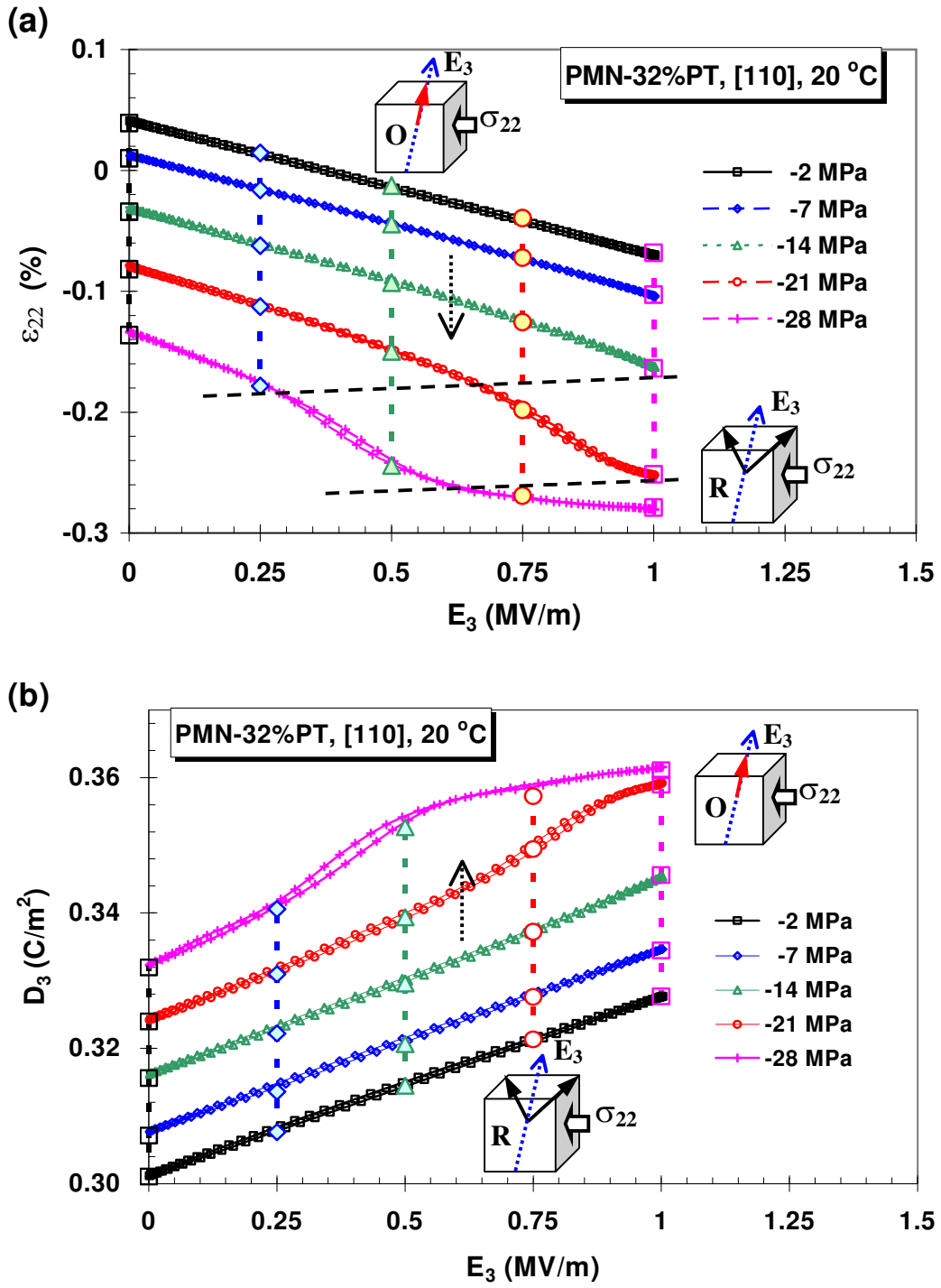

Figure 4-5. Two-dimensional plots of the room temperature data. (a) Strain vs. electric field for different prestresses, vertical lines are σ_{22}-ε_{22} at fixed E_3; (b) Electric displacement vs. electric field for different prestresses, vertical lines are D_3-σ_{22} at fixed E_3; (c) Stress vs. strain for different bias electric field, horizontal lines are ε_{22}-E_3 at fixed σ_{22}; (d) Stress vs. electric displacement for different bias electric field, horizontal lines are D_3-E_3 at fixed σ_{22}.

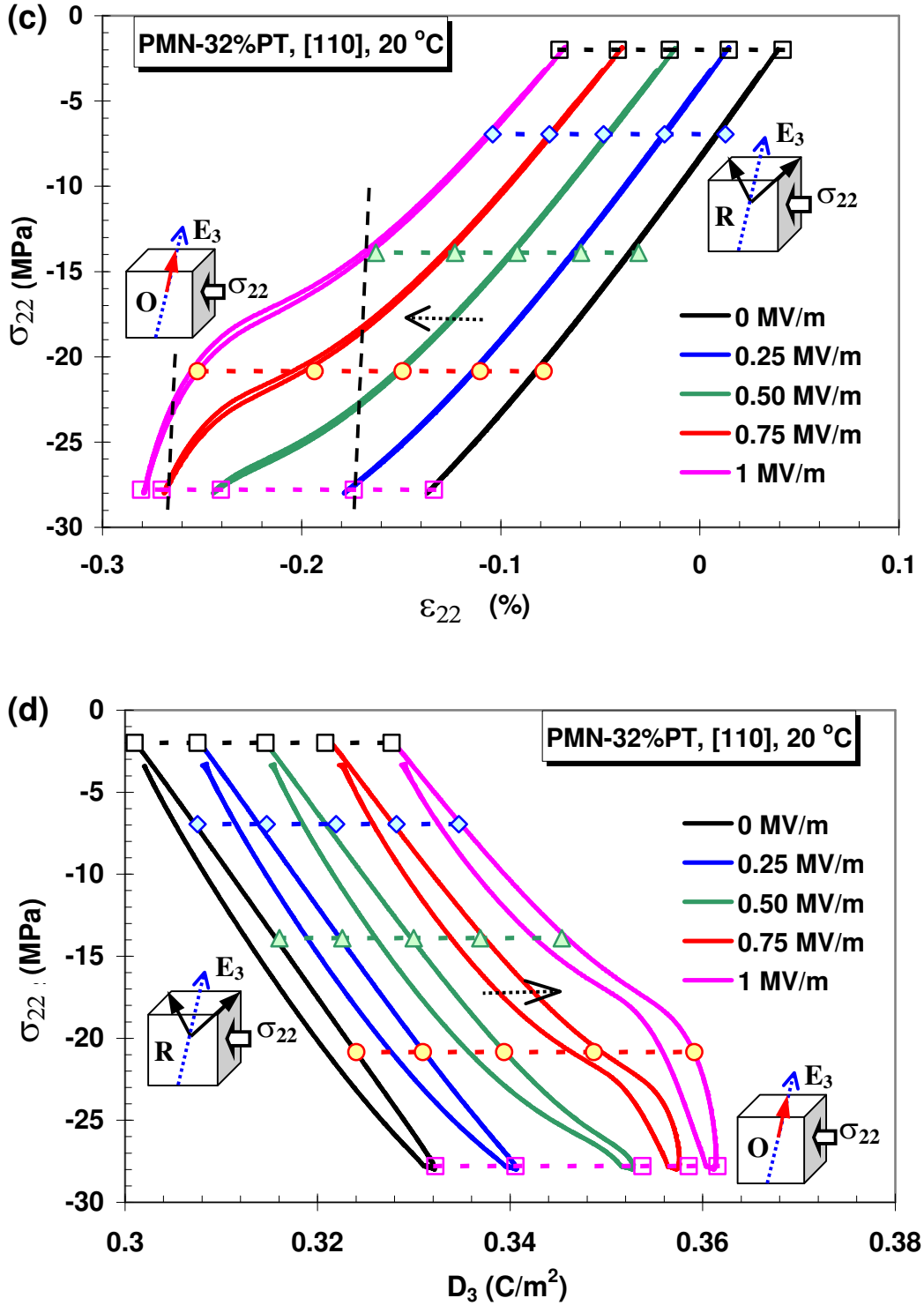

Figure 4-5 (continued).

The two-dimensional plots do not adequately show the coupled thermo-electro-mechanical dependence of the material behavior. To better illustrate this dependence, three-dimensional plots of the strain and electric displacement versus the applied field and stress are shown in Figures 4-6 and 4-7 for each of the three temperatures. When reading these plots it is important to note the subscripts on the quantities shown on the axis labels. The applied stress and the electric field directions are perpendicular to one another. Figure 4-6.a shows the room temperature stress, strain, and electric field data. Note the upper planar region and the lower planar region with a non-linear regime between. The upper planar region has a steeper slope than the lower planar region. This is associated with a larger piezoelectric coefficient and a higher compliance. The lower region has a lower piezoelectric coefficient and lower compliance. We believe these two regimes are associated with two different phases and the non-linear regime is the phase transition as shown schematically in Figures 4-2 and in Figure 4-5. Published phase diagrams identify the initial phase as rhombohedral. The direction of the applied electric field suggests that the secondary phase is orthorhombic, but this remains to be confirmed. Figure 4-6b shows the same plot at 40 °C. Note the change in slope corresponding to temperature dependent compliance and piezoelectric coefficients. Note also the reduced fields associated with the onset of the phase transformation. This trend continues as temperature is further increased as seen in Figure 4-6c. Figure 4-7 shows the same type of plots, but for the stress, electric field, and electric displacement. The open loops seen in the electric displacement stress data are likely an artifact of the instrumentation.

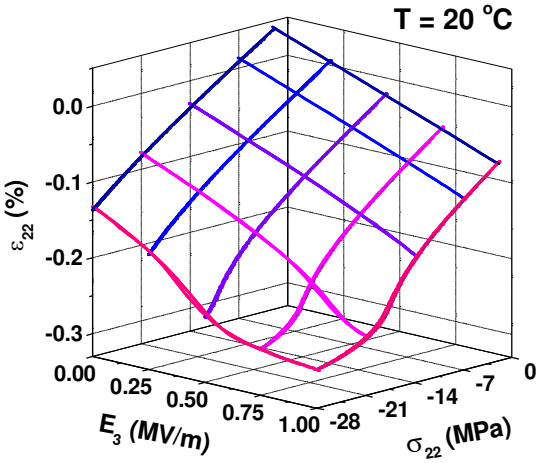

(a)

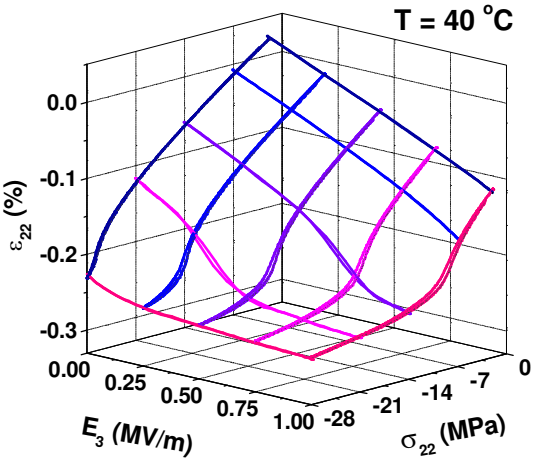

(b)

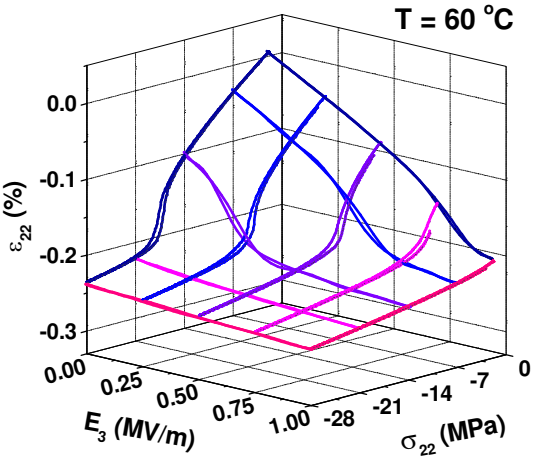

(c)

Figure 4-6. Three-dimensional plots of strain (ε_{22}) under combined electric field (E_3) and stress (σ_{22}) loading. (a) 20 °C, (b) 40 °C, and (c) 60 °C.

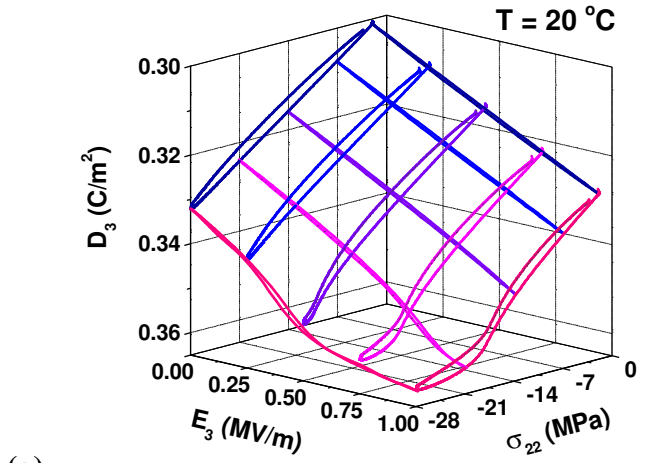

(a)

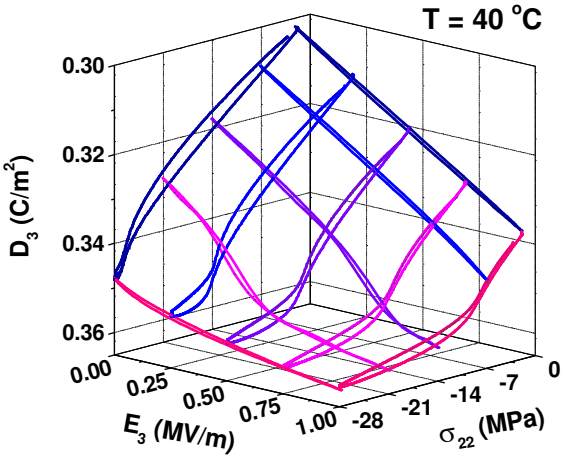

(b)

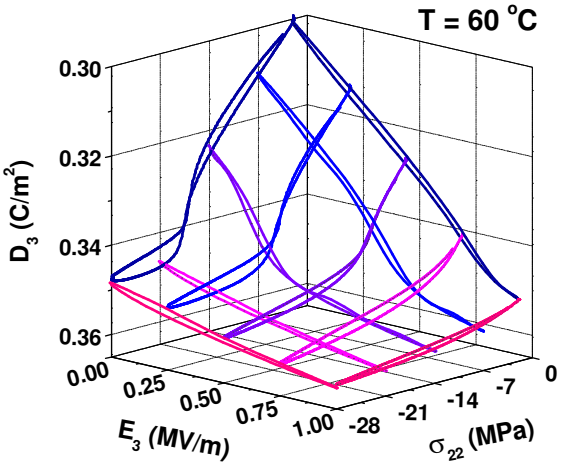

(c)

Figure 4-7. Three-dimensional plots of electric displacement (D_3) under combined electric field (E_3) and stress (σ_{22}) loading. (a) 20 °C, (b) 40 °C, and (c) 60 °C.

4.3.3 Field Induced Phase Transition

To date there has been little in situ diffraction work done to properly identify field induced phase transformations in PMN-xPT single crystals, so the following discussion of phases is based on symmetry and loading directions. From Figure 4-6 and Figure 4-7 it is apparent that both the <110> electric field and the <001> compressive stress tend to decrease the <001> strain and increase the <110> electric displacement. Before electric field and stress loading, the PMN-32%PT crystal is in the rhombohedral (R) phase very close to the MPB in the temperature range of these tests. The R crystal is polarized into a 2-domain state by the <110> E_3 field. This poled 32-mode R crystal displays linear piezoelectric and dielectric response. As the electric field is increased, a phase change occurs, shrinking the crystal in the <001> direction. In addition to a decrease of strain ε_{22} and increase of the electric displacement D_3, this phase change leads to a dramatic drop in magnitude of the piezoelectric coefficient d_{32}, the dielectric coefficient K_{33}^{σ}, and the elastic coefficient s_{22}^{E}. The new phase is probably the orthorhombic (O) phase poled in a single domain, or the M_B/M_C phase, in which a two-domain poled state is formed. The electromechanical response of the new phase is also linear. The lack of hysteresis associated with the phase transformation suggests that it is almost reversible. This gives credence to great compatibility of domains and a rotation through intermediate monoclinic phases during the transformation process.

The compressive stress in the <001> direction, which is perpendicular to the poling (<011>) direction, does not induce depolarization of the <110> poled R crystal. No depolarization is observed in stress loading even at zero E_3 bias field. Instead, it acts together with the E_3 field, forcing the crystal to undergo a phase change without

depolarizing the crystal. Therefore if a stress is present in the poling direction that could cause depolarization, a compressive stress in the <001> direction will help stabilize the poling state. But if this stabilizing stress is high enough, it may induce the R-O phase change at a relatively low or zero electric field.

From the surface plots it is clear how the strain ε_{22} and electric displacement D_3 change during the application of the combined electric field and stress loading. The <011> engineered domain state is driven to a state with lower strain in the <001> direction by the compressive <001> stress and the <011> electric field, thus the stress and the electric field are cooperative driving forces for the phase transformation. It is also apparent that as the temperature increases, the phase change occurs at lower stress and electric field levels. Increase of temperature reduces the driving forces needed for the phase change to occur. The barrier to phase transformations is inversely proportional to temperature over the range characterized, which will be discussed in next section.

Some of the elastic, piezoelectric, dielectric and electromechanical coupling coefficients of the crystal at different temperatures were calculated and listed in Table 4-2. The R phase exists at low field level and the O phase at high field level. For this reason the coefficients for the R phase are slopes measured at small electric field and small stress loading, while those for the O phase are from high electric field and high stress loading. The R phase shows a strong temperature dependence of the elastic, piezoelectric and dielectric coefficients. The measured coefficients for the O phase at 40 °C and 60 °C (at high electric field and high stress) are close to each other, while those at 20 °C are higher. This is possibly due to an incomplete phase change, i.e. multiphase coexistence.

Table 4-2. Measured properties of the <110>-cut PMN-32%PT crystal

Material properties	T(°C)	Rhombohedral	Orthorhombic
Compliance s_{22}^{E} (10^{-12} m^2/N)	20	60	24.9
	40	66	15.9
	60	79	15.4
Piezoelectric d_{32} (pC/N)	20	-1110	-300
	40	-1350	-170
	60	-1690	-170
Dielectric $K_{33}^{\sigma}(\varepsilon_0)$ (ε_0= 8.855*10^{-12} F/m)	20	2980	1231
	40	3820	960
	60	5340	970
Coupling factor k_{32}	20	0.88	0.58
	40	0.90	0.46
	60	0.87	0.47

4.3.4 Phase Change Map

As mentioned above, the applied stress, electric field and temperature cooperatively contribute to the phase change. Increasing the electric field E_3, compressive stress σ_{22} and temperature T all help induce the phase change. Values of E_3, σ_{22}, and T at the start and finish of the phase transition are obtained by picking the data points where the slopes of the curves start to change quickly. These points are plotted in the electric field-stress-temperature coordinates at two different viewing directions, as shown in Figure 4-8a, b. Electric field E_3 is in <110> direction, and stress σ_{22} is in <001> direction.

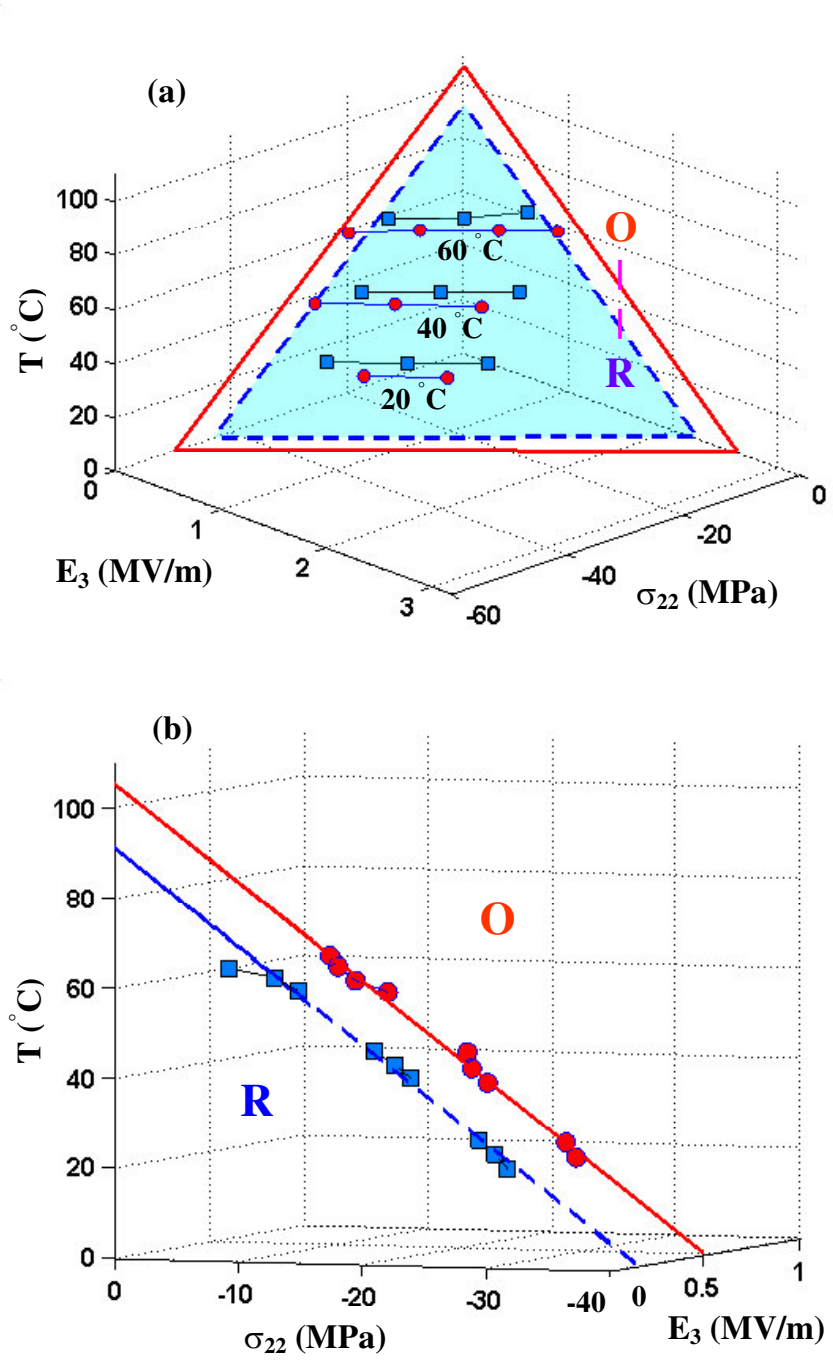

Figure 4-8. R-O Phase change plane plotted in electric field-stress-temperature coordinate system. (a) The linear relation of electric field and stress at constant temperature; (b) The phase transition points drop well into these two planes.

In Figure 4-8a the bottom (small) triangle refers to the onset plane of the transition, and the top (big) triangle is in the plane for the end of the transition. Load combinations below the bottom plane do not induce the phase transition. It is found that the starting points (E_3, σ_{22}, T) for the phase change drop into one plane and the finishing points into another. The phase change occurs between these two planes. Below the start plane the crystal maintains its high performance in the R phase; above the finish plane the crystal is in O phase and its properties are diminished.

Based on observations, the stress, electric field and temperature that drive the forward and reverse phase changes can be characterized by two planes in the E_3-σ_{22}-T space. By least square fitting of the data, the equation for the start plane is T = 91.1 - 41.3E_3 + 2.12σ_{22} and the equation for the finish plane is T = 105. - 40.6E_3 + 2.12σ_{22}. These two planes are nearly parallel (shown in Figure 4-8b), giving an estimate of the R-O phase change temperature range (at zero Electric field and stress) T_c = 90~105 °C.

Increases of <110> electric field and <001> compressive stress increase the energetic driving force that induces the rhombohedral to orthorhombic phase change. When this driving force reaches a critical level (energy barrier), the phase change will proceed. Increases of temperature reduce this energy barrier for the phase transformation. A work-energy analysis of this phase transition process will be given in next chapter. To avoid the R-O phase change in applications, the allowable electric field (E_3), stress (σ_{22}) and temperature (T) combinations should be maintained under this plane (within the tetrahedron confined by the plane and the E_3-σ_{22}-T coordinate planes).

4.4 Concluding Remarks

The strain and polarization of the <011> PMN-32%PT crystal under combined electric field and stress loading at different temperatures were recorded. Evidence of an R-O phase change of the crystal under stress and/or electric field loading has been observed. Phase transformation fields were measured, and the phase change criterion was given in form of linear equations of applied electric field, stress and temperature. The applied stress, electric field and temperature cooperatively contribute to the phase change.

These results are important to actuator and sonar transducer design and performance. Stress bias is needed to prevent the brittle crystals from cracking and electric field bias is needed to prevent reversing the polarization of the crystals. The bias levels selected should place the operating point at the center of the upper planar region of the three-dimensional plots with the varying fields causing the excursions to span the linear range. Increased temperature reduces the allowable bias range and reduces the allowable field excursions. It is noted that this data is for a single composition near the morphotropic boundary and a particular crystal cut. Compositions farther from the MPB are anticipated to require larger driving forces at these temperatures to induce a phase transition. Additional work is needed on other compositions and on the <001> cut crystals.

Acknowledgement

The author would like to thank Elizabeth A. McLaughlin at Naval Undersea Warfare Center (NUWC) Division Newport for providing the experimental data in this chapter.

CHAPTER 5

ENERGY ANALYSIS OF FIELD INDUCED PHASE TRANSITIONS IN RELAXOR FERROELECTRIC CRYSTALS

Relaxor ferroelectric single crystals exhibit several extraordinary properties including ultrahigh dielectric permittivity, piezoelectric coefficients, and electromechanical coupling factors [8]. In addition the proximity of their composition to phase instabilities results in temperature, stress and electric field induced phase transformations. A thermodynamics based analysis of the measured material behavior in <110> orientated (PMN-32%PT) and (PZN-4.5%PT) crystals under combined stress, electric field and temperature loading conditions leads to a direct measurement of the relative phase energy levels. The approach demonstrates that a small number of experiments are sufficient to characterize the multi-field driven phase transformations.

5.1 Introduction

Rhombohedral phase of relaxor single crystals $[Pb(Zn_{1/3}Nb_{2/3})O_3]_{(1-x)}$-$[PbTiO_3]_x$ (PZN-xPT, $0<x<0.1$) and $[Pb(Mn_{1/3}Nb_{2/3})O_3]_{(1-x)}$-$[PbTiO_3]_x$ (PMN-xPT, $0<x<0.35$) exhibit extraordinary electromechanical properties that are dependent on their microscopic domain and phase structures. When the crystals are poled along the <001> or <110> direction, there are maxima in certain piezoelectric coefficients and minima in dielectric losses. This is associated with an "engineered domain state" formed within the

crystals. When Poled in these orientations, the domain walls do not move in response to applied positive fields, resulting in linear non-hysteretic material response. The material properties are dependent on composition. Recent research has focused on mapping the temperature and electric field induced phase transitions, resulting in data showing temperature and field dependent material properties [142], composition-temperature phase diagrams [43], electric field-temperature phase diagrams [65] and the coexistence of multiple phases [134,136]. Limited results have been reported concerning the effect of stress on these transformations [76,78,139]. These materials display temperature and field induced phase transformations [52,131].

The work presented below shows that an energy based approach is particularly important for multi-physics coupled materials such as ferroelectrics, ferromagnetics [143] and ferroelectromagnets [144] because it provides a scalar transformation criterion that is easily measured. Phenomenological Landau-Devonshire theory is widely used to explain observed phases and phase transition phenomena [84,145]. Theoretical investigations have also been carried out to study structure-property relations at the atomic level [146,147]. Fu and Cohen [66] have studied a polarization rotation mechanism of piezoelectric single crystals under electric field using first principles calculations. The relative energy levels of the phase (presented below) will provide data for comparison with ab initio calculations and input for phenomenological models.

5.2 Phase Transformations in the <110> Poled Crystals

Evidence of an electric field induced rhombohedral to orthorhombic phase change has been observed in <110> oriented PMN-30%PT [138,148] and in PZN-4.5%PT [52].

The rhombohedral (R) phase has a spontaneous polarization in <111> direction and the orthorhombic (O) phase has a spontaneous polarization in <110> direction. Crystal variants present in a <110> poled single crystal and the rhombohedral-orthorhombic (R-O) phase transition under electric field E_3 and stress σ_{22} were illustrated in Figure 4-2. This phase change is effectively a <111> to <110> polarization rotation. Both the positive <110> electric field and the <001> compressive stress drive the R-O phase transition and stabilize the O phase. Figure 5-1 shows the typical electric displacement versus electric field curves for both PZN-4.5%PT [52] and PMN-32%PT [122] crystals with an R-O phase change. In this figure the PZN-4.5%PT was at 20 °C and zero stress, and the PMN-32%PT was at 40 °C and -14 MPa stress in the <001> direction. The two curves demonstrate the different phase change behavior of these two crystal types. A jump-type phase change with energy loss occurs in the PZN-4.5%PT, while the transformation in the PMN-32%PT is almost reversible with little hysteresis.

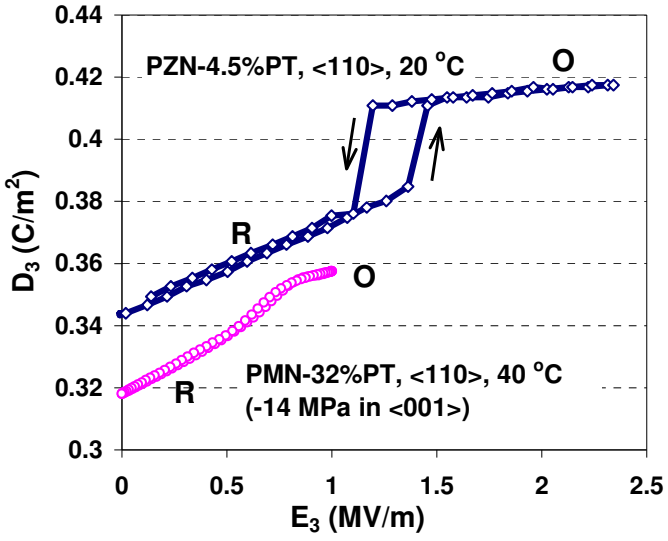

Figure 5-1. Field induced R-O phase transitions in <110> oriented relaxor PZN-PT and PMN-PT single crystals [52,122].

5.3 Work-Energy Relation

The electromechanical coupling behavior of piezoelectric materials is described by piezoelectric constitutive equations:

$$\varepsilon_{ij} - \varepsilon_{ij}^{r} = s_{ijkl}^{E}\sigma_{kl} + d_{nij}E_{n} \tag{5-1a}$$

$$D_{m} - D_{m}^{r} = d_{mkl}\sigma_{kl} + K_{mn}^{\sigma}E_{n} \tag{5-1b}$$

where σ_{kl} and E_{n} are applied stress and electric field, ε_{ij} and D_{m} are the strain and the electric displacement, ε_{ij}^{r} and D_{m}^{r} are the remnant strain and remnant electric displacement, and s_{ijkl}^{E}, d_{mkl} and K_{mn}^{σ} are the elastic (constant electric field), piezoelectric, and dielectric (constant stress) coefficients, respectively. Several phenomena including domain wall motion, phase transitions, and temperature dependence induce non-linearity and hysteresis in s_{ijkl}^{E}, d_{mkl} and K_{mn}^{σ}.

Calculation of the work done in a closed thermodynamic cycle leads to a direct measurement of the phase energy. Figure 5-1 provides data for the calculation of mechanical and electrical work during the phase transformation. Consider the poled crystal at zero stress and electric field with the initial temperature used as the reference state. According to the first law of thermodynamics, a change of internal energy density of the crystal during stress and electric field loading is given by

$$\Delta u = \Delta q + \Delta w \tag{5-2}$$

where Δq is the heat received from heat transfer or generation, and Δw is the work done by external forces (electrical and mechanical).

The work done per unit volume by a compressive stress in the <001> (x_2) direction and an electric field in <110> (x_3) direction can be computed by integration along the loading path:

$$w = \int \sigma_{22} d\varepsilon_{22} + \int E_3 dD_3 \tag{5-3}$$

In a linear region under the prescribed loads σ_{22}, E_3 (either in the R phase or O phase), the constitutive equations 5-1a, b reduce to:

$$\varepsilon_{22} - \varepsilon_{22}^r = s_{2222}^E \sigma_{22} + d_{322} E_3 \tag{5-4a}$$

$$D_3 - D_3^r = d_{322} \sigma_{22} + K_{33}^\sigma E_3 \tag{5-4b}$$

Experimental data gives direct measurements of the s_{2222}^E, d_{322} and K_{33}^σ coefficients for both the R phase and the O phase (in the linear regions) [122]. With these coefficients, the quadratic coupled energy function for the single crystal R phase or O phase is given by

$$w^l = \frac{1}{2} s_{2222}^E \sigma_{22}^2 + d_{322} \sigma_{22} E_3 + \frac{1}{2} K_{33}^\sigma E_3^2 \tag{5-5}$$

This result is independent of loading paths for linear material behavior.

The Gibbs free energy is a function of temperature, stress and electric field. In the common experimental condition for static measurements with temperature as the independent variable, stress and electric field are fixed (usually zero). Phase equilibrium is achieved when the Gibbs free energy *g* is at a minimum. This thermodynamic principle also applies to stress and electric field driven structural phase transitions. The presence of

stress or electric field alters the Gibbs free energy and induces the R-O phase change. In the case discussed above, the change of Gibbs free energy at constant temperature is:

$$\Delta g = -\int \varepsilon_{22} d\sigma_{22} - \int D_3 dE_3 \tag{5-6}$$

The change of Gibbs free energy for linear behavior of a single phase at constant temperature is given by

$$\Delta g = -(\frac{1}{2} s^{E}_{2222} \sigma^2_{22} + d_{322} \sigma_{22} E_3 + \frac{1}{2} K^{\sigma}_{33} E^2_3 + \varepsilon^{r}_{22} \sigma_{22} + D^{r}_3 E_3) \tag{5-7}$$

The remnant terms can be lumped with the reference state for the Gibbs free energy. From this reference point, the Gibbs free energy for a linear R phase is the negative value of w^l from Equation 5-5.

5.4 Data Analysis

A work-energy analysis of the PZN-4.5%PT crystal under electric field loading is shown in Figure 5-2. By applying the integrals in Equation 5-3 to the data shown in Figure 5-1, the external work done on the PZN-4.5%PT crystal was computed and plotted in Figure 5-2a. The changes of internal energy from Equation 5-5 and Gibbs free energy from Equation 5-7 for a linear R phase are plotted for comparison with the actual external work. After a loading cycle, the computed work does not return to zero, but has an offset Δq. This offset reflects the irreversible work done during the cycle, which has been converted to heat and dissipated to the isothermal bath.

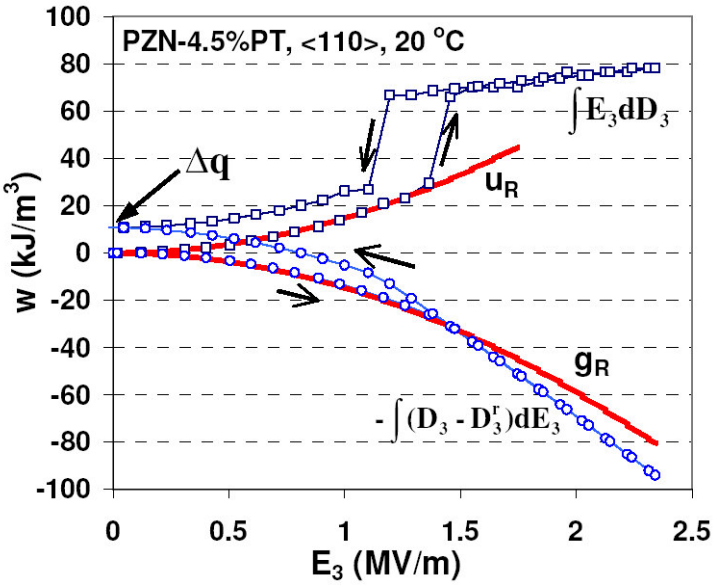

(a)

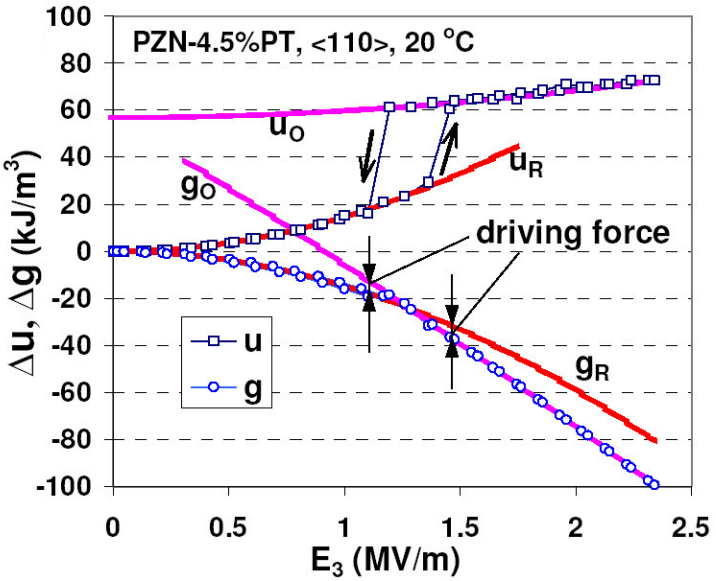

(b)

Figure 5-2. Work-energy analysis of PZN-PT crystals under external field loading. Internal energy and Gibbs free energy values for the R phase and O phase based on linear electromechanical response are super-imposed. (a) Work done by the electric field on the PZN-4.5%PT crystal; (b) Change of internal energy and Gibbs free energy for the PZN-4.5%PT crystal.

The heat generated in the PZN-4.5%PT crystal is due to the phase change hysteresis. If the computed work is adjusted by subtracting $\Delta q/2$ after the R-O phase change and a second $\Delta q/2$ after the reverse phase change, its value returns to zero after unloading, as shown in Figure 5-2b. After this adjustment for dissipated energy, the resulting plot represents the change of the internal energy density of the crystal during the cycle. Changes of internal energy from Equation 5-5 and Gibbs free energy from Equation 5-7 are plotted for the R phase and O phase with a shift for the O phase so that it matches at the maximum loading. The difference between g_O and g_R is the driving force for the transformation.

For the PMN-32%PT crystal, the results show that the heat generated during the cycle (the first term in Equation 5-2) is negligible; therefore the increase of internal energy density is equal to the work done by the applied stress and the electric field. The results are shown in Figure 5-3. The initial offset is due to the stress preloading in the <001> direction.

In the experimental investigation of relaxor PMN-32%PT single crystals [122], electric field induced polarization and strain for a series of bias stresses and stress induced polarization and strain for a series of bias electric fields were measured at three different temperatures (20, 40, 60 °C). These surfaces are functions of temperature. A work-energy analysis for the 40 °C data is shown in Figure 5-4. Figures 5-4a and 5-4b are the strain and electric displacement responses of PMN-32%PT single crystals under combined stress and electric field at 40 °C (refer to Figure 4-6b, 4-7b). As discussed in last chapter, there are two distinct planar regions (depicted by broken lines) in these three-dimensional surfaces. They are the rhombohedral (R) region at low field level and

the orthorhombic (O) region at high field level. Between them is an R-O phase transition region showing sharp changes of strain and electric displacement. This is associated with a large change of internal energy.

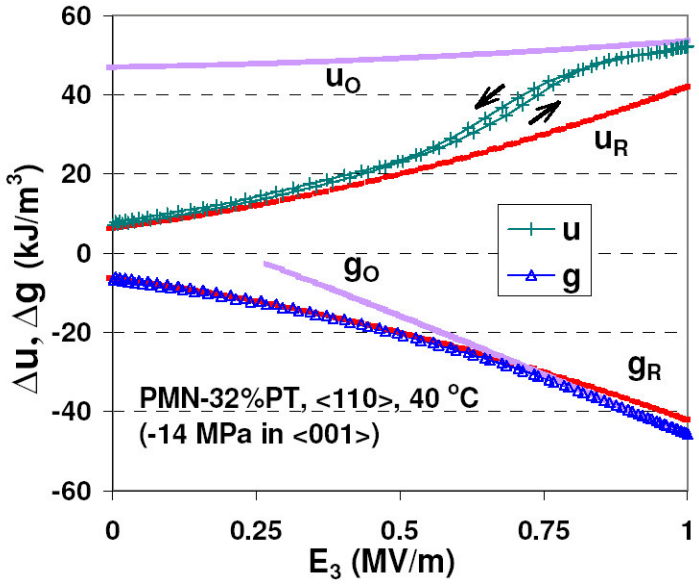

Figure 5-3. Work-energy analysis of PMN-PT crystals under external field loading. Internal energy and Gibbs free energy values for the R phase and O phase based on linear electromechanical response are super-imposed.

By applying the two integrals of Equation 5-3 simultaneously for each loading path, the total work along different loading paths was computed and the results plotted in $E_3 - \sigma_{22}$ coordinates as shown in Figure 5-4c. The quadratic energy functions for the linear R and O phases are superimposed. The figure shows how the R phase crystal undergoes the phase change into the O phase with an associated increase of internal energy due to the external loading.

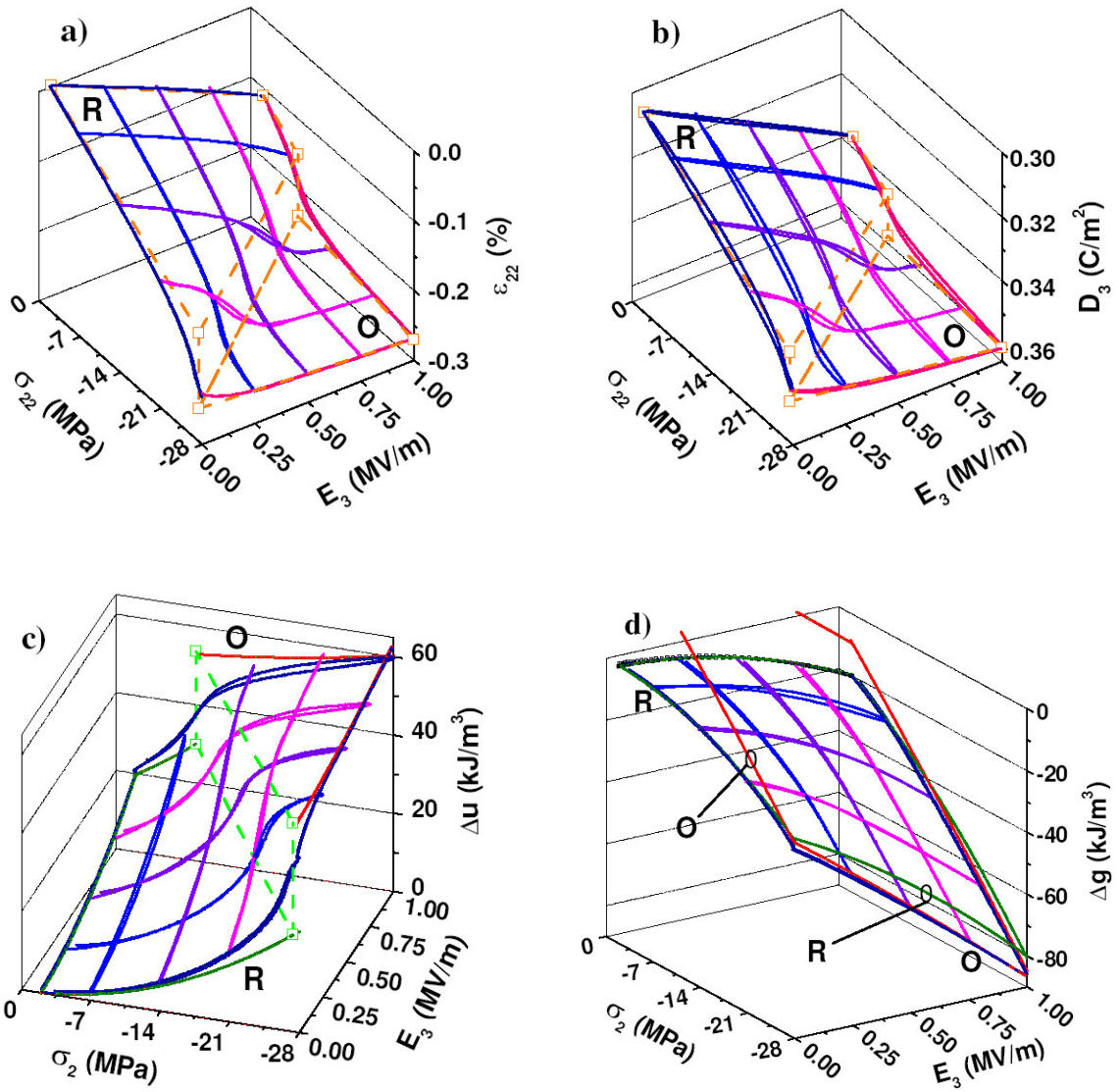

Figure 5-4. Behavior of PMN-32%PT crystals as a function of combined stress and electric field loading at 40 °C. Values for the R phase and O phase based on linear electromechanical response were plotted for comparison. (a) Strain [122]; (b) Electric displacement [122]; (c) Change of internal energy; (d) Change of Gibbs free energy.

An important condition for the phase transformation is that the external driving forces do positive work during the process. Both the compressive stress in the x_2 direction and the electric field in the x_3 direction contribute positive work during the loading processes. Note that the constant stress during electric field loading and the constant electric field during stress loading do work during the process.

A three-dimensional surface of the Gibbs free energy is plotted in $E_3 - \sigma_{22}$ coordinates in Figure 5-4d. This surface gives the minimum Gibbs free energy of the crystal as a function of applied stress and electric field at fixed temperature. The crystal is in the R phase at low stress and electric field; as the applied stress and electric field increase, the Gibbs free energy decreases and the O phase becomes stable at high field region. The observed gradual phase transition behavior with small hysteresis is the result of multi-phase coexistence with intermediate monoclinic phases [41].

The thermodynamic analysis of the data shows that when electric field and stress loading are applied at a given temperature, the R-O phase change begins when the internal energy reaches a critical value and the Gibbs free energy provides a positive driving force. It was also found that the critical energy decreases linearly with increasing temperature. The phase change finishes after a certain amount of additional external work. This analysis was repeated at several temperatures, resulting in the critical energy-temperature phase diagram shown in Figure 5-5. The two linear critical energy-temperature relations describe the onsets of the R-O phase change and the reverse O-R phase change. Between the R and O phases is the multiphase transition region.

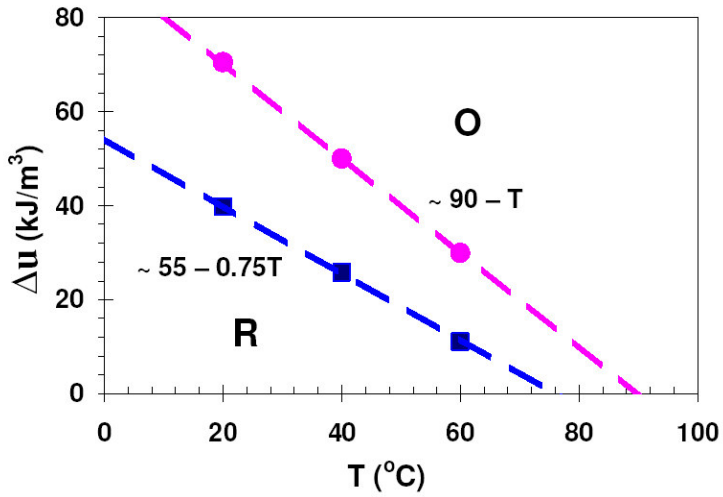

Figure 5-5. Critical energy-temperature phase diagram for <110> poled PMN-32%PT. Symbols are from measurements of electric field and stress induced phase transition at three temperatures.

5.5 Concluding Remarks

The phase transformation behavior under combined stress, electric field, and thermal loading is a coupled multivariable phenomenon. Full characterization of the phase behavior requires a large test matrix with temperature, stress, and electric field being varied. This must be repeated for a series of compositions, presenting significant challenges. This work began with an extensive set of data for a single composition and used a thermodynamics approach to show that the phase transformation behavior can be characterized with a much smaller set of experiments. At a given temperature the phase transformation begins at a critical level of internal energy density and ends at a second critical level. A second criterion, minimization of the Gibbs free energy, determines whether the transformation will take place. The critical energy levels were found to be independent of the combinations of stress and electric field that induced them. This leads

back to the analysis of the electric displacement – electric field data that was initially discussed. Collection of *D-E* data is straightforward and can be readily performed at a series of temperatures. The additional data that is needed is a measurement of the elastic, piezoelectric, and dielectric coefficients of each phase. This provides sufficient information to characterize the multivariable driven transformation. These results enable the rapid characterization of the structural phase transformation behavior over a range of compositions and temperatures.

The "engineered domain state" is critical to the utilization of this approach. In the <001> and <011> crystal cuts the domain walls are stable. This means there is little or no ferroelectric or ferroelastic polarization reorientation. In other crystal cuts there is domain wall motion under applied stress and electric fields. This gives rise to minor hysteresis loops and associated energy dissipation under applied fields. In this case it would be difficult to distinguish between energy barriers to transformation and the dissipative energy in the highly rate dependent and irreversible process of domain wall motion.

CHAPTER 6

<001>-ORIENTED PMN-32%PT SINGLE CRYSTALS UNDER STRESS, ELECTRIC FIELD AND TEMPERATURE LOADING

Phase transformations of <001> oriented PMN-32%PT single crystals induced by combinations of stress, electric field, and temperature loading were mapped experimentally. Stress, strain, electric displacement, electric field and temperature are varied and measured. The results indicate that combinations of stress and electric field applied along <001> direction drive several phase transformations, and the driving force for the transformations decreases with increasing temperature.

6.1 Introduction

Relaxor ferroelectric crystals exhibit extraordinary dielectric and electromechanical properties [122]. The dielectric and piezoelectric properties of relaxor single crystals are anisotropic, nonlinear and hysteretic. Both <001> and <110> poled $[Pb(Zn_{1/3}Nb_{2/3})O_3]_{(1-x)}$-$[PbTiO_3]_x$ (PZN-xPT, $0<x<0.1$) and $[Pb(Mn_{1/3}Nb_{2/3})O_3]_{(1-x)}$-$[PbTiO_3]_x$ (PMN-xPT, $0<x<0.35$) rhombohedral crystals offer extremely high electromechanical coupling and piezoelectric coefficients. The physical properties of these crystals are related to their domain structures and phase states, which change with composition, orientation, temperature, and applied fields [63,131].

The crystals occur in the cubic (C), tetragonal (T), rhombohedral (R), monoclinic (M), and orthorhombic (O) phases. The spontaneous polarization directions for the polar

phases were shown in Figure 4-1a. The high temperature phase (parent phase) has cubic symmetry. The lower temperature tetragonal (*4mm* class), rhombohedral (*3m* class) and orthorhombic (*mm2* class) phases have spontaneous polarization in <001>, <111> and <110> directions, respectively. Other phases have been detected near morphotropic boundaries in the phase diagram, especially when stress or electric field is present. There are potentially three types of monoclinic phases M_A, M_B, M_C [28]. Monoclinic phase was observed in PMN–33%PT crystals [149].

Investigations have shown that morphotropic phase boundary (MPB) compositions of the PZN-xPT and the PMN-xPT systems are in a multiphase state. Coexistence of R, M, O, or T phases leads to exceptional electromechanical properties and complex phase behavior [23,43,133]. Several researchers [29-31,134,135] have observed the coexistence of rhombohedral and tetragonal domains in PZN-xPT and PMN-xPT crystals at room temperature. A study of the MPB phases of PMN-xPT by means of high-resolution synchrotron X-ray diffraction indicated that a third phase besides R and T phases is present in the composition range of 31–37%PT at temperatures around and below 25 °C [43]. Recently the extent of different phases (R, M/O, T) in PZN-xPT and the dependency of their volume fractions on the PT content were observed [136]. It has been postulated that that coexistence of multiple phases and phase instability are critical to the extraordinary crystal properties.

The stability of the phases depends on the electrical and mechanical boundary conditions. Application of temperature, electric field and stress lead to complex polarization switching and phase transitions in these crystals and hence dramatically alter their electromechanical properties. Figure 6-1 is a schematic of crystal variants and the

possible phase transitions between them under electric field and stress loading in the <001> direction. The possible crystal variants present under the applied loads are demonstrated in the figure.

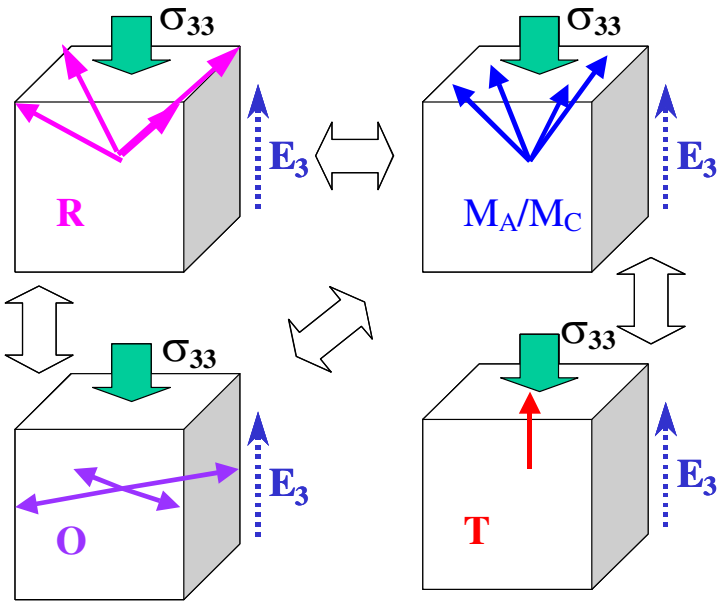

Figure 6-1. Domain structures of a <001> oriented single crystal and the possible phase transitions under <001> electric field and stress loading.

An electric field induced phase transition between the rhombohedral and tetragonal (R-T) phases has been observed by many authors [17,36,59,65,67,137]. Han and Cao [142] found that application of electric field bias along <001> decreases the R-T phase transition temperature. Ren *et al.* [65] measured the R-T phase transition fields of PZN-4.5%PT and PZN-8%PT crystals as a function of temperature and found linearly decreasing field values relative to increase of temperature. By polarizing microscope observation of temperature dependent domain structures, Schmidt *et al.* [150] and Tu *et*

al. [151] concluded that the R-T phase transition is through rotation of polarizations of monoclinic (M) phases. Phase changes along with reorientation switching induce heterogeneity in the crystals [140]. In addition, temperature and field induced phase transformations and changes of domain structures can induce cracking and fatigue that can lead to premature failure in applications.

This chapter discusses an experimental mapping of the phase transformations of <001> oriented PMN-32%PT single crystals induced by combinations of stress, electric field, and temperature loading. The experiments are described in section 6.2, results and discussion are presented in section 6.3. Section 6.4 provides some concluding remarks.

6.2 Experimental Approach

6.2.1 Test Preparation

Specimens were cut from a single boule of crystalline PMN-32%PT. They were diced with a wire saw to the final dimensions of approximately 4 x 4 x 12 mm, with the length dimension along <001> crystal orientation. Cr/Au electrodes were sputtered on the 4 x 4 mm faces in order to apply an <001> electric field. The specimens were cleaned in alcohol in an ultrasonic bath for 15 minutes and stored in a 35 °C environmental chamber overnight prior to testing.

Experiments were performed by a technician using the Stress Dependent Electromechanical Characterization System (SDECS) located at NUWC Division Newport under the supervision of Elizabeth A. McLaughlin. Refer to Section 4.2.1, this system is used to apply high electric fields, mechanical loads, and temperatures to

electroactive material specimens. The SDECS was set up to perform the following: An electric field was applied using a high voltage power amplifier and the voltage on the specimen recorded using a high voltage probe. The polarization was measured using modified Sawyer-Tower circuitry. Strain was recorded using foil strain gages connected to a Wheatstone bridge. Strain gages were placed in the center of two opposite 4 x 12 mm faces. Strain was measured along the 12 mm dimension, i.e. along x_3. The pair of strain gages on opposite faces of the specimen was connected in series to remove any small contribution to the strain from bending. A pneumatic cylinder was used to apply mechanical stress by applying a soft-spring load to a load train contained in an alignment fixture. The load was monitored using a load cell. The specimen was placed in a specimen cup and submerged in Fluorinert for electrical isolation. Once the specimen and cup were placed in the fixture, a -2 MPa preload was maintained throughout the test to contain the specimen. The pneumatic cylinder and fixture were placed in an environmental chamber to control temperature during testing.

The test setup provided stress boundary conditions. The ends of the specimen were not clamped but were free to move axially when an electric field was applied. The specimens had a 3-to-1 aspect ratio such that stress components generated by the end constraints were minimized at the center of the specimen where the strain gages were located. The electric field, polarization, strain and load data were low-pass filtered (1000 Hz) and fed into a four-channel dynamic signal analyzer. The entire measurement was automated including temperature, stress, electric field control and data acquisition.

6.2.2 Test Procedure

Table 6-1 defines the test matrix. The driving and bias electric fields were introduced via the electrodes on the two 4 x 4 mm faces, and the mechanical load was applied in this direction as well. The loading sequence progressed through each temperature, starting with the highest and stepping down to the lowest. The loading sequence is shown schematically in Figure 6-2. At each temperature a set of stress-induced strain and polarization curves were measured for a series of electrical biases. The stress cycle consisted of one half of a 0.07 Hz sine wave from a load of -2 MPa to -28 MPa (-4 kpsi) and back. The first stress-strain curve was measured with no electrical bias applied. Then the highest electrical bias field was applied to the specimen and the second stress cycle was run. Data was taken during each succeeding stress cycle for each decreasing value of field. Finally, the zero field measurement was repeated. Each measurement consisted of three averages. Prior to the three averages, two stress cycles with corresponding biases were run to determine the voltage range settings for the dynamic signal analyzer.

Table 6-1. Test conditions for the <001>-cut specimen

Test mode	Electric field (MV/m peak)	Prestress (kpsi)	Prestress (MPa)	Temperature (°C)
Stress loading, ½ sine	0, 1.51, 1.34, 1.17, 1.01, 0.84, 0.67, .51, 0.34, 0.17, 0, bias	0.3 → 4→ 0.3	2 → 28 → 2	80, 60, 50, 40, 20, 5
Electric field loading, 8 cycles	0 → 1.5 → 0	0.3, 1, 2, 3, 4, prestress	2, 7, 14, 21, 28, prestress	80, 60, 50, 40, 20, 5

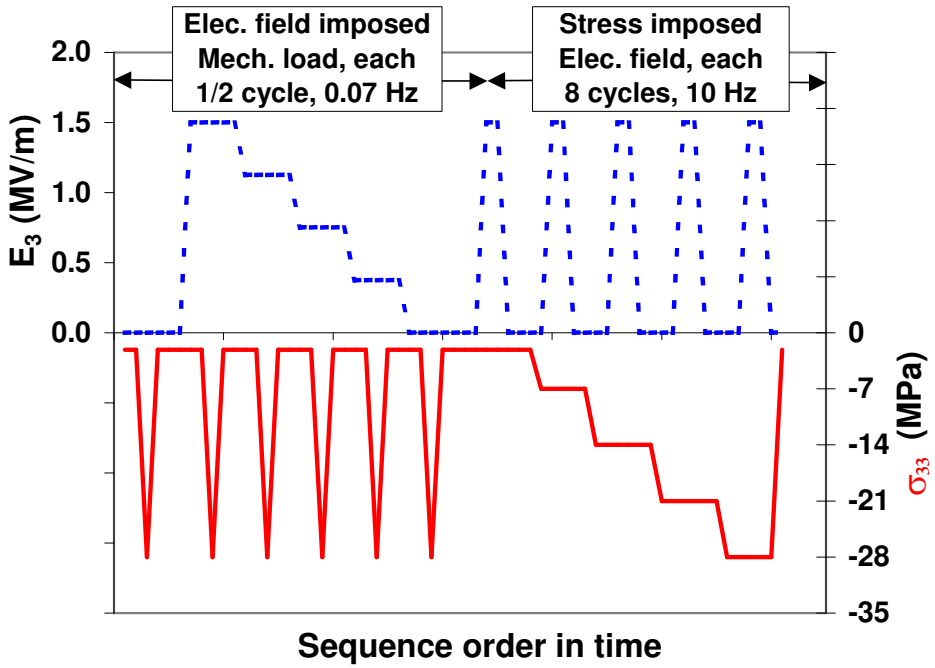

Figure 6-2. Combined electric field and stress loading scheme (test sequence).

Also at each temperature after the stress cycles were complete, field induced strain and polarization data were generated. Prior to the data measurement, two electric field signals with corresponding loads on the specimen were run to determine voltage range settings for the measurement system. The first measurement was run under -2 MPa of load and the subsequent measurements under increasing loads. The electric field signal consisted of 8 cycles of a 10 Hz sine wave. The sine wave was a biased 0.75 MV/m amplitude waveform that varied from zero to 1.5 MV/m peak. Each measurement consisted of three averages.

6.3 Results and Discussion

6.3.1 Initial Data Analysis

The recorded voltage data was processed using a MATLAB data analysis routine that applied the calibrations of the various instruments used, refer to Section 4.3.1. Drift of electric displacement data resulted in a loss of the reference value for polarization. To recover the electric displacement offset, the measured data from electric field cycling and stress loading were correlated at common loading points. First according to our measurement of *D-E* hysteresis loops, the remnant electric displacement for the <001> poled PMN-32%PT was found to be about 0.2 C/m^2. This was set as the initial value for -2 MPa prestress AC electric field loading data. This resulting data was then used to adjust the starting points for stress loading data. Now the starting points for AC field loading with -7 MPa or higher prestress were adjusted according to 0 V bias stress loading data. The electric displacement data from stress loading shows signs of drift that were induced by the instrumentation. These data sets were adjusted to meet those from AC electric field loading, which seems to be more accurate.

6.3.2 Strain and Electric Displacement Responses

Figure 6-3 shows two-dimensional plots of ε_{33}-E_3, D_3-E_3 for different pre-stress (-2, -7, -14, -21, -28 MPa) and σ_{33}-ε_{33}, σ_{33}-D_3 for different electrical bias (0, 0.17, 0.5, 1.0, 1.5 MV/m) at 20 °C data. Figure 6-3a shows the strain as a function of electric field. The vertical lines are plots of the stress-strain response at fixed bias electric fields. Figure 6-3b shows the electric displacement plotted as a function of electric field. Similarly the

vertical lines are produced by the electric displacement change when stress was applied. This plot makes clear the adjustment made to the electric displacement offset. Figure 6-3c shows the stress as a function of strain. In this case the horizontal lines are the result of electric field variation at constant stress. Figure 6-3d shows the stress as a function of electric displacement. The horizontal lines are the result of electric displacement changes induced by electric field at constant stress. Similar plots in Figure 6-4 shows evidence of several phase transformations at 60 °C.

The multivariable dependence of the material behavior is shown as three-dimensional surfaces in Figures 6-5 and 6-6 for the six temperatures (5, 20, 40, 50, 60 and 80 °C). Figure 6-5 is the strain response under stress and electric field loading. The change in slopes corresponds to temperature dependent compliance and piezoelectric coefficients. Note the reduced fields associated with onset of the phase transformations. Figure 6-6 is the electric displacement response under stress and electric field loading. The open loops seen in some of the electric displacement-stress data are likely an artifact of the instrumentation.

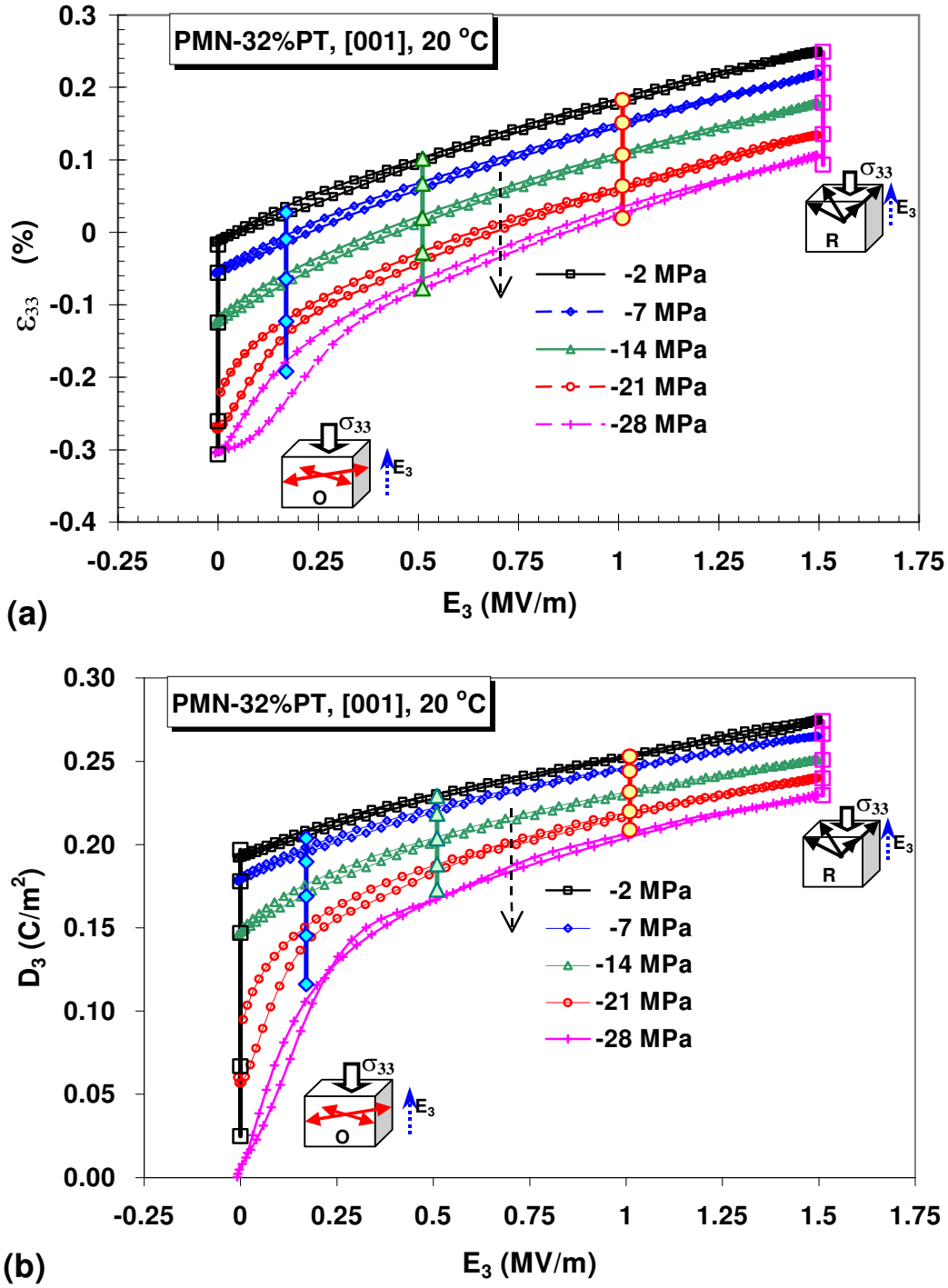

Figure 6-3. Two-dimensional plots of the room temperature data. (a) Strain vs. electric field for different prestresses, vertical lines are σ_{33}-ε_{33} at fixed E_3; (b) Electric displacement vs. electric field for different prestresses, vertical lines are D_3-σ_{33} at fixed E_3; (c) Stress vs. strain for different bias electric field, horizontal lines are ε_{33}-E_3 at fixed σ_{33}; (d) Stress vs. electric displacement for different bias electric field, horizontal lines are D_3-E_3 at fixed σ_{33}.

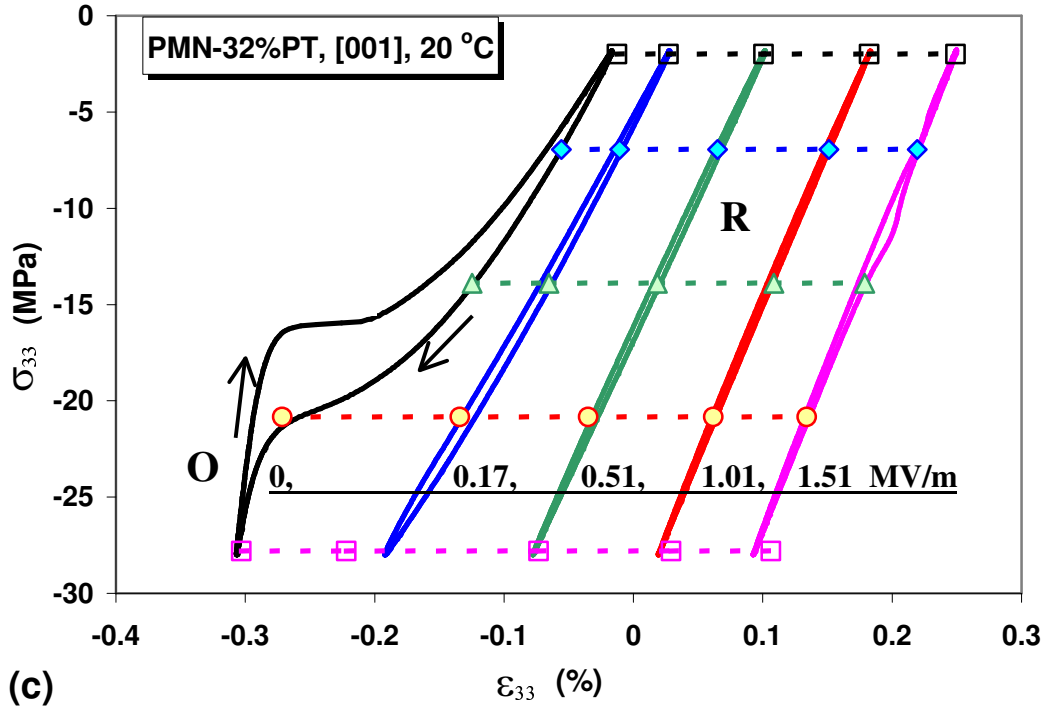

(c)

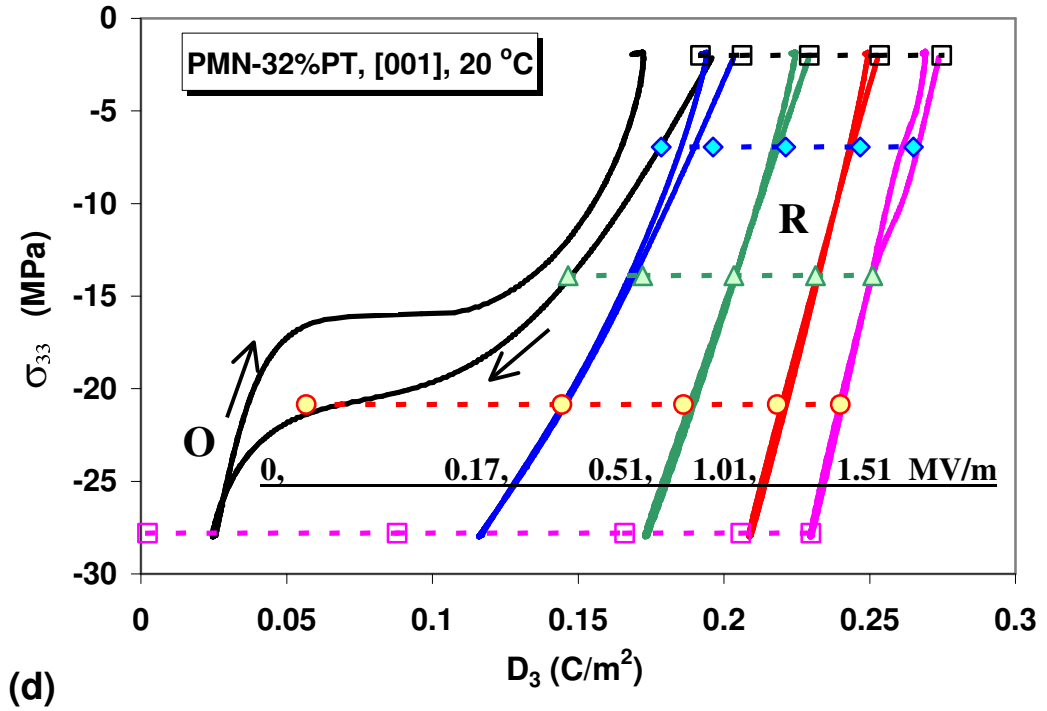

(d)

Figure 6-3 (continued).

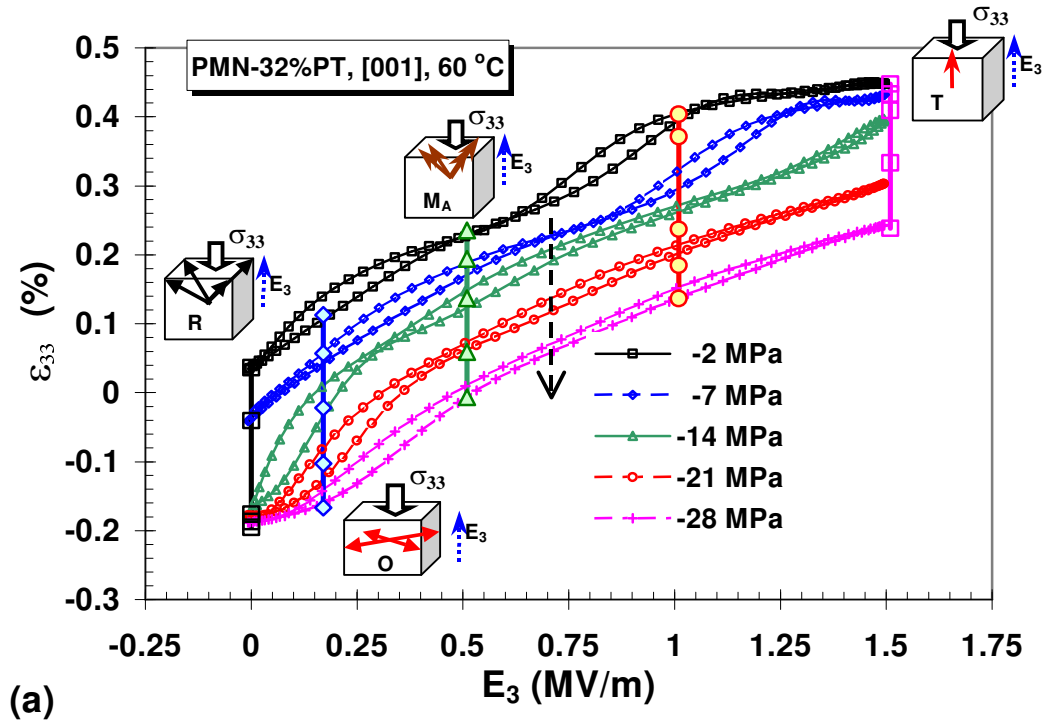

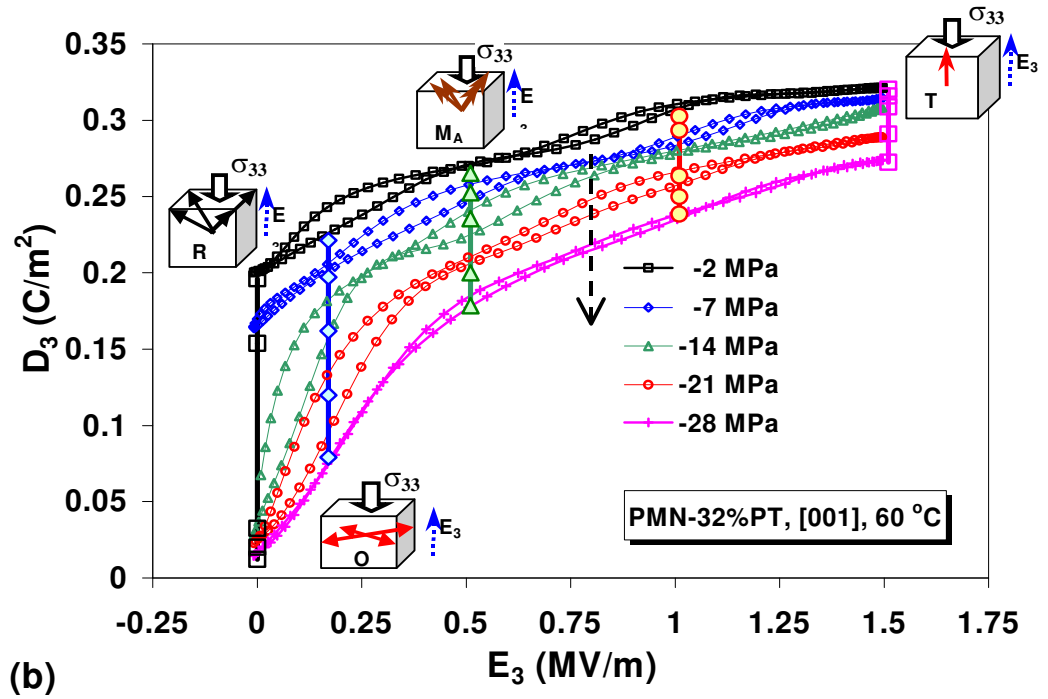

Figure 6-4. Two-dimensional plots of 60 °C data. (a) Strain vs. electric field for different prestresses, vertical lines are σ_{33}-ε_{33} at fixed E_3; (b) Electric displacement vs. electric field for different prestresses, vertical lines are D_3-σ_{33} at fixed E_3; (c) Stress vs. strain for different bias electric field, horizontal lines are ε_{33}-E_3 at fixed σ_{33}; (d) Stress vs. electric displacement for different bias electric field, horizontal lines are D_3-E_3 at fixed σ_{33}.

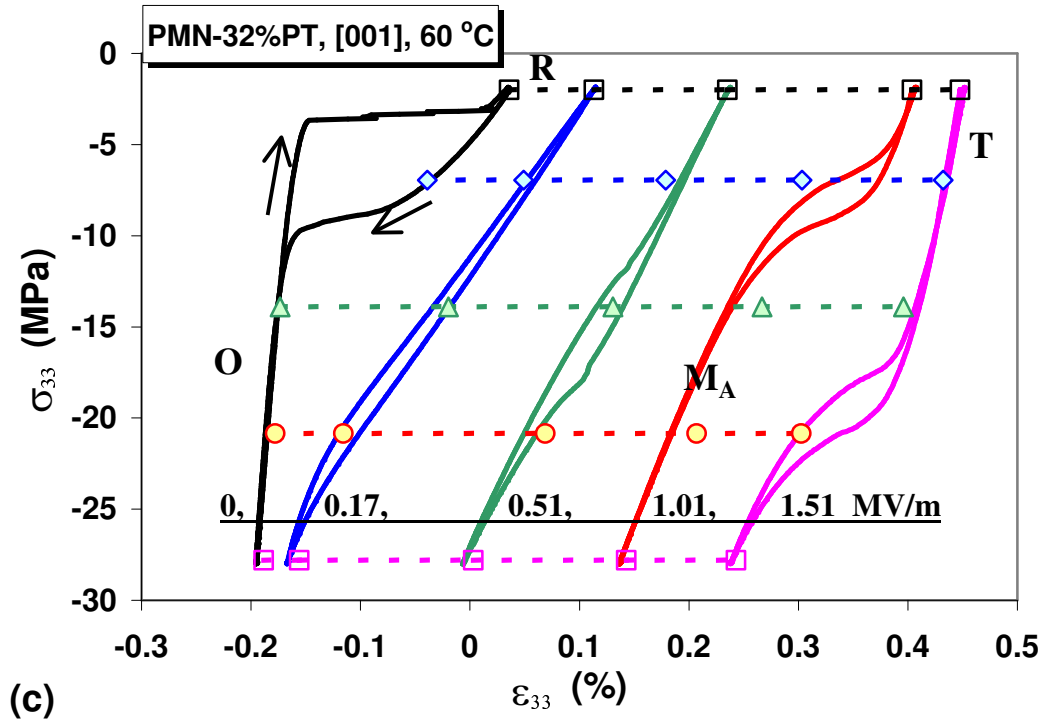

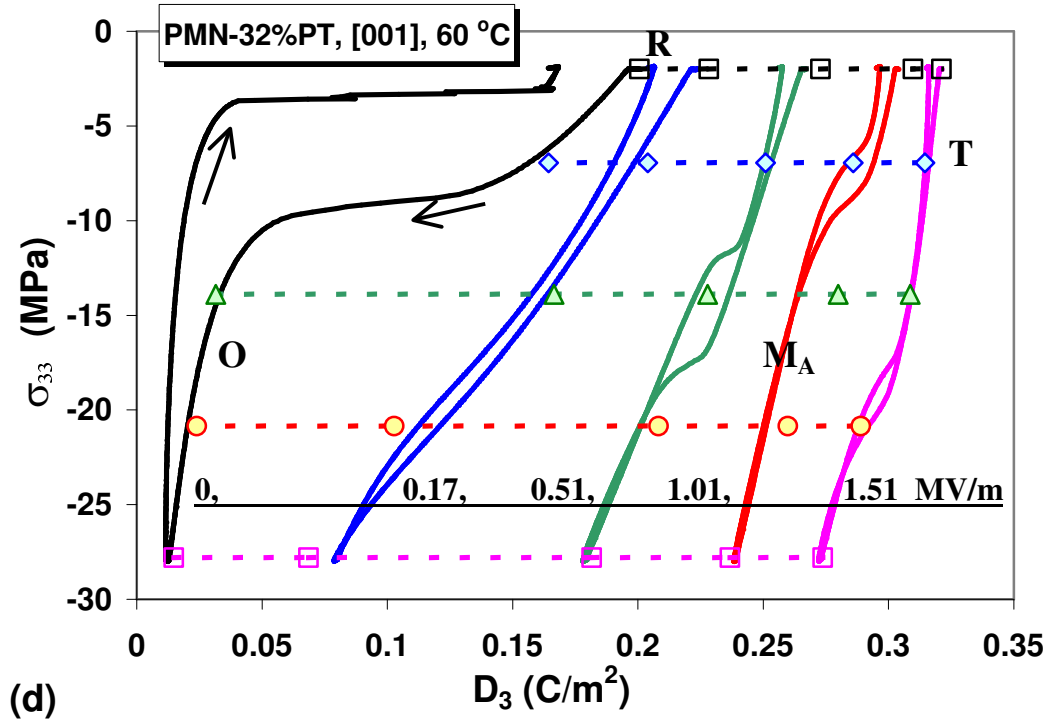

Figure 6-4 (continued).

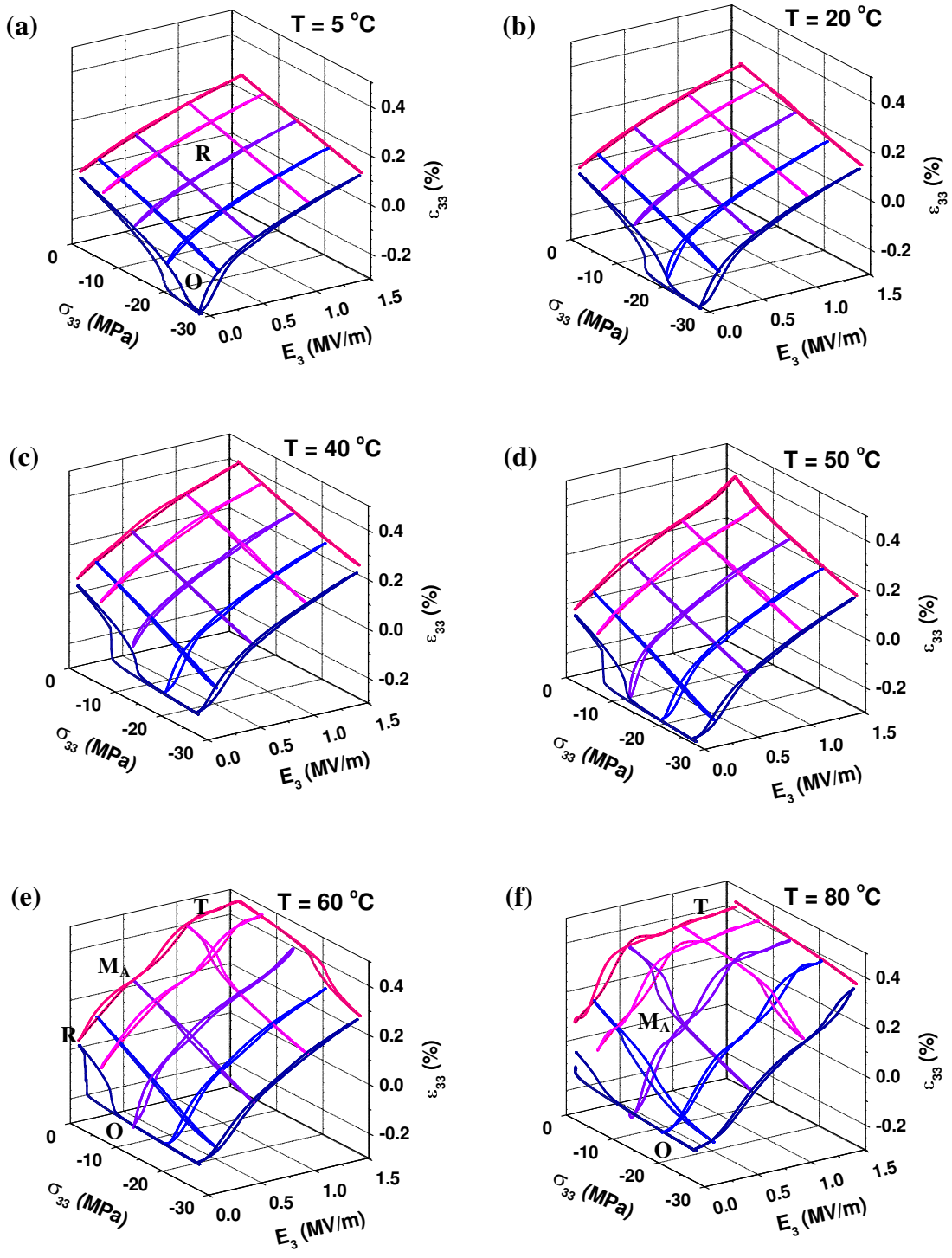

Figure 6-5. Three-dimensional plots of strain (ε_{33}) under combined electric field (E_3) and stress (σ_{33}), 5~80 °C.

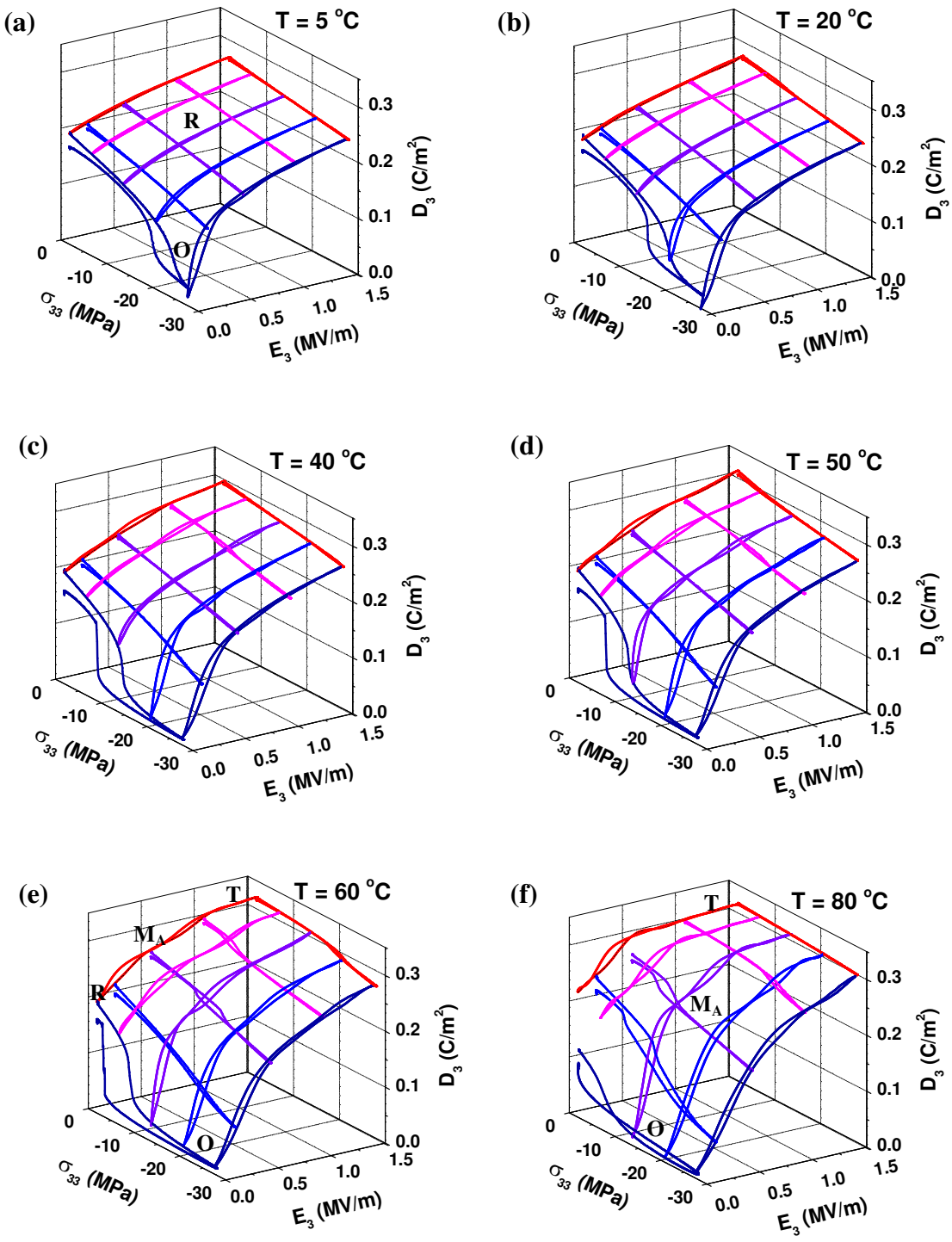

Figure 6-6. Three-dimensional plots of electric displacement (D_3) under combined electric field (E_3) and stress (σ_{33}), 5~80 °C.

The elastic, piezoelectric and dielectric coefficients of the crystal at different temperatures were obtained and listed in Table 6-2. Note that a phase exists only at specific field and temperature ranges, and there is strong temperature dependence for the elastic, piezoelectric and dielectric coefficients.

Table 6-2. Measured properties of the <001>-cut PMN-32%PT crystal

Phase	I (O) Depoled	II (R) Poled	III (M_A) poled	IV (T) poled
Piezoelectric d_{33} (pC/N)	0	2000 (5 °C) 2100 (20 °C) 2800 (40 °C) 3000 (50 °C)	1600 (40 °C) 1900 (50 °C) 2130 (60 °C) 3570 (80 °C)	700 (60 °C) 500 (80 °C)
Compliance s_{33}^E (10^{-12} m^2/N)	(s_{11}^E) 14 (20~80 °C)	67 (5 °C) 70 (20 °C) 86 (40 °C) 90 (50 °C)	65 (40 °C) 75 (50 °C) 80 (60 °C) 92 (80 °C)	29 (60 °C) 26 (80 °C)
Dielectric $K_{33}^{\sigma}(\varepsilon_0)$ (ε_0= 8.855×10^{-12} F/m)		7700 (5 °C) 8500 (20 °C) 11300 (40 °C) 13200 (50 °C)	3850 (40 °C) 4500 (50 °C) 5692 (60 °C) 11070 (80 °C)	1900 (60 °C) 1500 (80 °C)

Experimental results show that in general the electric field tends to increase the <001> strain and the electric displacement, while the compressive stress tends to decrease them. In analysis of the strain and electric displacement responses shown in Figures 6-5 and 6-6, it appears that there are 3 kinds of phase transitions among 4 phases (and therefore 4 poling states) during these loadings. Referring to a recent in situ diffraction

study of field induced phase transformations [41], the following discussion of phases is based on symmetry, loading directions, and a small degree of speculation.

6.3.3 Stress Driven R-O Phase Transition

The surface plots in Figure 6-5 and Figure 6-6 show clearly how the strain ε_{33} and electric displacement D_3 change during the application of electric field and stress. Published phase diagrams [43] identify the room temperature phase of PMN-32%PT as rhombohedral (R). Prior to testing, the R crystal was polarized into a four-domain state (on an average aspect) by the <001> electric field, producing a very large piezoelectric coefficient (d_{33} = 2000 pC/N at 20 °C). This poled 33-mode R crystal displays linear piezoelectric and dielectric response below 40 °C (Figure 6-5a~c and Figure 6-6a~c). The upper planar region is the R phase region associated with a large piezoelectric coefficient and a high compliance. The elastic, piezoelectric and dielectric coefficients of the <001> poled R crystal show strong temperature dependence with larger values at higher temperatures. The piezoelectric coefficient d_{33} increases from 2000 pC/N at 5 °C to 3000 pC/N at 50 °C, and the ultrahigh dielectric coefficient K_{33}^{σ} changes from 7700 at 5 °C to 13200 at 50 °C. The compliance s_{33}^{E} is close to the compliance s_{22}^{E} for the <110> case. This is reasonable because they are both for the <001> direction of the R phase structure.

The R-phase PMN-32%PT crystal is very close to the morphotropic phase boundary (MPB) in the temperature range of these tests. When zero electric field is applied (short circuit condition), the compressive stress in the <001> direction induces almost complete depolarization (D_3 ~ 0) and large negative strain (ε_{33} ~ -0.3%). This is in contrast with the

32-mode case (see Chapter 4) in which the <001> stress does not depolarize the <110> poled crystal but reinforces it [122]. Depolarization, decrease of strain and large hysteresis suggest that this process is a phase change from the poled R phase to an unpoled phase. The direction of applied compressive stress suggests that this phase is probably the O or T phase. This unpoled phase has an in-plane random distribution of spontaneous polarization perpendicular to <001>. Upon removal of the stress the R phase returns.

In lack of a linear region, the piezoelectric and dielectric coefficients were not measured for the depolarized phase from the test data. The piezoelectric coefficients should be very small due to depolarization (close to zero). Above 40 °C the crystal is completely depolarized by the <001> stress when there is zero electric field bias, showing linear elastic response with a compliance of 14×10^{-12} m^2/N, which is almost constant in the temperature range of 40~80 °C. This compliance is not s_{33}^E (which is defined for the poling direction) but rather s_{11}^E or s_{22}^E, because the in-plane random polarization is perpendicular to this direction. In fact its value is close to the compliance s_{22}^E for the O phase as measured in the <110> case [122]. This suggests that the depolarized phase in the <001> crystal is also an O phase.

This phase transition exists at all six temperatures when the electric field is small. Increase of temperature reduces the driving forces needed for the phase change. As the temperature increases, the O phase region grows and the phase change occurs at lower stress levels. Increase of temperature thus reduces the stress needed to drive the phase transition and increases the field required to reverse it.

At a given electric field bias the stress required to drive this phase transition reduces as the temperature increases. At a given temperature the stress required to drive the phase change increases with increasing electric field. Therefore an electric field in the poling direction can effectively prevent this phase transition and depolarization caused by the stress.

6.3.4 Electric Field Driven Phase Transitions

Refer to Figure 6-5 and Figure 6-6, electric field in the <001> direction induces additional phase changes at higher temperature. Below 40 °C and in the ranges of applied electric field and stress, the <001> poled R crystal has nearly linear piezoelectric response except for the R-O phase change. Above 40 °C, however, another phase transition is observed next to the R-O phase change as the electric field increases. This phase change is more apparent at 60 °C in the strain and electric displacement hysteresis curves and in the changes of piezoelectric and dielectric coefficients. This phase may be the M_A phase. During this phase change the <001> poled crystal displays increased strain and polarization while reduced piezoelectric coefficients d_{33}, dielectric coefficients K_{33}^{σ} and small hysteresis. At constant temperature the phase change stress and electric field are linearly dependent, increasing stress leads to increasing electric field for the phase change. Increase of temperature reduces the phase change field level.

As the temperature increases, the region for the R phase shrinks, making it difficult to determine its coefficients. When the temperature reaches 80 °C, The R phase is not shown in the strain and electric displacement plots, and there is instead a direct phase

change between the poled M_A and depolarized O phase. It implies the R phase no longer exists in the crystal above this temperature.

A third phase change is observed under high electric field above 50 °C. The onset of this phase change can be seen at 50 °C. Shown in the plots for 60 and 80 °C, this phase change leads to a major drop of piezoelectric coefficient d_{33}, dielectric coefficient K_{33}^{σ}, and elastic coefficient s_{33}^{E}. The induced phase is probably the T phase, forming a single domain state in the crystal. The electromechanical response of this phase is linear, and there is no sign of further phase transitions. After the phase change the strain ε_{33} goes above 0.4% and the electric displacement D_3 above 0.3 C/m^2.

At 80 °C only three phases are apparent. The O phase is present at low electric field, the R phase is lost in the transition between the O and M_A phases and the T phase is at the highest fields and lowest stresses. Compared to the stress induced R-O phase change, the small hysteresis associated with the other two electric field induced phase changes suggests that these transformations are a series of polarization rotations retaining an <001> polarization direction.

6.3.5 Phase Transition Map

Values of electric field (E_3), stress (σ_{33}) and temperature (T) at the onset of the R to O, R to M_A, M_A to O and M_A to T phase transitions were obtained and plotted in the E_3-σ_{33}-T coordinates, as shown in Figure 6-7 (two different views of the same data points were plotted in a and b). As shown in Figure 6-7b, except for the M_A to O phase transition, the (E_3, σ_{33}, T) points for a phase transition drop approximately into a plane.

The relationship between the stress, electric field and temperature that drive a phase transition can therefore be expressed through a planar equation. Least square fitting gives the R-O phase transition temperature (R-O plane) as $T = 73.5 + 165E_3 + 4.10\sigma_{33}$. The R-$M_A$ phase transition temperature (R-M_A plane) is $T = 52.1 - 30.2E_3 - 1.19\sigma_{33}$, and the M_A-T phase transition temperature (M_A-T plane) is $T = 90.0 - 36.2E_3 - 1.39\sigma_{33}$. It is interesting that all the three planes are almost parallel to the viewing direction in Figure 6-7b.

The R-O plane and the R-M_A plane outline the R phase region, in which the crystal maintains an engineered domain state of high performance. At the R-O plane the crystal starts to transform into an unpoled O phase and the piezoelectric properties are diminished. On the other side of the R-phase region, above the R-M_A plane there is the M_A phase region and above that, the T phase region with decreasing piezoelectric coefficients. The R-O plane and the R-M_A plane intersect and lead to an interface between the O phase and the M_A phase. The O-M_A phase boundary seems not to be a plane. More measurements are necessary in order to characterize this.

In applications, it is important to avoid these phase transitions and maintain the crystal in the high performance R phase region in order to achieve a linear piezoelectric effect. The allowable electric field (E_3), stress (σ_{33}) and temperature (T) should be maintained within this region, e.g., limit the applied stress, keep an adequate electric field bias and control the temperature. The R-O phase transition is definitely harmful and should be avoided. Comparably the R-M_A and R-T phase transitions are safer. Higher absolute strain can be obtained by going through these phase transitions with the drawback of non-linearity, reduction of piezoelectric effect and small degree of hysteresis.

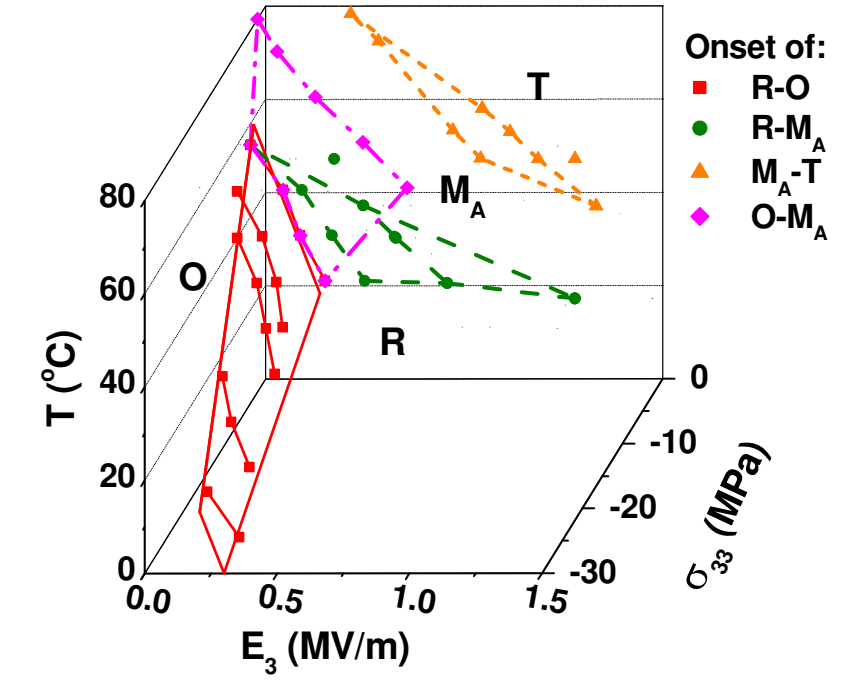

(a)

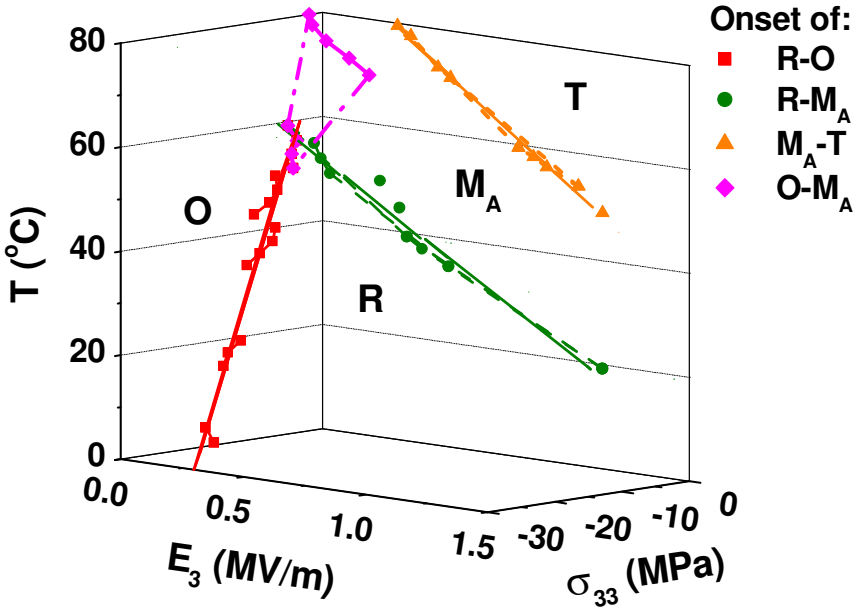

(b)

Figure 6-7. R-O phase change map in the electric field-stress-temperature (E_3-σ_{33}-T) coordinates. (a), (b) are two different views of the same map.

6.4 Concluding Remarks

The strain and electric displacement responses of the <001> PMN-32%PT single crystal under combined electric field and stress loading in the 5~80 °C temperature range were recorded. Evidence of three phase changes under combined stress and electric field loading was observed. For all three phase changes, the applied <001> stress and electric field provide the driving forces and an increase of temperature facilitates the phase changes.

These experimental results are important for actuator design and performance control. The R-O phase transformation is associated with depolarization and large hysteresis. Stress and electric field values for this phase change were measured, and the phase change criterion was given in form of a linear equation of applied electric field, stress and temperature. This criterion gives a guideline in determining acceptable applied fields on the crystal to prevent depolarization, heat generation and damage. Stress and electric field levels selected should place the operating point at the center of the planar region of the R phase.

Increased temperature reduces the allowable bias range and field excursions. The results suggest that the preferable working temperature of the crystal is below 40 °C. The data is for a single composition near the morphotropic boundary and a particular crystal cut. Additional work is needed on other compositions further from the MPB.

Acknowledgement

The author would like to thank Elizabeth A. McLaughlin at Naval Undersea Warfare Center (NUWC) Division Newport for providing the experimental data in this chapter.

CHAPTER 7

ORIENTATION DEPENDENCE OF NON-LINEARITY AND HYSTERESIS IN PZN-4.5%PT SINGLE CRYSTALS

Relaxor ferroelectric crystals exhibit excellent electromechanical properties as well as strong anisotropy. In this study compressive stress and electric field were applied to relaxor single crystals $[Pb(Zn_{1/3}Nb_{2/3})O_3]_{0.955}$-$[PbTiO_3]_{0.045}$ (PZN-4.5%PT) in a series of orientations between <001> and <111>, the corresponding strain and electric displacement were measured. It is found that as the angle of the orientation cut is rotated from <001> to <111>, dramatically the piezoelectric coefficient d_{33} drops and hysteresis loss increases. The piezoelectric coefficients, remnant strain and remnant electric displacement related to domain volume fractions were analyzed as functions of orientations. The bipolar electro-mechanical responses of the crystals including hysteresis, non-linearity and rate effect associated with polarization reorientation and phase transition were discussed.

7.1 Introduction

7.1.1 Orientation Dependence of Domain States

Rhombohedral phase of relaxor single crystals $[Pb(Zn_{1/3}Nb_{2/3})O_3]_{(1-x)}$-$[PbTiO_3]_x$ (PZN-xPT, $0<x<0.1$) and $[Pb(Mn_{1/3}Nb_{2/3})O_3]_{(1-x)}$-$[PbTiO_3]_x$ (PMN-xPT, $0<x<0.35$) exhibit excellent electromechanical properties along <001> and <110> orientations compared to the <111> (cubic cell reference) spontaneous polarization direction [8,52].

They show strong anisotropy as well as complex polarization switching and phase transitions under stress and electric field loading [122]. These crystals can be polarized into a single domain state with <111> oriented electric field. When the crystals are poled along a non-polar direction, a multi-domain state forms [8]. The crystals display large piezoelectric coefficients and low loss when poled in a <001> or <110> direction. This is the result of minimal domain wall motion in the "engineered" domain state.

For the <001> poled crystal with equal volume fractions of four variants and the <011> poled crystal with equal volume fractions of two variants, a volume averaging approach can be used to determine their piezoelectric coefficients from the single variant <111> coefficients [52,152,153]. The large shear piezoelectric coefficient d_{15} for the <111> single domain leads to very large piezoelectric coefficients (d_{33} as well as d_{31}, d_{32}) in the <001> or <011> cut.

Orientation dependence of relaxor single crystals has been studied on PZN-4.5%PT crystals with electric field applied along several directions from <001> to <111> [8,60]. Orthogonal transformations of the 3rd order piezoelectricity tensor are not sufficient to determine the piezoelectric coefficients in such orientations if the volume fractions of each variant are unknown or if there is evolution of the volume fractions during application of loads (unstable switching behavior). Domain structures and their evolution play important roles in the electromechanical response [154]. In addition, at higher (stress or electric) field levels the material may undergo field induced phase transformations. Such phase boundary motion is often hysteretic.

7.1.2 Orientation Dependence of Fatigue

External stress and electric field loading could also lead to critical issues including fracture and fatigue. Both <111> poled rhombohedral PZN-xPT (x<0.1) and <001> poled tetragonal PZN-xPT (x>0.1) tend to fatigue, while rhombohedral phase relaxor single crystals demonstrate exceptional polarization switching fatigue resistance along <001> [60]. The fatigue free nature of the rhombohedral phase in the <001> orientation is closely related to an engineered domain configuration. The aging characteristics of <001> oriented PZN-xPT and PMN-xPT single crystals were studied under electrical and mechanical drive [155], and a narrow aging range with strong non-linearity and hysteresis was found after a fatigue resistance period. Ozgul [60] argued that an engineered domain state with the polarization inclined relative to the electrode is necessary to minimize or eliminate fatigue.

Vladimir *et al*. [156] proposed that fatigue is due to a redistribution of the local internal bias field during cycling (spatially non-uniform imprint effect). As fatigue evolves in the <111> orientation, higher electric fields are required for switching due to buildup of local internal electric fields, and asymmetry of bipolar strain loops can be detected [157]. Takemura *et al*. [60] and Ozgul *et al*. [62] measured the electrical fatigue behavior as a function of orientation and suggested that the observed fatigue is the result of domain wall motion.

Yu *et al*. [49,50] investigated electric field induced domain nucleation/growth and domain switching under pulsed electric field conditions. Randomly orientated dendritic domain patterns were created under a pulsed electric field condition or during a back-switching process. The polarization relaxation behavior of PZN-xPT for <001> and

<111> orientations was studied under pulse field conditions [158], showing faster polarization relaxation in <001> than in the <111> orientation. Yin and Cao [54] studied the frequency dependence of PZN-4.5%PT crystals in several orientations responding to electric field, and a saturated coercive field representing the intrinsic switching barrier was given.

In situ TEM study of field-induced micro-cracking along 90° domain boundary in the tetragonal PMN-35%PT single crystal [159] indicates that field-induced cracking in the piezoelectric crystal prefers the domain wall as the crack path. Our microscopic observation of PZN-4.5%PT single crystals also shows a similar feature. Cracks and domain walls may introduce each other in an interactive way.

This work provides direct macroscopic measurements of hysteresis under compressive stress and electric field in a series of crystal orientations. The experimental arrangement is first introduced in Section 7.2. In Section 7.3 the initial polarization of these crystals under unipoler electric field is discussed; in Section 7.4 crystal variant volume fractions and piezoelectric coefficients as functions of orientations are analyzed based on measured remnant electric displacement. Section 7.5 focuses on the hysteresis behavior of oriented PZN-4.5%PT single crystals under both compressive stress and bipolar electric field. Switching and phase stability are discussed in Section 7.6.

7.2 Experimental Arrangement

Specimens of unpoled PZN-4.5%PT single crystals were cut to 5 mm^3 size along three orientations between <001> and <111> (10°, 25°, 35° off <001> direction), as shown in Figure 7-1a. The specimens were polished and electroded perpendicular to the

x_3-axis. Strain gages were bonded to the side surfaces to measure strains in all three directions. A strain gage rosette was bonded to the <110> faces of the 25° and 35° specimens in order to measure the shear strain ε_{23}. Due to the limit of specimen size the 0°–45°–90° rosette was actually orientated ±45° and 90°, therefore the strain component ε_{33} was directly measured while ε_{22} and ε_{23} were computed by orthogonal transformation of the Rosette data.

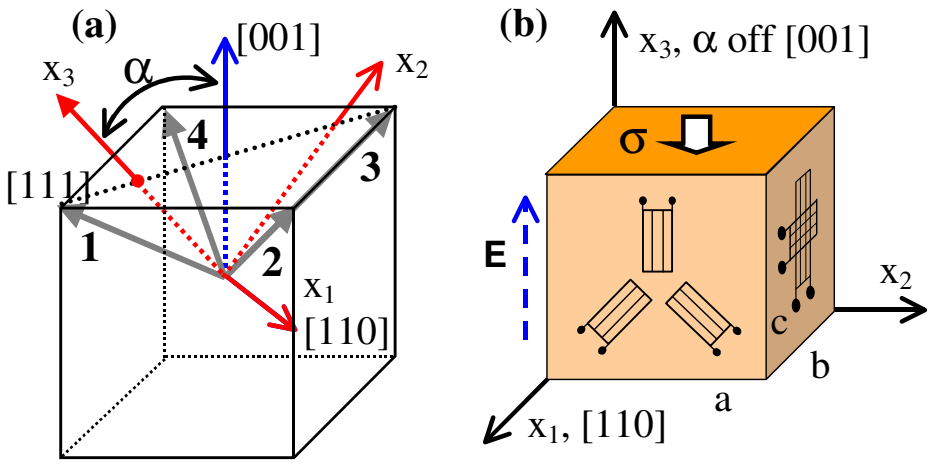

Figure 7-1. Specimen preparation for measurements. (a) PZN-4.5%PT specimens oriented α off <001>, α = 10°, 25°, 35°; (b) loading and measurement scheme.

The experimental arrangement for combined electric field and stress loading is shown in Figure 7-2. This arrangement allows combined loading of bipolar electric field and compressive stress. Teflon spacers were placed in the stress loading apparatus. This provided sufficient compliance to maintain constant stress during piezoelectric actuation.

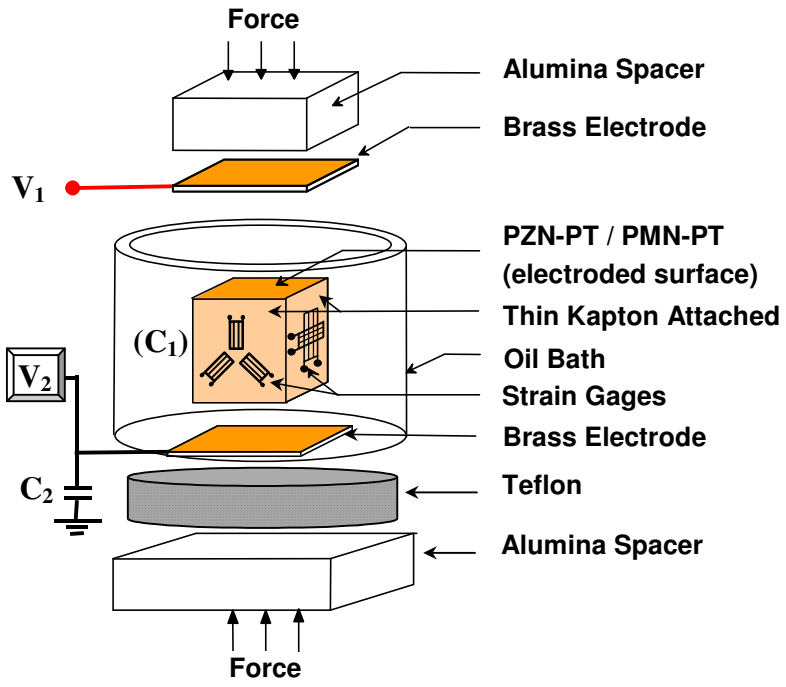

Figure 7-2. Test arrangement for combined stress and electric field loading.

The stress and electric field loading sequence are described in Figure 7-3. Compressive stress and electric field were applied in the x_3 direction. Under a small preloading stress (-0.4 MPa), the specimens were polarized by applying a bipolar electric field (triangle wave) at 0.02 Hz with amplitude of 0.4 MV/m then 0.8 MV/m (10° and 35° specimens), or 0.8 MV/m from the beginning (25° specimen). Two complete cycles on the unpoled crystal are necessary in order to obtain a full and symmetric hysteresis curve. The stress magnitude was then increased in 10 MPa increments to a maximum of 30 MPa (40 MPa for the 10° specimen, in which damage was observed at this stress level). At each hold level an electric field cycle was applied. The stress was then unloaded back to the preloading level, and the electric field was applied again.

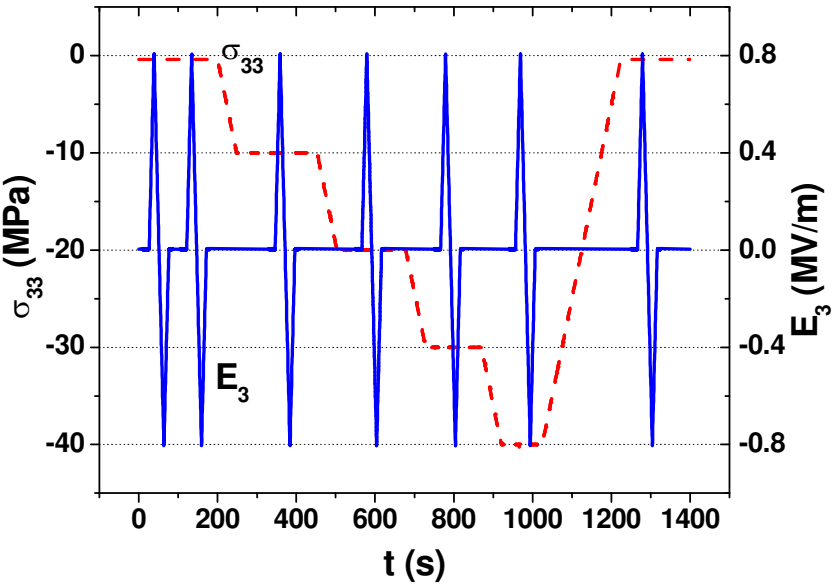

Figure 7-3. Stress and electric field loading procedure.

Applied force was controlled by a digital DC servo-controlled electromechanical test system and voltage was from a function generator and amplifier. Strain gages were connected to a Wheatstone bridge signal conditioner. Applied voltage was monitored and the electric displacement was measured using a Sawyer-Tower circuit. All signals were digitally recorded.

7.3 Initial Polarization

Figure 7-4 plots the electric displacement and three-axial strains for these three specimens during the initial half cycle. It shows that the strain and electric displacement responses for the three crystal orientations are much different. Shown in Figure 7-4a, the saturated and remnant electric displacement increase with orientation angle. Figure 7-4b shows the strain components ε_{11}, ε_{22}, ε_{33} for the 10° specimen. Note that the strain and

electric displacement values for the 10° orientation were from two 10° specimens. The electric displacement data was obtained from a second sample due to a problem in measurement of the first sample. The initial electric field maximum in the strain data was not of full (0.8 MV/m) magnitude; therefore the strains under higher electric field (after polarization switching) were also plotted in Figure 7-4b. Shift of remnant strain from initial (incomplete) polarization at 0.4 MV/m was observed. Such a big shift was not observed for the 35° specimen under the same loading (Figure 7-4d). Shear strain ε_{23} for the 10° specimen was not measured. Its value should be small. In fact, shown In Figure 7-4c and 7-4d, the piezoelectric shear strain ε_{23} was small for both the 25° and 35° specimens. Therefore the shear piezoelectric coefficient d_{323} is small. For the 35° specimen the apparent larger d_{323} value at lower field level is in fact a depolarization effect.

According to the observation, the initial polarization for the 10° specimen is somewhat gradual and the specimen was not fully polarized until the electric field is above 0.6 MV/m, while it is almost instantaneous for the 25° and 35° specimens. The coercive field (E_c) in the initial polarization is about 0.3 MV/m. The initial E_c (at the point of highest strain and electric displacement rate) decreases a little bit with increasing orientation angle (α).

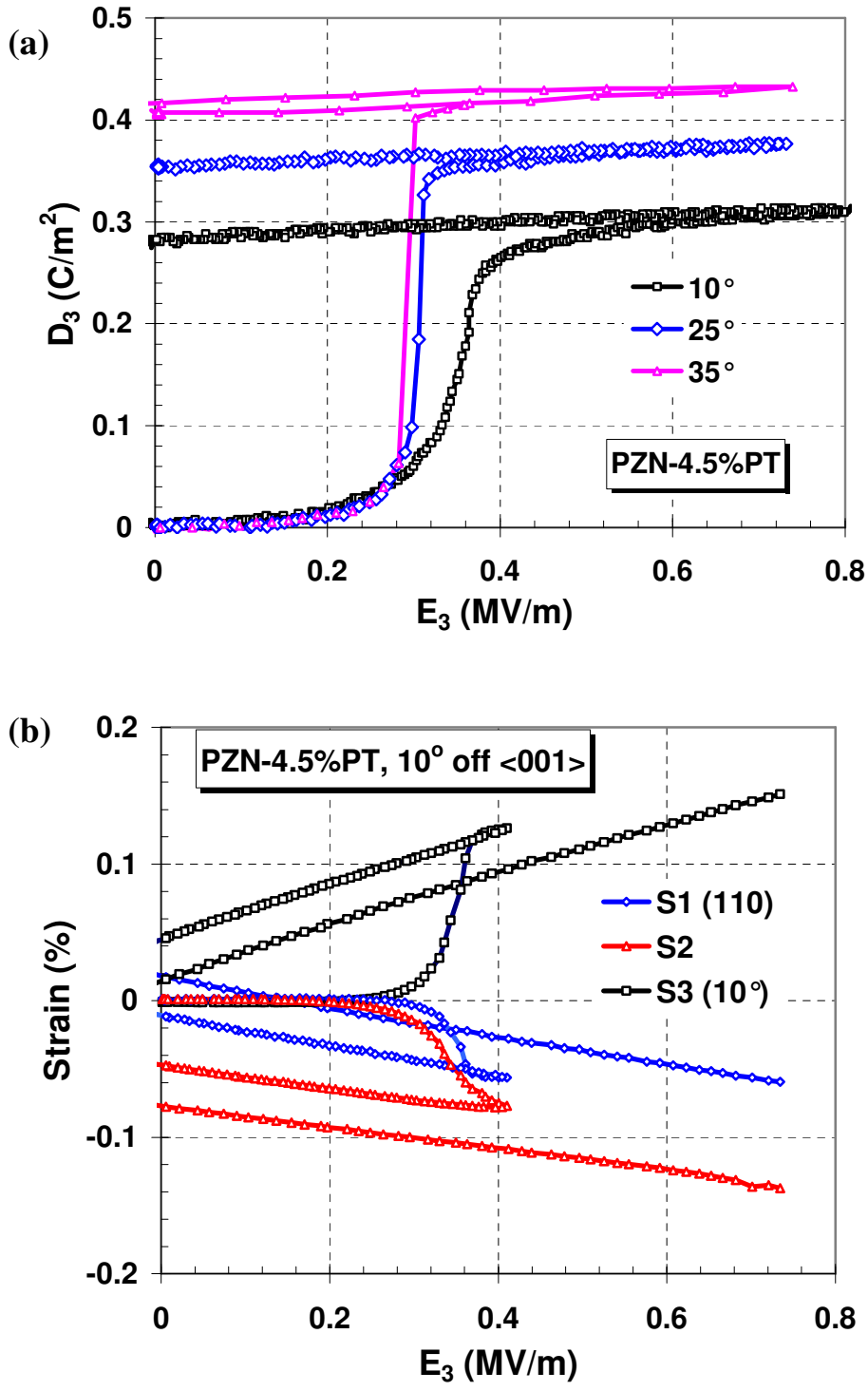

Figure 7-4. Strain and electric displacement response under initial polarization. (a) Electric displacement vs. electric field for 10°, 25°, 35° specimens; (b) Strain vs. electric field for the 10° specimen; (c) Strain vs. electric field for the 25° specimen; (d) Strain vs. electric field for the 35° specimen.

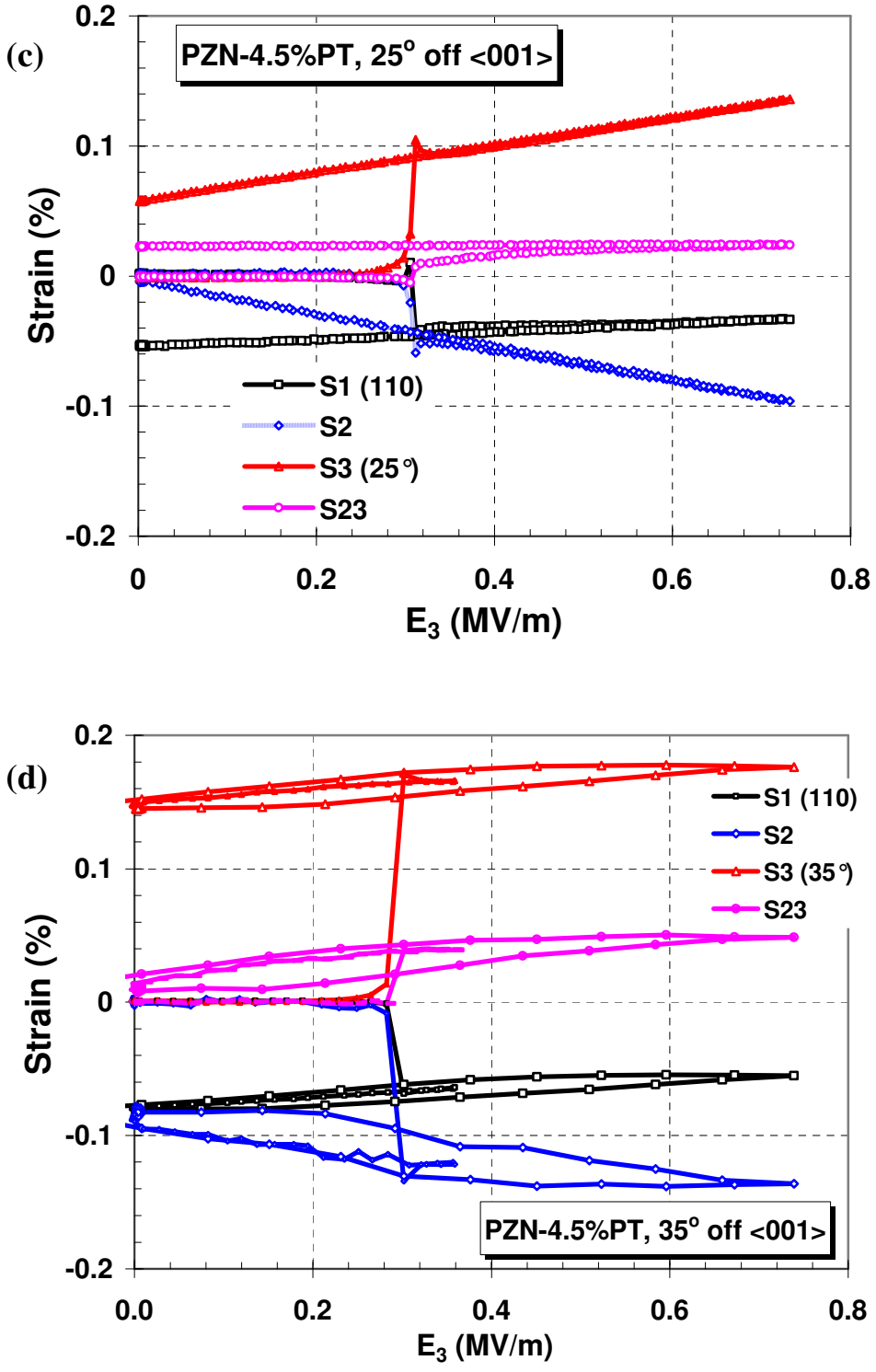

Figure 7-4 (continued).

7.4 Domain Analysis

Plotted in Figure 7-5a, the remnant electric displacement D_3^r is shown to increase with orientation angle α. These values are in good agreement with Takemura *et al.*'s measurements [60] and a little higher than those by Park and Shrout [8]. As shown in Figure 7-5a, D_3^r is relatively insensitive to small orientation changes around the <001> or <111> direction, while it increases rapidly in the range of 15° to 30°.

By applying a model based on volume averaging of crystal variants, the volume fractions of the four domains with an acute angle to the poling direction were computed by satisfying D_3^r. There are totally eight crystal variants in a rhombohedral PZN-xPT crystal. Once completely polarized, there should be at most four variants present in any specimen poled along α off <001> ($0 \le \alpha \le 54.7°$), as shown in Figure 7-1. Let f_1, f_2, f_3, f_4 be their volume fractions, then $f_1 + f_2 + f_3 + f_4 = 1$ ($f_1 \ge f_2, f_3, f_4 \ge 0$). The subscripts on the volume fractions correspond to the variants as labeled in Figure 7-1. It is found that the remnant electric displacement in the poling direction depends only on α and $(f_1 - f_3)$:

$$\begin{aligned} D_3^r/D^s &= (f_1 + f_2 + f_3 + f_4)\cos(54.7°)\cos(\alpha) + (f_1 - f_3)\sin(54.7°)\sin(\alpha) \\ &= \cos(54.7°)\cos(\alpha) + (f_1 - f_3)\sin(54.7°)\sin(\alpha) \end{aligned} \tag{7-1}$$

or

$$(f_1 - f_3) = [D_3^r/D^s - \cos(54.7°)\cos(\alpha)]/[\sin(54.7°)\sin(\alpha)] \tag{7-2}$$

In the <001> oriented crystal, the polarization vectors of each of the crystal variants make equal angles with the <001> direction. This enables calculation of the <111>

polarization vector. Assuming a fully polarized 4-varant state, the measured D_{001}^r = 0.265 C/m^2 for the <001> case correlates to a spontaneous electric displacement of $D^s = \sqrt{3}D_{001}^r$ = 0.459 C/m^2. This value is a little higher than the measured remnant electric displacement for the <111> crystal, which is reasonable considering the depolarization (incomplete polarization) in the <111> crystal. Letting D^s = 0.459 C/m^3 and D_3^r as measured values in Equation 7-2 leads to the value of $(f_1 - f_3)$ as a function of orientation α. $f_3 \geq 0$, therefore this function directly gives the minimum of f_1 (when f_3 = 0). At the same time $f_1 + f_3 \leq 1$ ($f_2 + f_4 \geq 0$), so f_1 has a maximum of $(f_1 - f_3)/2$+0.5.

The <001> oriented crystal is generally assumed to comprise equal volume fractions (0.25) of four variants, but there could be a different domain structure such as $f_1 = f_3 = 0$ or $f_1 = f_3 = 0.5$ as was observed [160]. Including this extreme case, the maximum and minimum values of f_1 are plotted as functions of α in Figure 7-5b. Also plotted in the figure are the maximum value of f_3 (when f_1 = max., f_2, f_4 = 0) and the maximum of $(f_2 + f_4)/2$ (when f_1 = min., f_3 = 0). The gap between the maximum and minimum of f_1 happens to be the same as the maximum value of f_3 as well as the maximum of $(f_2 + f_4)/2$. f_2 and f_4 can be considered equal statistically. Letting $f_2 = f_4$ leads to $D_1^r = 0$. When D_3^r is satisfied, D_2^r is a small non-zero value independent of f_1.

The volume fraction analysis shows that although D_3^r changes slowly as α deviates from <001>, f_1 increases quickly to satisfy D_3^r. At α of 30°, there is over 80% volume fraction of this crystal variant. It is shown that the polarization concentrates to a single <111> variant when α is larger than 35°.

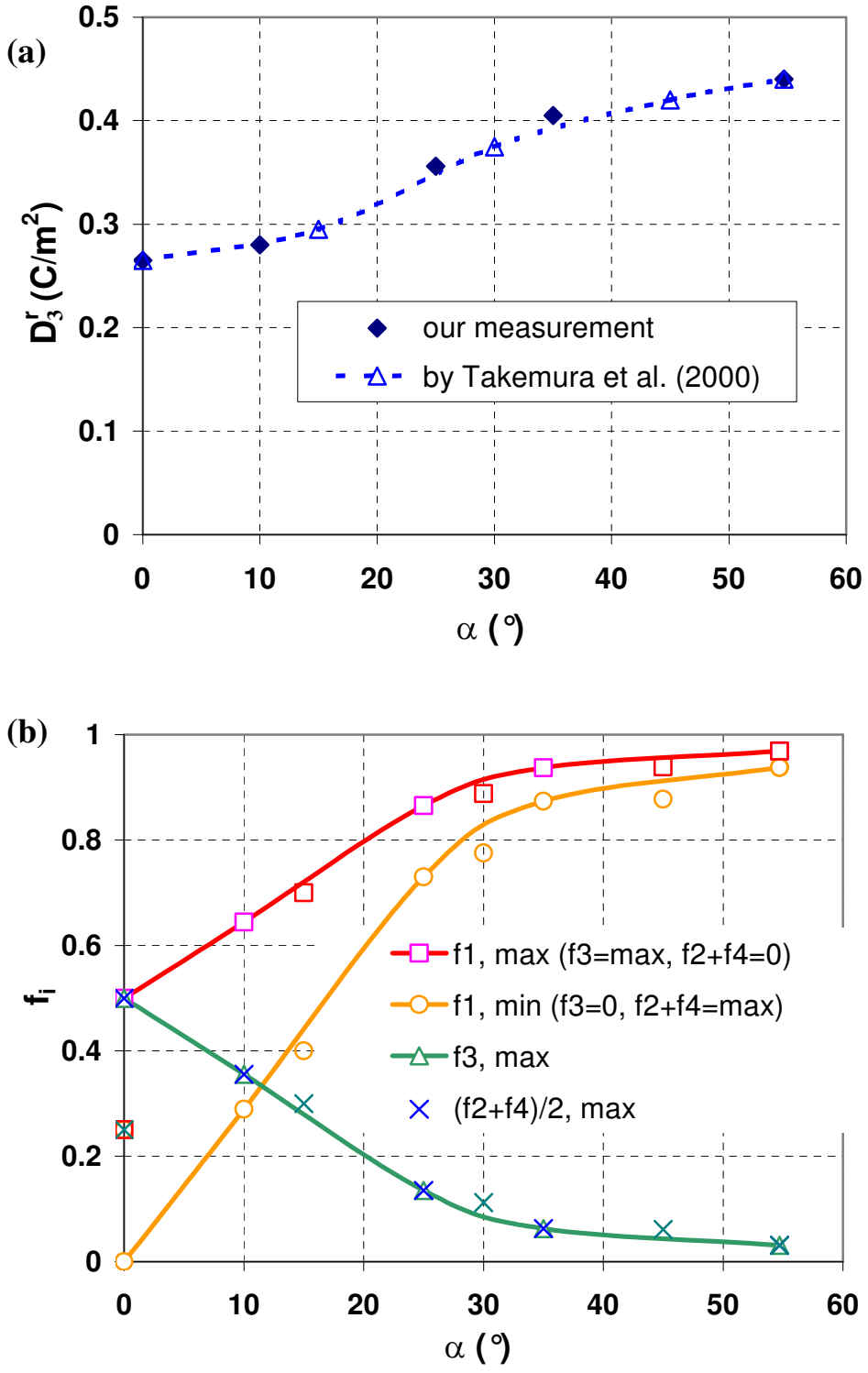

Figure 7-5. Orientation dependence of crystal properties. (a) Measured remnant electric displacement; (b) Domain volume fractions; (c) Piezoelectric coefficients; (d) Remnant strain.

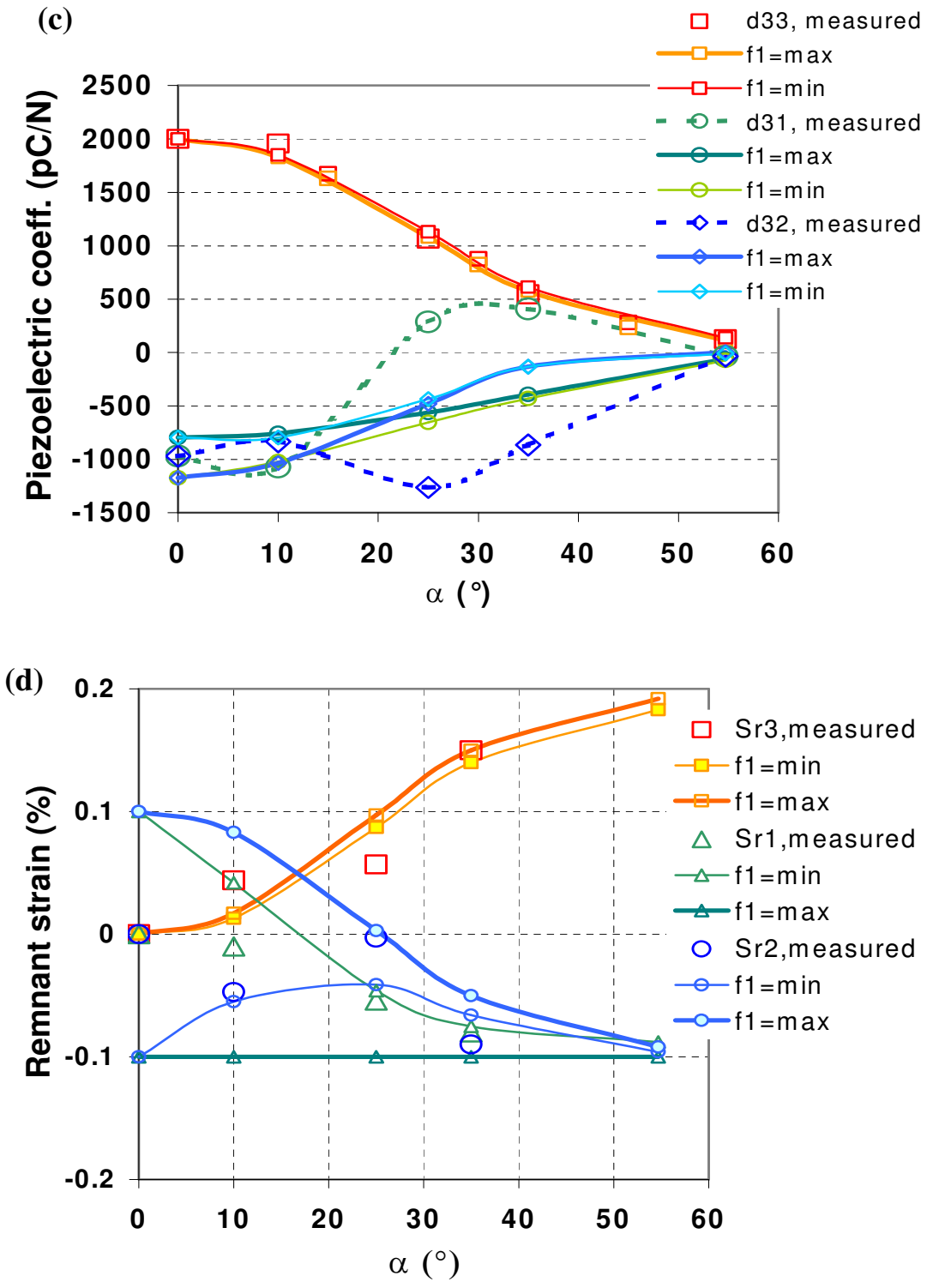

Figure 7-5 (continued).

Piezoelectric coefficients were obtained from the initial polarization data and plotted in Figure 7-5c, with d_{33} = 2000 pC/N in the <001> direction and 120 pC/N in the <111> direction adopted [161]. As the angle of the crystal cut rotates from <001> to <111>, the piezoelectric coefficient d_{33} drops dramatically with increasing hysteresis. The 10° specimen shows linear piezoelectric behavior similar to a <001> oriented crystal, the 35° specimen shows non-linearity and hysteresis similar to a <111> oriented crystal, and the 25° specimen shows some mixed features between. The piezoelectric coefficient d_{31} is negative and close to d_{32} for the 10° specimen, while interestingly it became positive for both 25° and 35° samples.

From a set of piezoelectric coefficients for the <111> domain (with local coordinates x_1–x_2–x_3 in <-110>, <-1-12>, <111> directions): d_{33} = 125, d_{31} = -35, d_{15} = 3824, d_{16} = -1902 (pC/N) [161], the piezoelectric coefficients were computed by orthogonal transformations according to the obtained bounds of volume fractions shown in Figure 7-5b. Results were plotted in Figure 7-5c for comparison with measured data. It shows that as long as D_3^r is satisfied, the computed d_{33} is in good agreement with the measured data. Variance of volume fractions between the bounds shown in Figure 7-5b doesn't change much of d_{33} value. It predicts some difference between d_{31} and d_{32} but not the abnormal results measured for the 25° and 35° specimens. Such results might be related to complex domain interactions or coexistence of a second phase (such as monoclinic), which is not captured in the crystal variant volume averaging analysis.

Figure 7-5d plots the remnant strain components versus crystal orientation. Computations are based on the volume fractions in Figure 7-5b and a spontaneous strain of 0.2% for a (<111> poled) unit cell. According to the computation, variance of volume

fractions between the bounds doesn't change the ε_{33}^r value much, but may induce large variance of ε_{11}^r and ε_{22}^r values between $\pm 0.1\%$, which is as large as a half of the spontaneous strain. Computational results seem to be in agreement with measurements. Note that for the 10° specimen there were large changes of remnant strains from initial polarization to bipolar switching cycles, suggesting evolution of crystal variants, domain structures, or possibly evolution of a second phase.

7.5 Hysteresis Loops under Stress and Electric Field Cycling

7.5.1 10° *Sample*

Figure 7-6 shows the experimental results for the 10° specimen under electric field cycling with pre-stress. Figure 7-6a is the strain versus electric field plot and Figure 7-6b the electric displacement versus electric field plot, under different pre-stress. Figure 7-6c and 7-6d are respectively the stress-strain and stress-electric displacement curves. Strain data for pre-stress up to -40 MPa is available and included in Figure 7-6a and 7-6c.

Due to the compliance of the specimen, the strain versus electric field hysteresis loops in Figure 7-6a show a vertical offset, which is the decrease of the strain as the magnitude of compressive stress increases. The offset (and also the compliance) is large when the magnitude of the stress is within 20 MPa, but becomes much smaller when the stress is above 20 MPa.

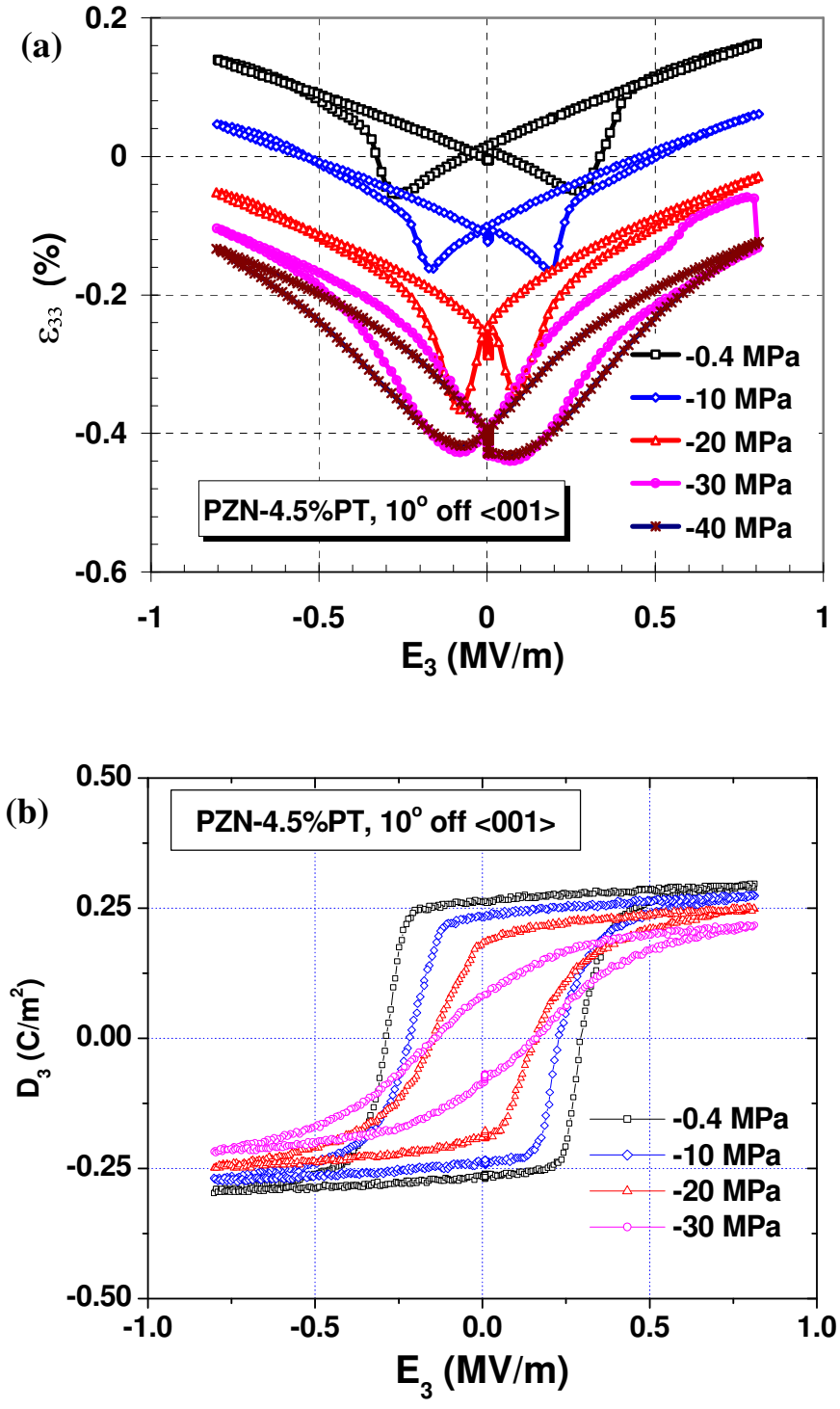

Figure 7-6. The 10° specimen under stress and electric field loading. (a) Strain vs. electric field; (b) Electric displacement vs. electric field; (c) Stress vs. strain; (d) Stress vs. electric displacement.

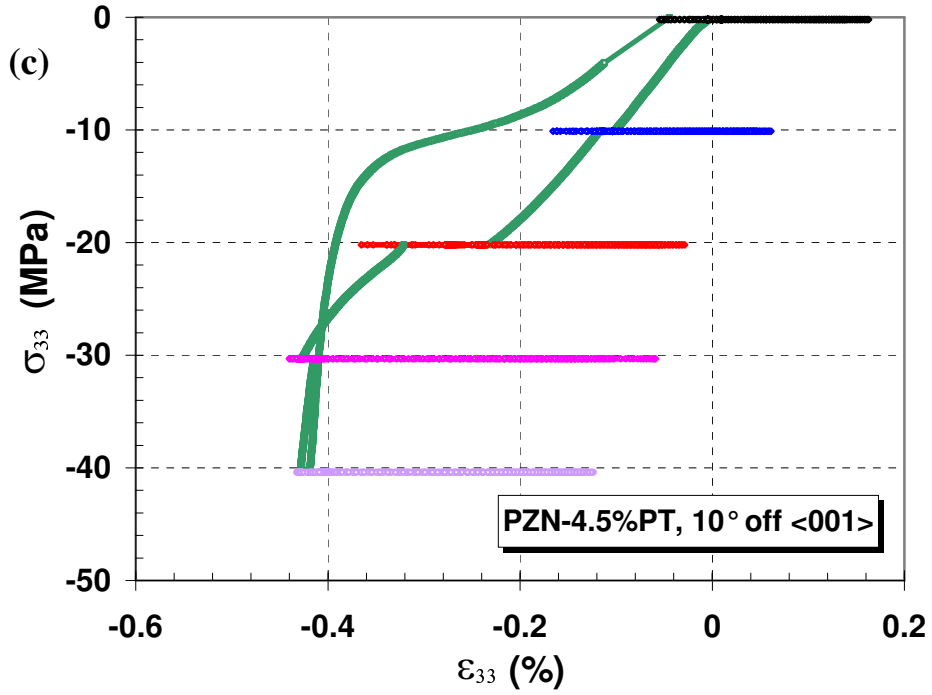

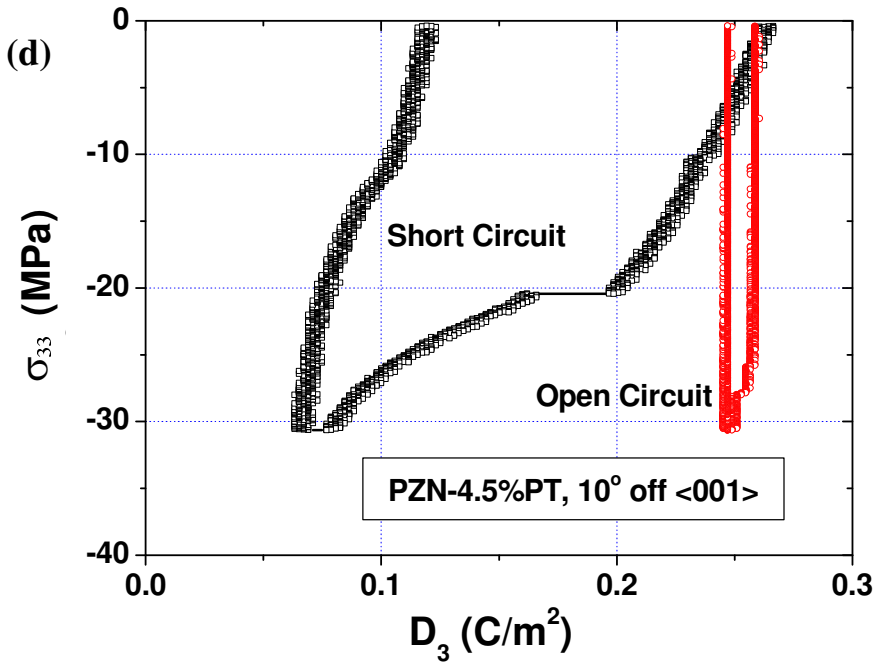

Figure 7-6 (continued).

As shown in Figure 7-6, the electromechanical response of the 10° crystal is similar to that of a <001> oriented specimen [8]. When the magnitude of the pre-stress is no more than 10 MPa, the response under electric field is linear piezoelectric strain associated with large piezoelectric coefficient d_{33} and a typical 180° polarization switching. When the magnitude of pre-stress is increased to 20 MPa, nonlinear piezoelectric strain, 90° type of switching and depolarization can be observed. Depolarization is apparent as it leads to large reduction of remnant strain and remnant polarization. Typically when the electric field is unloaded back to zero with -20 MPa pre-stress held, the strain and electric displacement continue to decrease (creep), as reflected by the flat regions in Figure 7-6c,d. The coercive field decreases as the pre-stress increases. Yet at higher stress levels, the polarization process becomes slower (flatter), polarization saturation requires a higher electric field, and the non-linearity of piezoelectric response becomes severe.

At -30 MPa there is an abrupt variation at the upper-right segment of the strain versus electric field hysteresis loop. This is probably due to temporary non-uniform domain activities in the specimen. The strain recovered back to the "normal" value during unloading and this variation did not seem to affect the later measurement.

Under short circuit condition, the stress-strain curve shows large stress-induced strain, change of compliance and strain recovery upon unloading (Figure 7-6c). The stress-polarization curve with short circuit condition shows large depolarization and partial recovery after unloading (Figure 7-6d). They reflect a phase change that is similar to the R-O phase change observed in <001> PMN-32%PT crystal (Refer to Chapter 6). The R phase undergoes R-O phase change at about -20 MPa and back to R phase upon

unloading, but the poling state is depolarized during the R-O phase transition and is not re-polarized completely under short circuit condition. Under open circuit condition, there is almost no depolarization with stress up to 30 MPa.

7.5.2 25° Sample

Figure 7-7 shows the results for the 25° specimen. In this case the curves have some unique features. The piezoelectric response of this cut is still linear at low pre-stress. At -0.4 MPa pre-stress the bottoms of the strain vs. electric field hysteresis loop (early stage of switching reversal) are somewhat flat. This is probably due to a rearrangement process of different domain variants. As the compressive pre-stress is increased to 10 MPa, the hysteresis loop changes the shape remarkably. The 180° type of switching change to the typical 90° type with a sharp tip. As the pre-stress is further increased, the hysteresis loops change shape again, forming flat bottoms of strain vs. electric field curve. Similar to the case of the 10° specimen, the coercive field decreases as the pre-stress is increased, but up to 20 MPa there is little depolarization and the polarization process is sharp.

The stress-strain curve for the 25° sample shows relatively good linearity for loading and unloading. There is, though, large depolarization and creep behavior when the stress reaches 30 MPa under short circuit condition, featuring a 90° switching.

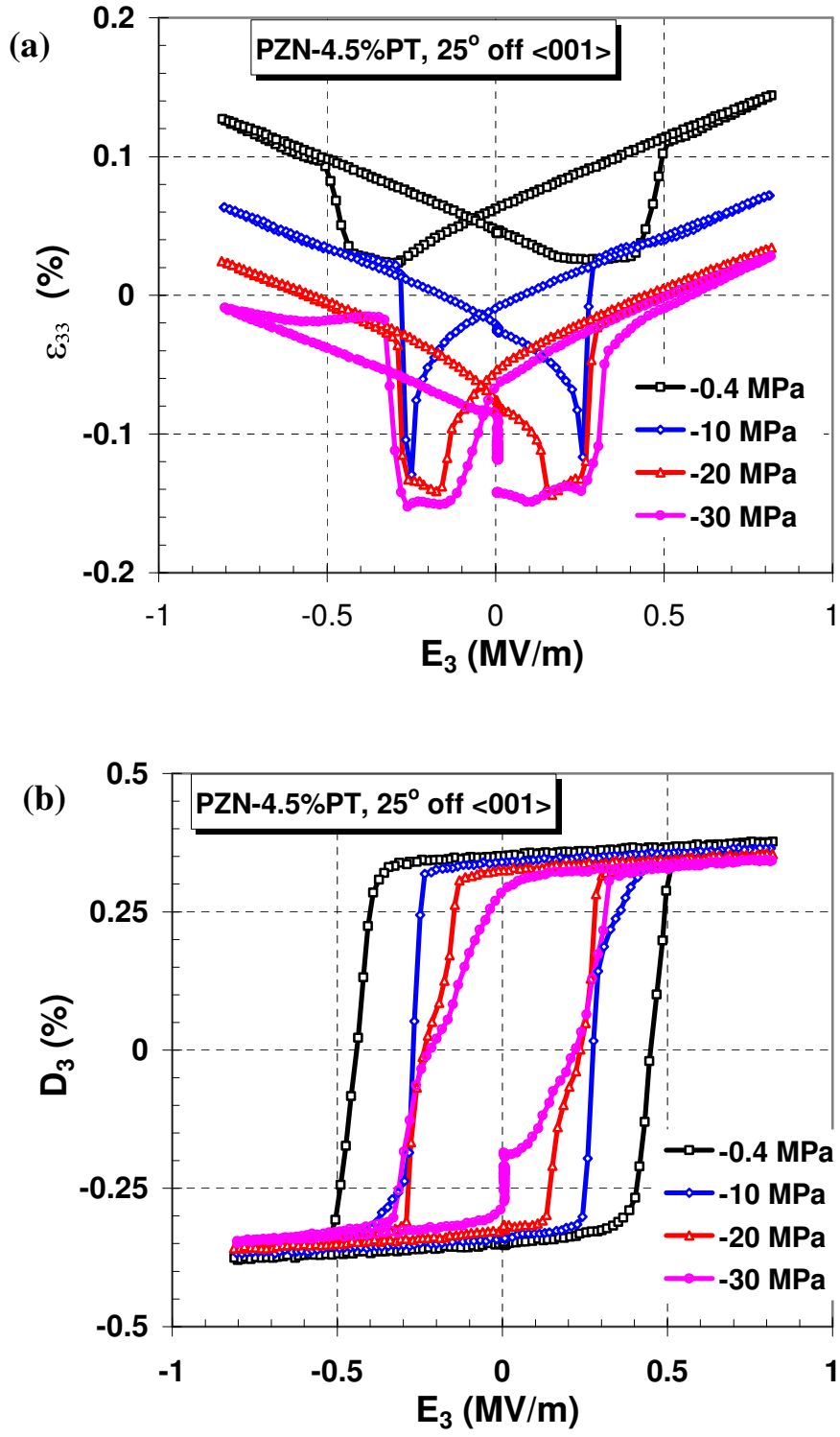

Figure 7-7. The 25° specimen under stress and electric field loading. (a) Strain vs. electric field; (b) Electric displacement vs. electric field; (c) Stress vs. strain; (d) Stress vs. electric displacement.

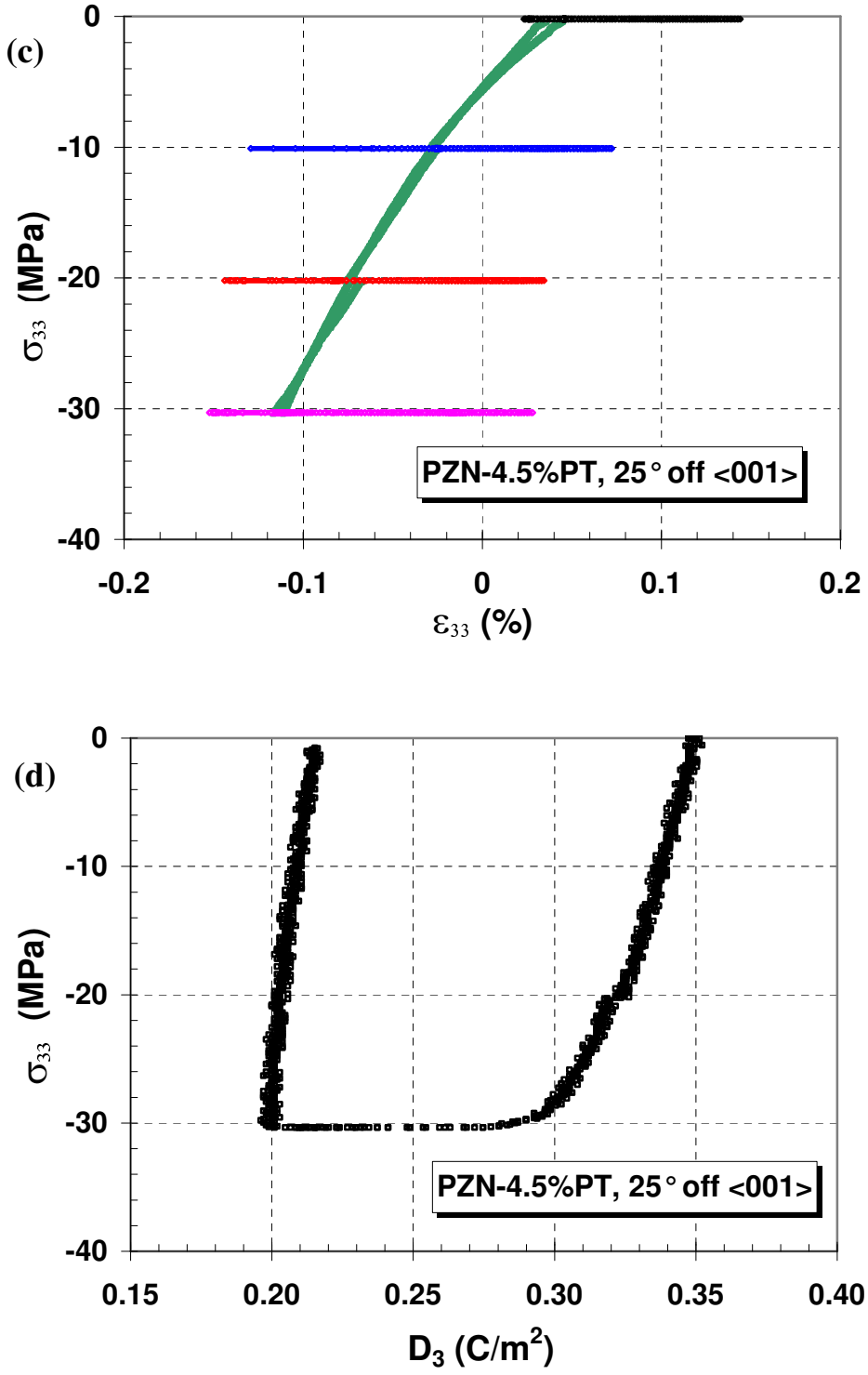

Figure 7-7 (continued).

At -30 MPa the strain showed non-symmetric response to positive and negative electric field, while the electric displacement did not. This can be explained by the different measurement methods for strain and electric displacement. Strain was measured by small strain gages glued on the surface of the specimen that measures local strain, while the electric displacement (D_3) was obtained by measuring the charge on the electrode surface and averaging over the surface. Unfortunately domain inhomogeneity may result from tilting of stress loading. Therefore non-uniform strain due to non-uniform domain or phase state in the specimen was reflected in the strain measurement but not in electric displacement measurement. Recorded data shows that the same strain component ε_{33} measured on two surfaces may have a variance of 15%.

7.5.3 35° *Sample*

Figure 7-8 shows the results for the 35° specimen. The strain and electric displacement responses are similar to those for a <111> cut. The rhombohedral crystal is polarized gradually, large remnant strain and remnant polarization in the poling direction are shown after unloading. Typical 90° switching (which is actually 71° or 109° switching) feature is shown at small pre-stress, and the piezoelectric strain is much smaller. Yet the polarization is pretty stable compared to a <111> case.

As the stress is increased, the strain versus electric field hysteresis loops change considerably. The bottoms of the loops open up and the area within the loops increase. The pre-stress strongly forces depolarization and delays re-polarization. Severe creep is observed when the pre-stress is above 20 MPa. The coercive field decreases only a little bit as the pre-stress is increased.

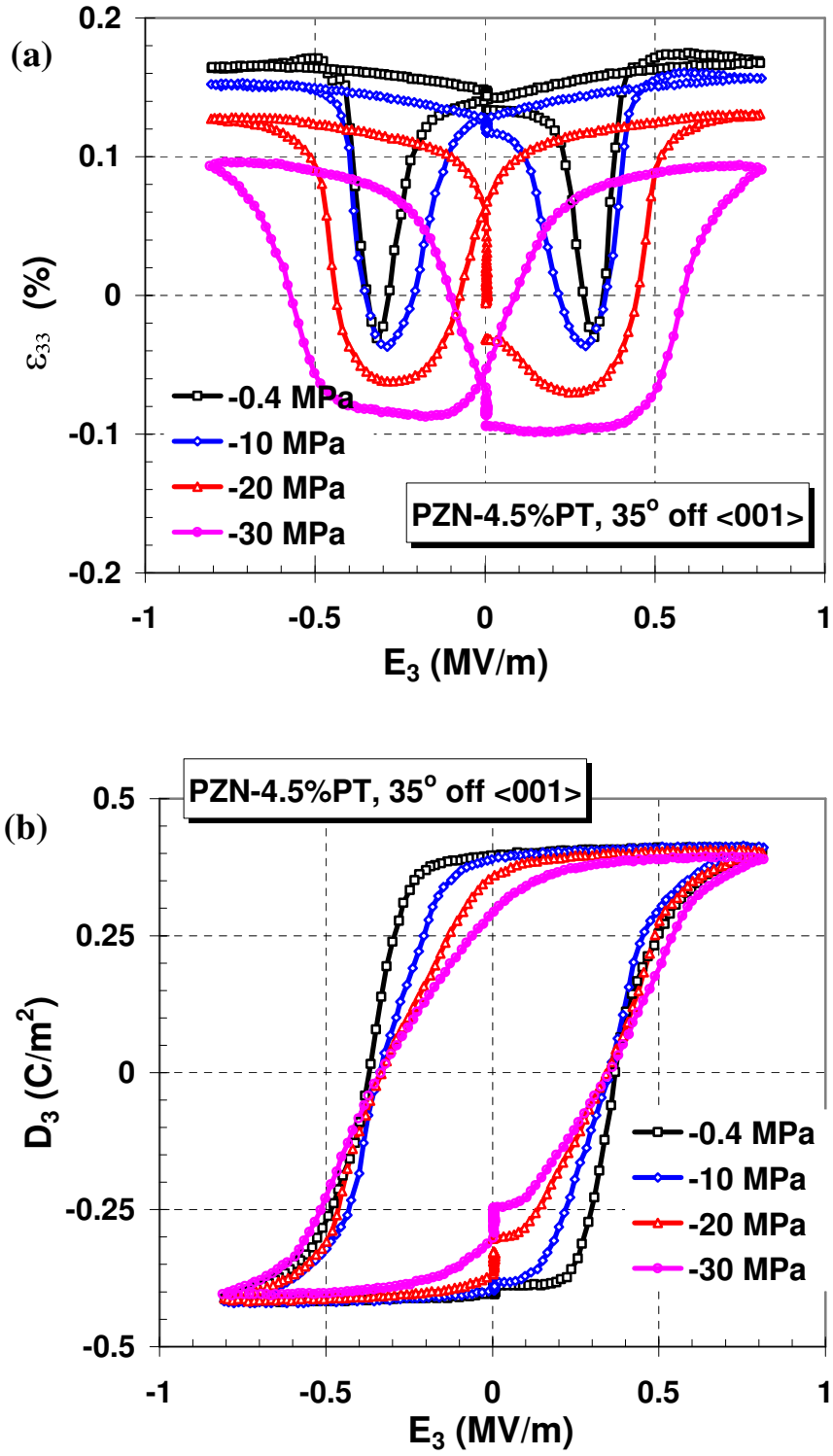

Figure 7-8. The 35° specimen under stress and electric field loading. (a) Strain vs. electric field; (b) Electric displacement vs. electric field; (c) Stress vs. strain; (d) Stress vs. electric displacement.

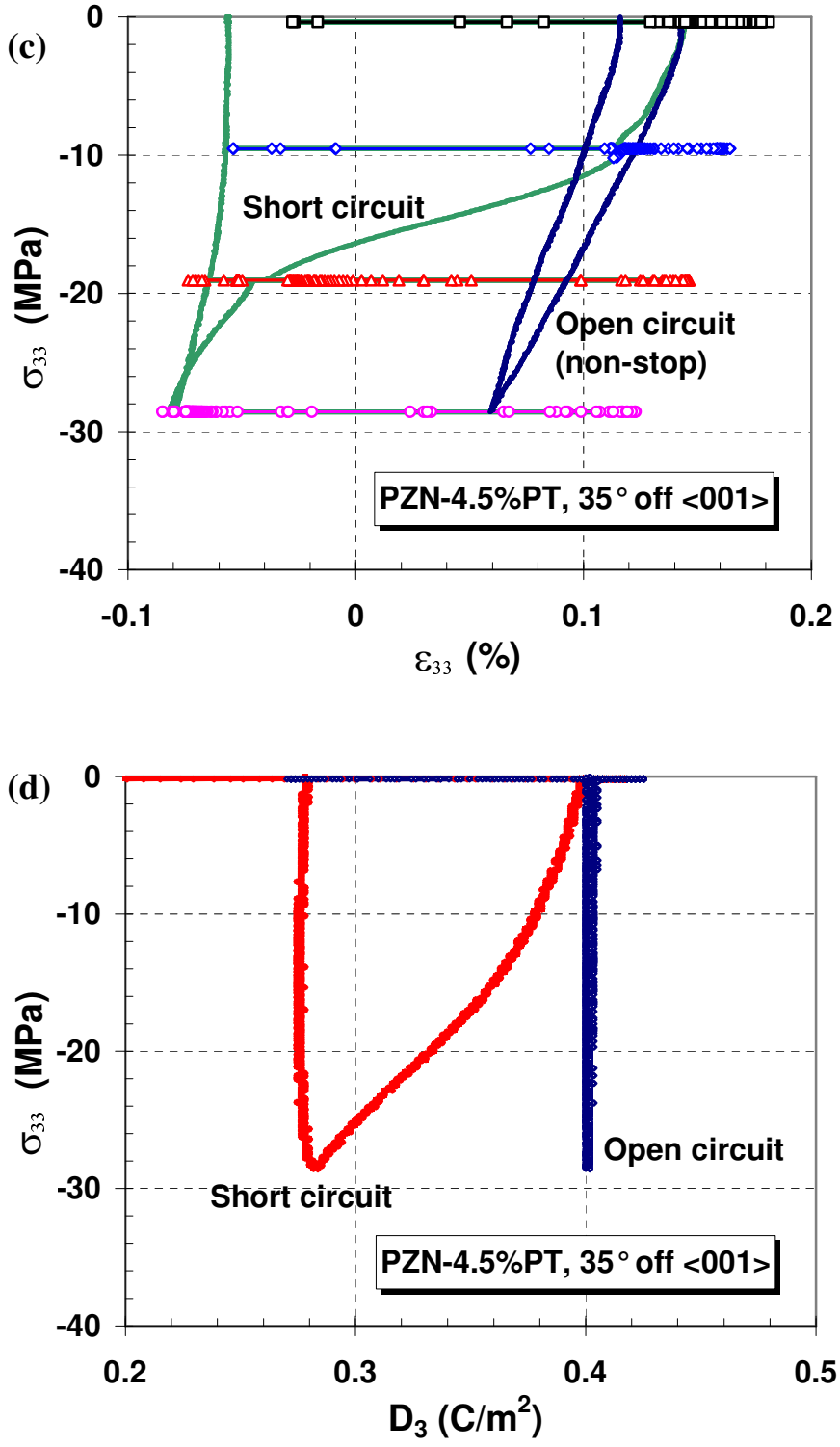

Figure 7-8 (continued).

The 35° sample displays significant offset of strain and electric displacement after a stress cycle under short circuit condition. The large remanent strain induced by polarization was reduced to a negative value, and the remanent electric displacement was reduced from 0.4 C/m^2 to 0.22 C/m^2. These reflect a strong stress induced depolarization. In open circuit case there is almost no depolarization, and the stress-strain response is close to linear. The compliance from unloading data for short circuit condition and open circuit condition are about the same and hold constant during unloading. That implies the crystal remains in R phase during the test, and the nonlinear response in short circuit condition is from depolarization, not from phase change. Note that for the 35° orientation cut, there are two directions of spontaneous polarization at about 90° to the poling direction. These domains directions will facilitate the depolarization and reorientation instead of a phase change.

Figure 7-9 is a plot of the coercive field as a function of orientation and stress. The coercive field increases with increasing orientation angle except for one data point of the 25° sample at -0.4 MPa. It decreases with increasing pre-stress, approaching a stable value above 20 MPa of compressive stress. Note that the coercive field in polarization reversal at -0.4 MPa decreases a little bit from its initial value for the 10° specimen, while increases a lot for both the 25° and 35° specimens.

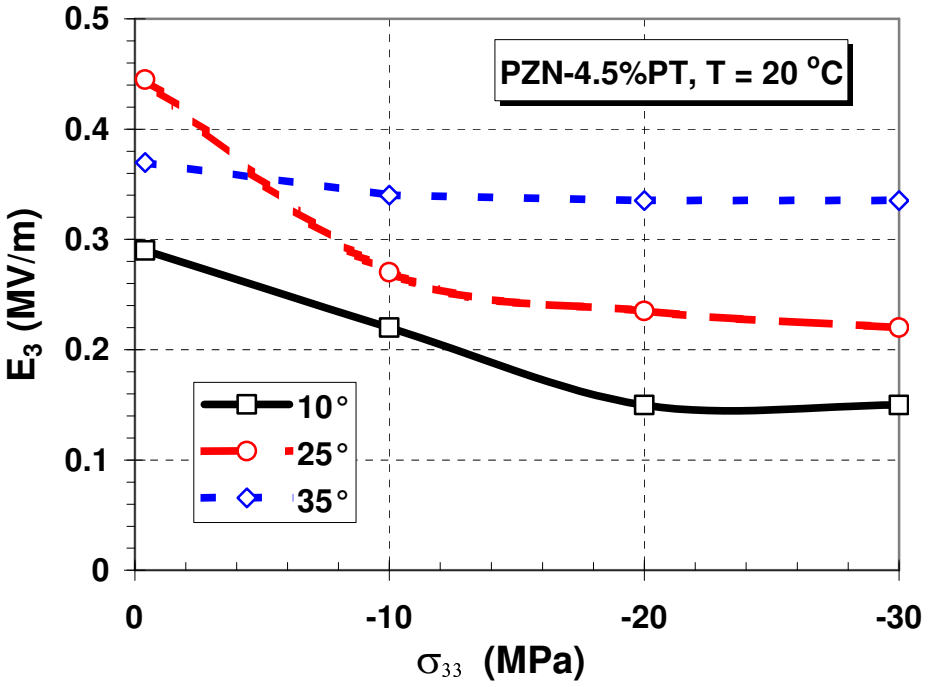

Figure 7-9. Coercive field as a function of orientation and stress.

7.6 Switching and Phase Stability

7.6.1 Stress Effect

Application of stress greatly affects polarization switching and phase transformation in the PZN-xPT and PMN-xPT single crystals. In the experiments depolarization was observed under compressive stress. The stress tends toward reducing the remnant strain in the loading direction. A compressive stress in a direction with positive remnant strain (normally in the poling direction) will hinder the polarization and induce depolarization through 71° or 109° switching, while a compressive stress in a direction of negative remnant strain will stabilize the poling state. Application of stress along different orientations shows different effects on the switching and phase stability.

In the absence of stress, both the <001> poling state and the <110> poling state of the rhombohedral crystals are very stable, and their polarization switching completes in a short range of electric field (almost instantaneously) [52]. If we consider the switching of the R-phase crystal variants for these two orientations, effectively there is only one kind of switching for either case, and the switching of a crystal variant is most likely a 180° switching, which does not induce a change of remnant strain. In <001> and <110> orientations good strain compatibility between equivalent-state domains reduces the driving force for domain wall motion thus the material behavior is linear with very little hysteresis at small to intermediate field levels.

Experimental investigation demonstrated that the high electromechanical performance of <001>-oriented rhombohedral crystals is relatively independent of compressive stress [77,162]. When there is no structural phase change, the rhombohedral crystal variants give cubic-symmetric mechanical properties: the mechanical properties of the rhombohedral domain are equivalent along the perpendicular <001>, <010> and <001> directions, and there is zero remnant strain for the <001> domain-engineered poling state. A stress in the poling direction has little effect in changing the poling state in order to reduce the remnant strain. Therefore theoretically a stress in <001> direction does not hinder or enforce the domain reorientation process of the rhombohedral crystals. In practice the <001> poled crystals show some degree of tetragonal symmetry due to a contribution of the engineered domain structure.

When the loading direction is with an angle off the <001> crystal orientation, polarization generates a positive remnant strain in the poling direction, thus a compressive stress in this direction will now act against the remnant strain and

polarization. As the orientation angle increases, the remnant strain also increases, leading to increasing depolarization and hysteresis under stress.

Application of stress could also lead to phase transitions such as the R-O phase change observed in the 10° specimen. The R-O phase change has been observed in both <001> and <110> PZN-xPT/PMN-xPT single crystals [52,122,163]. In these oriented PZN-4.5%PT crystals, a transformed orthorhombic phase can have spontaneous polarization perpendicular to the poling direction (parallel to the x_1 direction) showing a depolarized state. Generally the stress could induce both depolarization and phase change such as in the 25° specimen, making the behavior of the crystals complicated.

7.6.2 Open and Short Circuit Conditions

Shown in Figure 7-6d, 7-8c and 7-8d, the polarized crystals experienced stress loading under short circuit and open circuit conditions. Depolarization together with large strain change occurred in the short circuit case, while not much depolarization was observed in the open circuit case.

Short circuit condition means the electric field is held zero. In the open circuit condition the electric displacement is held constant. According to the piezoelectric constitutive relation, application of a compressive stress at open circuit condition effectively induces a positive electric field on the specimen (so that the electric displacement doesn't change). This induced electric field helps to stabilize the crystal from depolarization or phase change.

7.6.3 Rate Effect

Compared to 180° polarization switching and phase transitions with compatible domain structures as in <001> and <110> oriented crystals, depolarization and field induced phase transition show strong rate dependence due to rearrangement of domain structures. They also lead to deterioration of performance and cracking in the crystals. Response of the oriented PZN-4.5%PT crystals is also dependent of the electric field cycling frequency. As shown in Figure 7-10, the strain and electric displacement response are quasi-static when the field frequency is at or below 0.1 Hz. While at a frequency of 1.0 Hz, the apparent coercive field is much higher, the crystal was not fully polarized at E_{max} = 0.8 MV/m above this frequency. Comparably the 35° sample shows stronger rate effect than the 10° sample.

On the other hand, when the loading rate of stress increases from 0.2 MPa/s to 2 MPa/s, the stress-strain curves did not change much. Therefore we assume the stress loading speed is slow enough and the measurements reflect the quasi-static response of the crystals. According to the depolarization feature observed, rate effect can be expected when the speed of stress loading is higher, especially in the depolarization region.

Reapplication of electric fields cycles when stress was unloaded reflects good recovery of strain and electric displacement response, though cracks can be observed in these specimens after tests. The major cracks seem to be parallel to the poling direction, such that the specimens can still sustain the mechanical load. Arcing may occur due to these cracks.

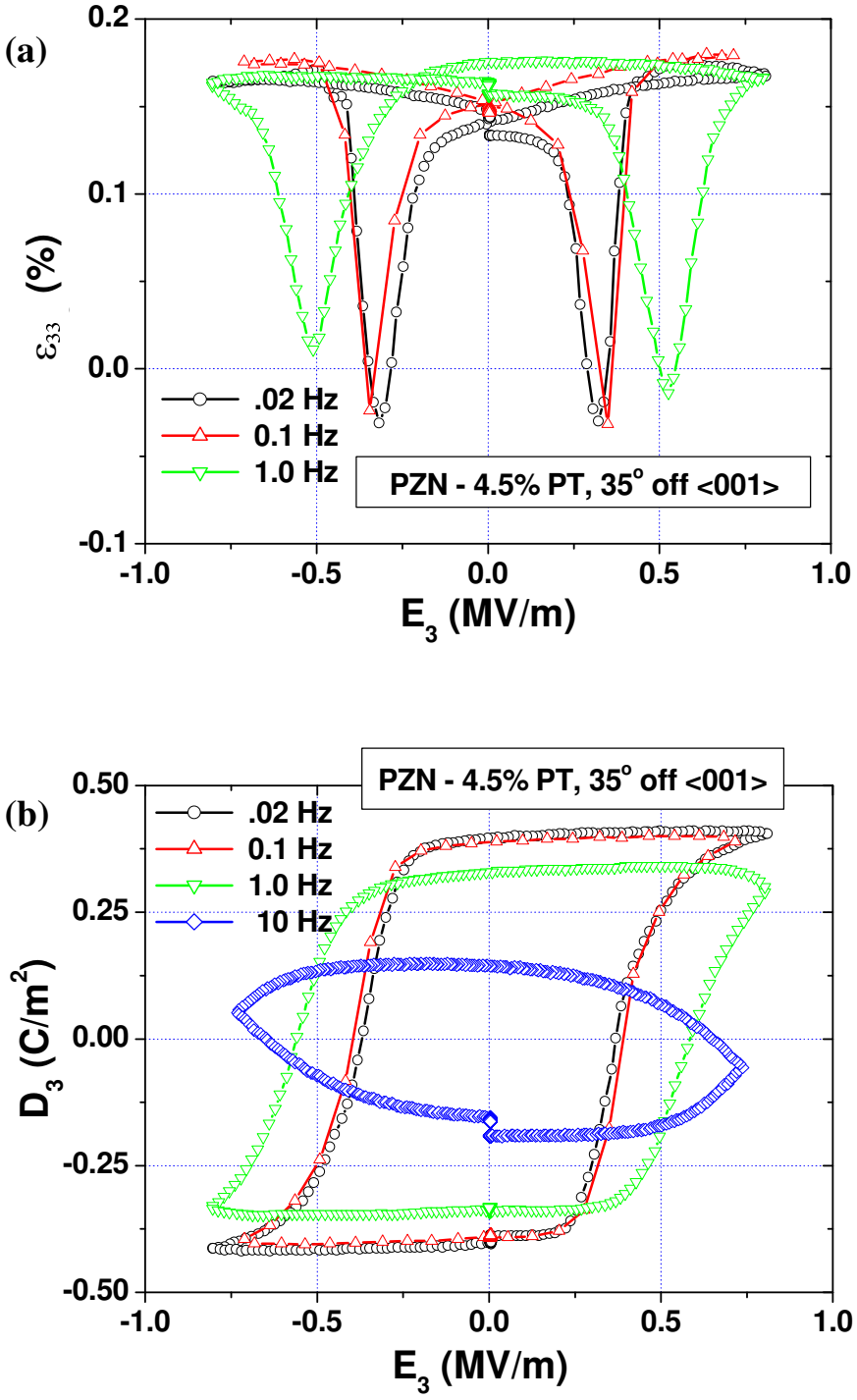

Figure 7-10. Electric field rate effect on the strain and electric displacement response. (a) Strain vs. electric field for the 35° specimen; (b) Electric displacement vs. electric field for the 35° specimen; (c) Electric displacement vs. electric field for the 10° specimen.

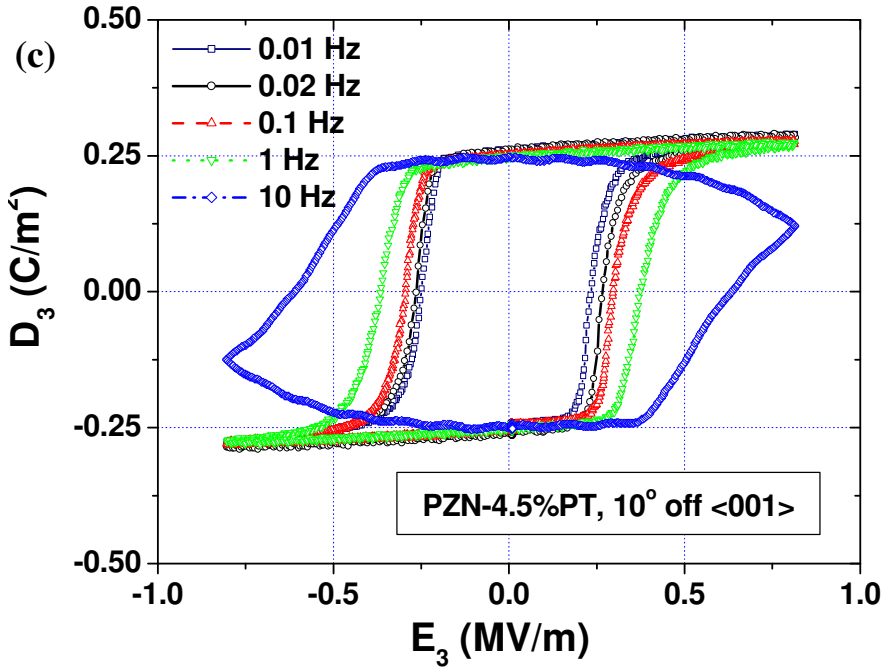

Figure 7-10 (continued).

7.7 Concluding Remarks

The electromechanical response of PZN-4.5%PT single crystals were experimentally investigated by applying compressive stress and electric field cycles in different crystal orientations between <001> and <111>. It was shown that the electromechanical response of the crystals exhibit strong orientation dependence. A <001>-oriented crystal offers a stable poling state and high piezoelectric coefficient (d_{33}). As the orientation of the crystal is rotated from <001> to <111>, the piezoelectric coefficient drops dramatically. Crystal variant volume fractions and piezoelectric coefficients were computed from remnant electric displacement for different orientations. The results were in good agreement with the experimental measurements except for the

abnormal behavior of the piezoelectric coefficients d_{31} and d_{32} for the 25° and 35° specimens. This may be related to domain interactions or multiphase coexistence.

Combined stress and electric field loading reveals complicated polarization switching and phase transition behavior. A compressive stress tends toward reducing the remnant strain in the loading direction through either depolarization or phase transitions. Stress induced depolarization can be observed in all orientation cuts. A rhombohedral-orthorhombic phase transition featuring depolarization was observed in the 10° specimen. Depolarization and phase transitions are dependent on electric boundary conditions. Short circuit condition eases, while open circuit resists depolarization and phase transitions. Field induced polarization and phase transition show strong rate dependence.

Domain interaction and incompatibility also lead to deterioration of performance and cracking in the crystals. Due to complicated field induced polarization reorientations and phase transitions in the relaxor ferroelectric crystals, further investigation is necessary in understanding the domain interaction mechanism behind the complex phenomena of oriented crystals.

CHAPTER 8

CRACK INITIATION AT ELECTRODE EDGES IN PZN-4.5%PT SINGLE CRYSTALS

Fringing electric fields emanating from an electrode edge in electro-mechanically coupled materials can potentially lead to cracking from a strain incompatibility of the active and inactive regions. Partial electrodes were studied in single crystal PZN-4.5%PT to characterize the fracture behavior near an electrode edge. Crack growth was characterized by varying the specimen thickness (t = 0.7 mm and 2 mm) and electrode coverage (50~95%). It is found that an electric field of 2 MV/m will initiate cracks in the 2 mm thick specimens, while an electric field of 3 MV/m was required to initiate cracks in the 0.7 mm specimens. Linear piezoelectric finite element analysis was carried out to determine the field quantities near the electrode edge and evaluate the internal energy density. A paper of this work has been accepted for publication in the *Journal of Intelligent Material Systems and Structures*.

8.1 Introduction

Piezoelectric PZN-4.5%PT single crystals are under development for high strain piezoelectric actuators and sensors. The <001> oriented and poled rhombohedral crystals possess a high electromechanical coupling factor (k_{33} > 90%) and large piezoelectric constants (d_{33} > 2500 pC/N) [8,10,18,44,59,113,129]. The large electromechanical response offers the potential for substantial improvements over ceramic

electromechanical transducers and actuators. Under large electric field the <001> crystals also exhibit rhombohedral to tetragonal phase transition behavior [36,67].

Ceramic multilayer actuators are often designed with the electrode edge ending inside the ferroelectric material in order to simplify design and reduce manufacturing costs. In such case when the material is poled, a strain incompatibility arises from complex domain reorientation near the electrode edge. A stress gradient forms, often leading to cracking and device failure upon repeated electrical cycling. There are manufacturing advantages to using simple electrode patterns for stack actuators, but the fracture behavior of single crystals needs to be understood before design this type of multilayer single crystal actuator.

Investigations of the damage mechanisms in ceramic multilayer actuators have been studied in detail. Lucato *et al.* [109] characterized and modeled cracks forming in partially electroded lead zirconate titanate (PZT) specimens. It was shown that cracks can form perpendicular to the electrode edge. Other studies [164-166] have shown that cracks can form preferentially from the electrode edge. An analytic approach was developed by Suo [167] who showed that a stress gradient forms near an electrode edge from nonlinear domain reorientation under an applied electric field. Later works by Hao, Gong, and Suo [168] and Gong and Suo [169] used nonlinear finite element modeling to determine stress intensity factors for a multilayer actuator under electric field loading.

This work focuses on characterizing and modeling the behavior of PZN-4.5%PT single crystals under electric fields near the edge of an electrode. The rhombohedral crystals were cut and poled in the <001> direction with partial electrodes. The specimen geometry and electrode coverage were varied and the fracture behavior was observed. A

linear piezoelectric finite element model was used to evaluate the field quantities near the electrode edge.

8.2 Experiments and Modeling Procedure

Listed in Table 8-1, ten partially electroded PZN-4.5%PT single crystals received from TRS Technologies, Inc. were used for the characterization. The specimens were initially in an unpolarized state. The surfaces of the specimens were not polished. For each specimen, refer to Figure 8-1, the top surface was covered by a partial electrode; the bottom side was 100% covered with electrode. All ten specimens were subjected to unipolar cyclic electric fields (in $+x_3$ direction) at a frequency of 0.5Hz. The crack growth was monitored and recorded using an optical microscope and VCR. These experiments were conducted by Dr. Shan Wan.

Table 8-1. <001>-oriented PZN-4.5%PT specimens with partial electrodes.

Specimen#	Geometry $X_1 \times X_2 \times X_3$ (mm)	Electrode covering fraction
P1	5.184×4.302×0.759	95%
P2	5.317×4.144×0.717	90%
P3	5.299×4.280×0.770	70%
P4	4.931×4.181×0.739	60%
P5	5.112×4.228×0.721	50%
P6	5.165×4.192×2.015	95%
P7	5.181×4.108×2.027	90%
P8	5.063×4.342×2.019	70%
P9	5.086×3.871×2.026	60%
P10	5.122×3.781×2.018	50%

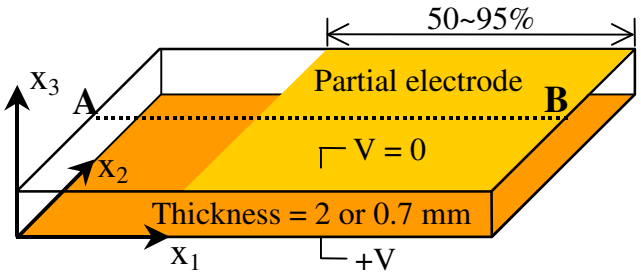

Figure 8-1. Illustration of a partially electroded PZN-4.5%PT specimen.

A computational model was developed to compute the stress and electric field distributions using the multi-physics module of FEMLAB 2.3. Only the linear piezoelectric effect was considered. Figure 8-1 also represents the three-dimensional finite element model geometry. The partial electrode (top-shaded region) was grounded and a positive voltage was applied to the bottom electrode. Free body movement and rotation are constrained. The line AB was the path along which electric field, stress and energy density were later plotted.

In the computation the region of the material covered with an electrode is assumed to be poled in x_3 direction, while the uncovered part is unpoled. The electrode covered part was assigned to have piezoelectric coefficients of <001> poled PZN-4.5%PT single crystals, and the uncovered part was assumed to have no piezoelectric effect. This was implemented to model a worst case scenario of the active and inactive regions. This approach overestimates the strain incompatibility. A rhombohedral domain has a spontaneous polarization in a <111> direction. The unpoled crystals have a cubic symmetry. For the <001> poled rhombohedral crystal, a contribution from the engineered domain pattern may lead to a tetragonal symmetry with different coefficients along the

poling direction. But the anisotropy is small. Rather, electric boundary conditions have a much larger effect on the material coefficients, and not all of the coefficients have been measured experimentally. Here the elastic and dielectric material coefficients were approximated as isotropic and the same for the poled and unpoled regions. With these assumptions the strain incompatibility will be purely due to the linear piezoelectric effect. The properties are given in Table 8-2. Different thickness and electrode percent coverage are considered in the computations. Mesh refinement near the electrode edge was utilized during each simulation to ensure proper convergence.

Table 8-2. Material properties of the PZN-4.5%PT used in the finite element model (Refer to [44]).

	Unpoled region	Poled region
E [GPa]	10	10
ν (Poisson's ratio)	0.4	0.4
K (relative permittivity)	2000	2000
e_{33} [C/m^2]	0	15
e_{31} [C/m^2]	0	-3.7
e_{15} [C/m^2]	0	8.9

8.3 Results and Discussion

8.3.1 Cracking Behavior

Experimental results show that Crack formation is strongly dependent on the electric field magnitude, electrode covering fraction, and specimen thickness. The 2 mm specimens were more prone to cracking than the 0.7 mm thick specimens. The amount of cracking increased as the amount of electrode coverage decreased.

The 0.7 mm specimens were more resistive to crack propagation under high electric field. No apparent cracking was observed in any of the 0.7 mm thick single crystal specimens when the electric field was cycled between 0~2 MV/m. These specimens fractured when the electric field was increased to 3 MV/m, horizontal cracking in the x_1 direction was induced, as shown in Figure 8-2a~d. The bright regions in the images (right sides) are the electroded part of the surfaces. No cracking was found in x_2 or x_3 direction in 0.7 mm thin specimens.

Cracking usually took place abruptly within 50 cycles. Cracks rapidly reach saturated length after a few more cycles. Therefore no stable fatigue crack growth was observed. As shown in Figure 8-2a~d, most long cracks were found in the polarized part of the crystals covered by electrodes. In the unpolarized region with no electrode, cracks were observed with shorter length. The saturated crack lengths in the polarized and unpolarized regions decreased with increasing electrode covering fraction, as shown in Figure 8-2e. At 95% coverage, the 0.7 mm specimens exhibited no cracking under a 3 MV/m electric field cycling.

The 2 mm thick specimens resulted in cracking for all cases when an electric field of 2 MV/m was applied. In addition to cracking in the x_1 direction, cracks in the x_2 and x_3 directions were also observed in the specimens with 50% and 60% electrode coverage. These can be seen in Figure 8-3a~c. Similar to the 0.7 mm specimens, the horizontal crack lengths decreased with increasing electrode coverage, as shown in Figure 8-3d. The lengths of the cracks in x_2 and x_3 directions were difficult to quantify.

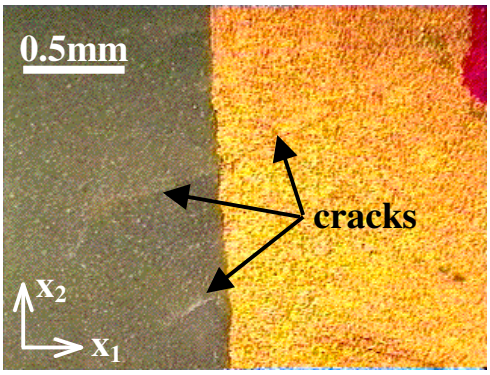

(a) 50% electrode

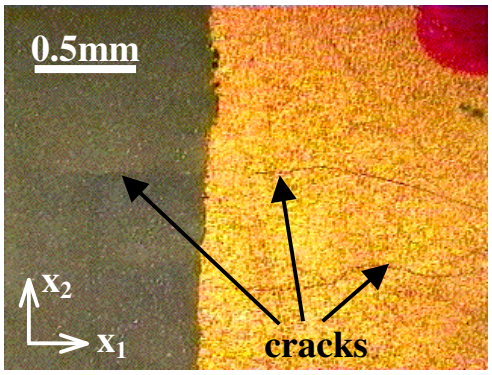

(b) 60% electrode

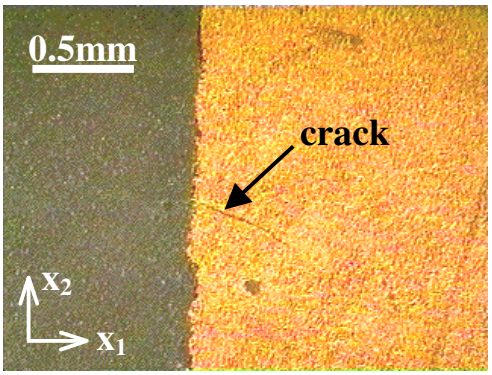

(c) 70% electrode

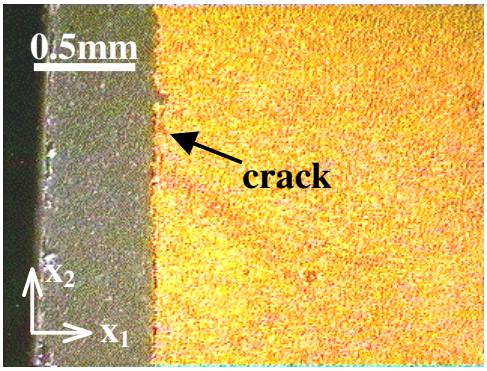

(d) 90% electrode

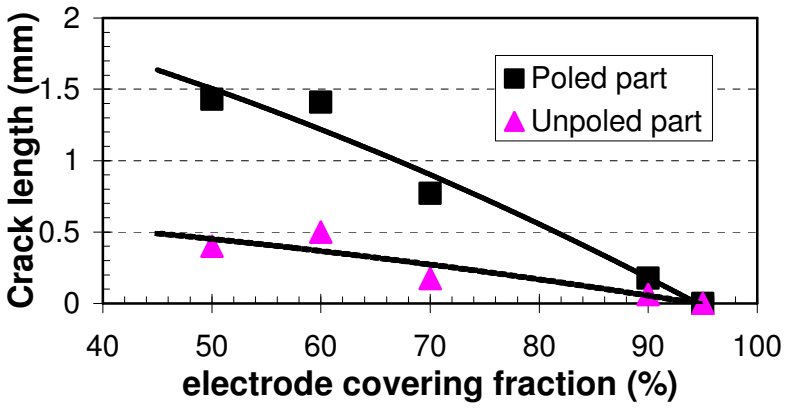

(e)

Figure 8-2. Horizontal cracks (x_1 direction) in four 0.7 mm thick PZN-4.5PT crystals driven by 3 MV/m unipolar cyclic electric field. (a~d) Various cracks in the partially electroded crystals (there was no cracking in the 95% electroded specimen); (e) Saturated crack length in x_1 direction.

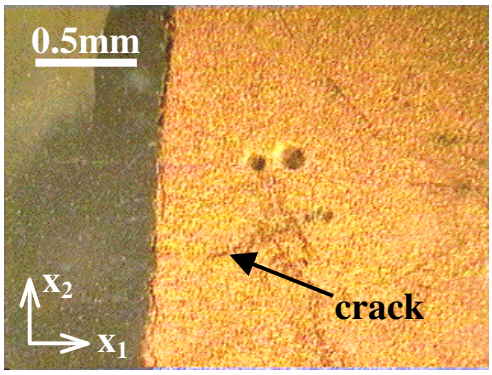

(a) Horizontal cracks in x_1 direction

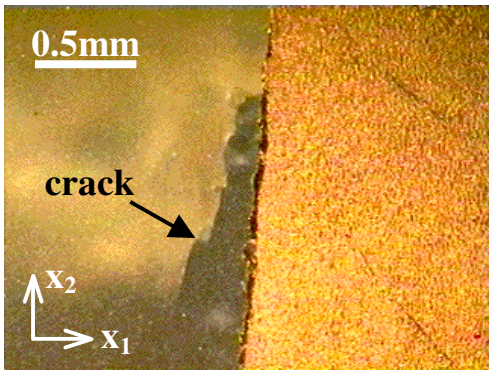

(b) Damage in crystal interior

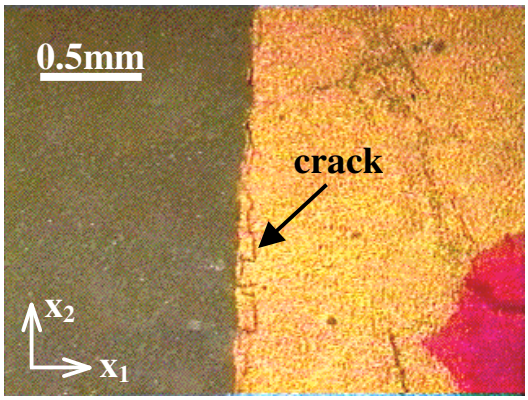

(c) Vertical cracks in x_2 direction

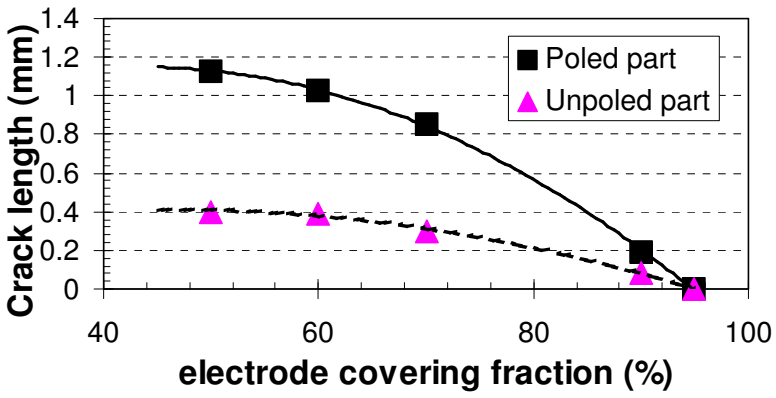

(d)

Figure 8-3. Cracks in 2 mm thick PZN-4.5PT crystals driven by 2 MV/m unipolar cyclic electric field. (a~c) Various cracks in the 50% partially electroded; (d) Saturated crack length in x_1 direction.

8.3.2 Finite Element Analysis

The geometry shown in Figure 8-1 was used in finite element modeling to compute the field quantities near the electrode edge as a function of specimen thickness and electrode coverage. Under an applied voltage, an electric field singularity exists at the electrode edge, as shown in Figure 8-4a. A stress concentration was also determined to exist at the electrode edge. The stress component in the x_2 direction (σ_{22}) is shown in Figure 8-4b. The solution shows a compressive region outside of the electrode followed by a region of tension underneath the electrode. A similar stress concentration was found in σ_{11}.

Finite element solutions of the electric field, stress σ_{22} and strain energy density along path AB (shown in Figure 8-1) for different electrode coverage and for different specimen thickness were plotted in Figure 8-5 and Figure 8-6, respectively. The finite element solution was used to calculate the variation of internal energy density along the line AB. The computation predicts a concentration at the electrode edge. The electrical energy density has a similar functional form, approximately an order larger than the elastic component. The finite element simulations show that the strain energy density increases when the electrode coverage is reduced (Figure 8-5c) or when the specimen thickness is increased (Figure 8-6c).

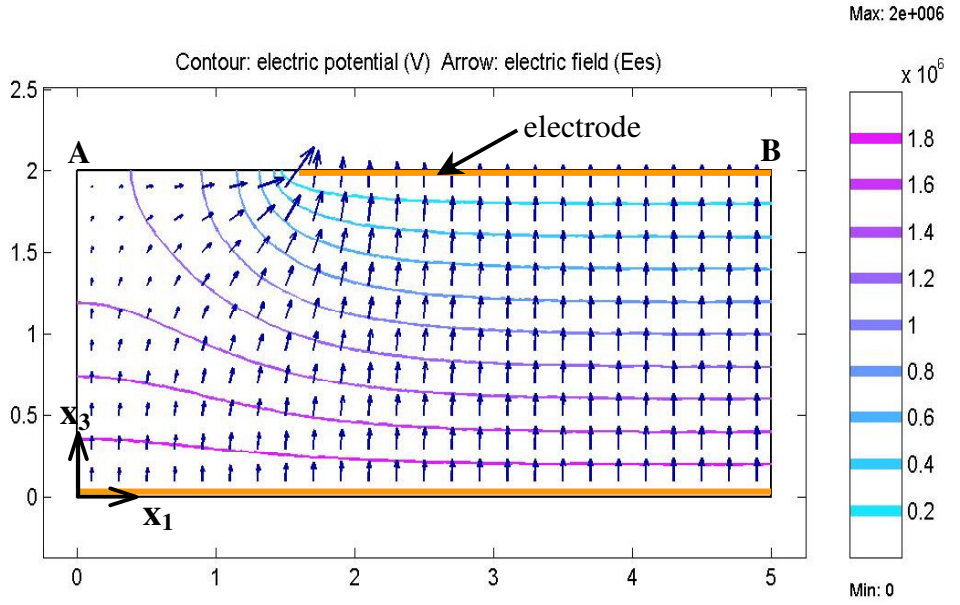

(a)

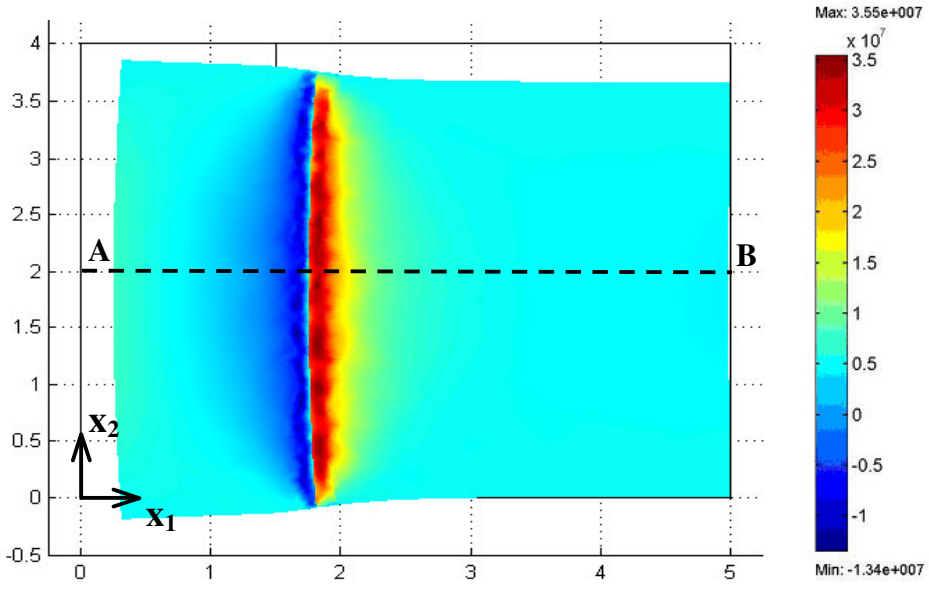

(b)

Figure 8-4. Finite element analysis of a 70% electroded 2 mm thick crystal under electric field. (a) Electric potential and electric field distribution in the x_1-x_3 plane sliced along path AB; (b) Deformation and stress component σ_{22} of the top surface (plot of x_1-x_2 plane).

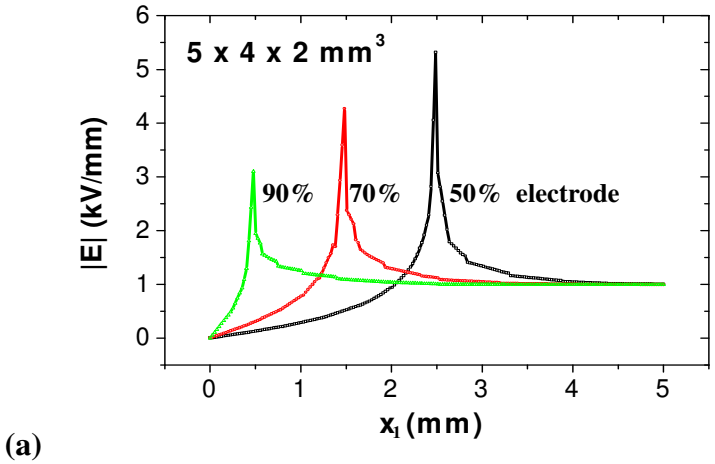

(a)

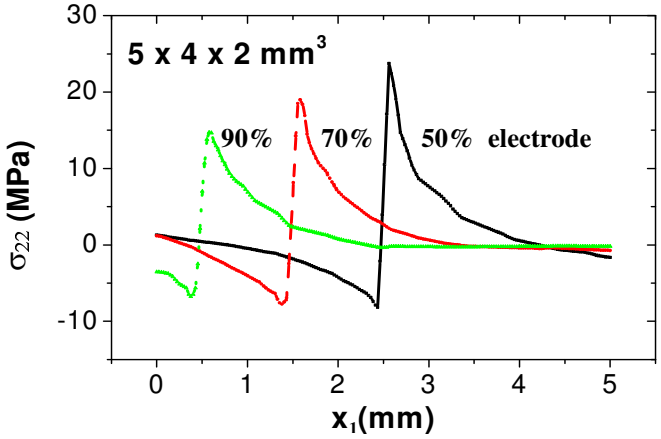

(b)

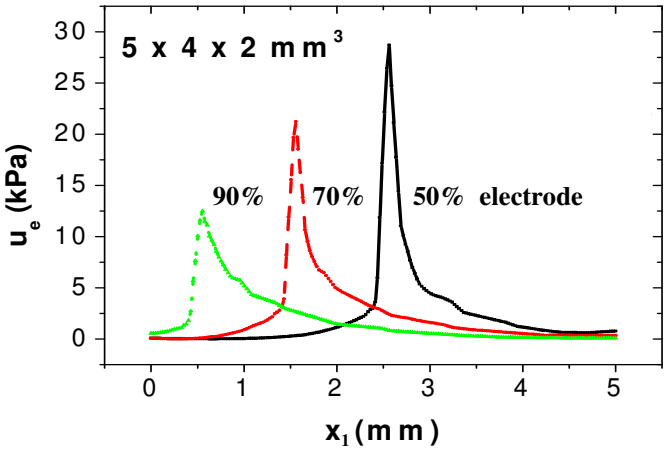

(c)

Figure 8-5. Finite element analysis of the electric field, stress and strain energy density along path AB for 2 mm thickness and different electrode coverage. (a) Electric field magnitude; (b) Stress component σ_{22}; (c) Strain energy density.

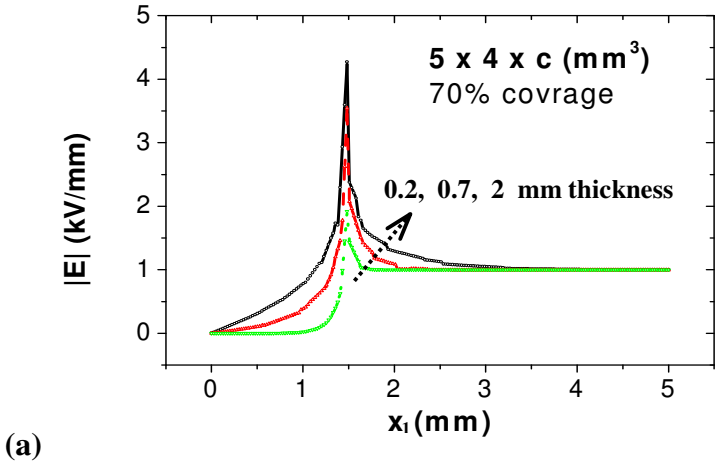

(a)

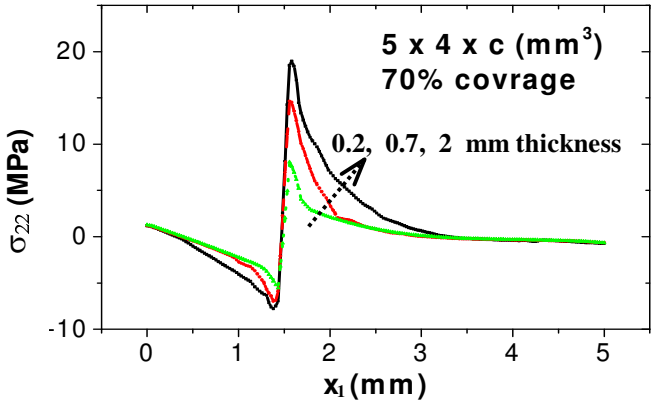

(b)

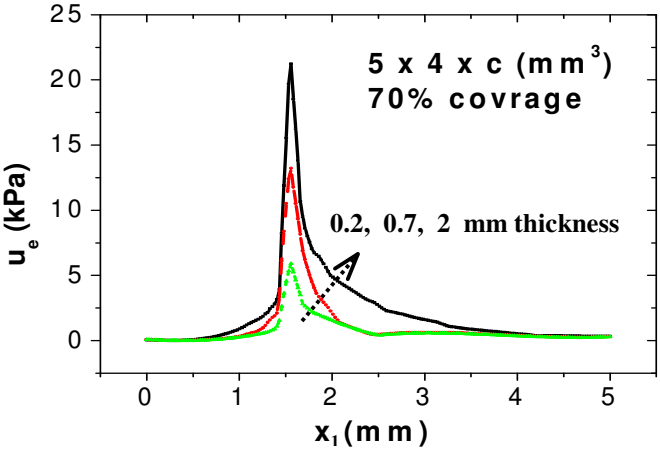

(c)

Figure 8-6. Finite element analysis of the electric field, stress and strain energy density along path AB for 70% electrode coverage and different specimen thickness. (a) Electric field magnitude; (b) Stress component σ_{22}; (c) Strain energy density.

8.3.3 Fracture Mechanism

The electric field induced cracking in partially electroded specimens is due to non-uniform deformation in the crystals. Near the electrode edge, see Figure 8-4a, a fringing electric field develops from the finite length of the top electrode. The fringing field is highly concentrated at the electrode edge, which creates a region of large internal energy density. Internal energy density can be reduced by domain reorientation, phase transformations, or crack propagation.

PZN-4.5%PT is in cubic phase above the Curie temperature and becomes rhombohedral at room temperature. In the unpoled state, single crystal PZN-4.5%PT consists of eight randomly oriented rhombohedral crystal variants. When a large electric field was applied in a <001> direction, the crystal variants rotate into four of the eight variants to partially align with the applied field, forming a pseudo-tetragonal structure in the region underneath the electrode. After this polarization, large piezoelectric response is expected for applied electric fields below 3 MV/m. The fringing fields near the electrode edge will force some of the crystal variants to rotate to align with the non-uniform field (see Figure 8-4a). Complex domain reorientation and different crystal phases can be expected to be present in this region. A microstructural incompatibility may therefore develop, potentially leading to crack formation.

The linear finite element model predicts a concentration of electric field and stress focused at the electrode edge. The stress concentration is enhanced by the inhomogeneous piezoelectric properties used in the simulation from Table 8-1. This was used as a worst case scenario for modeling the active and inactive regions excited by the

electric field. Near the electrode edge, the model predicts large tensile stresses on the side containing the electrode. On the opposing side, the material is under compressive stress. This correlates with the fracture behavior where longer cracks were observed under the electrode.

The driving force for crack propagation is proportional to the reduction of strain energy associated with the introduction of a crack. The thinner specimens with the largest area fraction of electrode coverage have the smallest volume of material affected by the strain incompatibility and thus the least amount of strain energy to be released upon introduction of a crack. Figure 8-5c and Figure 8-6c illustrate how the strain energy depends on electrode coverage and specimen thickness. The results suggest that it may be possible to partially electrode thin wafers and stack them without inducing cracking. This may lead to an alternative stack manufacturing technique.

8.4 Concluding Remarks

Single crystal PZN-4.5%PT was characterized under non-uniform electric fields emanating from a partial electrode. The electric field magnitude, specimen thickness and electrode coverage were shown to significantly affect the fracture behavior. A specimen with a thickness of 0.7 mm was less prone to cracking than a 2 mm specimen. All the 2 mm specimens formed cracks under a uni-polar 2 MV/m electric field, while no cracking was observed in the 0.7 mm specimens under the same electric field. A 3 MV/m electric field induces cracks in the 0.7 mm specimens except for the one with 95% electrode coverage.

Linear piezoelectric finite element modeling supported the observed behavior. An electric field singularity occurs at the electrode edge. Stress concentrations were computed in this region assuming an interface between piezoelectric and non-piezoelectric parts separated at the electrode edge. A concentration of internal energy density was determined which may provide the driving force for crack propagation.

The actual boundary conditions for a piezoelectric layer in stack actuators may be different from the experiments and the computation model due to the constraints between layers. Furthermore, real materials will exhibit difference in the severity of field singularity at the electrode edge. Domain reorientation and phase transformations will occur near the electrode edge to minimize the internal energy. This may give difference in strain and charge incompatibilities that drive crack nucleation and growth.

Acknowledgement

The author would like to thank Dr. Shan Wan for conducting the experimental measurements in this chapter.

CHAPTER 9

MAJOR CONCLUSIONS

The polarization switching and phase transition behavior of relaxor ferroelectric PZN-4.5%PT, PMN-32%PT single crystals were investigated by a combination of experimental and theoretical modeling methods. Crystals at different orientation cuts were investigated under different temperature, electric field and stress loadings. It was found that these crystals show strong orientation dependence of electromechanical properties, and applied temperature, stress and electric field all affect their poling and phase states. Depolarization, rate dependence and fracture behavior of these crystals under external fields have been measured and analyzed. In the following sections the major contributions of this research are summarized, the limitations of this work and prospect of future research are discussed.

9.1 Contributions

Crystal orientation is critical to the performance of the relaxor ferroelectric single crystals. A favorable <110> orientation for rhombohedral relaxor single crystals has been identified and characterized. When the rhombohedral crystals are polarized along this orientation, stable multi-domain structures are formed, leading to superior electromechanical properties including high piezoelectric coefficients, excellent linearity and fatigue resistance. At the same time relaxor single crystals may exist in different phases or a coexistence of multiple phases. In order to achieve the benefits of the multi-

domain structures of the <001> or <110> oriented relaxor single crystals, they should be retained in the rhombohedral phase.

Based on experimental measurements, crystal variant based models were developed to compute the physical properties of multi-domain crystals at different orientation cuts from a set of properties for the single domain. This mesoscale modeling matches experimental data very well, showing that it is suitable for the analysis and computation of multi-domain structures in ferroelectric single crystals.

External fields, including temperature, stress and electric field, all strongly affect the poling and phase states of the relaxor single crystals. Therefore it is important to identify the allowable loading and temperature ranges for applications. The R-O phase transition was observed in both PZN-4.5%PT and PMN-32%PT single crystals under <110> electric field. Applied stress, electric field and temperature on the <110> PMN-32%PT single crystals were found to cooperatively contribute to the phase transition. The phase transition criterion was obtained in form of linear equations of applied electric field, stress and temperature. These results are useful for the design of high performance actuators and transducers. Multiple phase transitions in <001> oriented PMN-32%PT single crystals were also observed and their occurrence as functions of applied electric field, stress and temperature was measured.

Experimental measurements provided data for thermodynamics analysis of the polarization switching and phase transitions of relaxor ferroelectric single crystals. Work-energy analysis of the R-O phase transition processes in both PZN-4.5%PT and PMN-32%PT single crystals showed that at a given temperature the phase transformation begins at a critical level of internal energy density and ends at a second critical level. A

second criterion, minimization of the Gibbs free energy, determines whether the transformation will take place. The critical energy levels were found to be independent of the combinations of stress and electric field that induced them. This work-energy analysis of field induced phase transitions sheds light on the mechanism of structural phase transitions of ferroelectric single crystals. It leads to energy based phase transition criteria, which are not only essential for theoretical modeling and numerical simulations, but also desirable for directing experimental investigations. They enable the rapid characterization of the structural phase transformation behavior of relaxor single crystals over a range of compositions and temperatures.

9.2 Prospect

The results of this research provide an improved understanding of field induced polarization switching and phase transition behavior of relaxor ferroelectric crystals. The crystal variant modeling and thermodynamics analysis give theoretical insight and numerical capability for future research and applications of ferroelectric materials. By including polarization switching and phase transition criteria, the crystal variant modeling leads to a mesoscale constitutive model for the nonlinear behavior of ferroelectric crystals. Such a model can be implemented in finite element codes to simulate, predict and design engineered multi-domain ferroelectric materials.

The electromechanical properties of different ferroelectric phases in relaxor single crystals associated with different spontaneous polarization directions are much different. When the compositions of the crystals are close to the MPB, they show higher electromechanical properties. But the crystals around the MPB are prone to phase

transitions and domain instability, which leads to increasing variance and non-linearity of these properties. Increasing domain and phase complexity also causes challenges in crystal variant modeling as well as reliability problems such as hysteresis loss, fracture and fatigue.

In the <001> and <110> crystal cuts the domain walls are very stable. This means there is little or no ferroelectric or ferroelastic polarization reorientation. In other crystal cuts there is domain wall motion under applied stress and electric fields. This gives rise to minor hysteresis loops and associated energy dissipation under applied fields. Energy analysis must distinguish between energy barriers to transformations and dissipative energy during the highly rate dependent and irreversible process of domain wall motion.

Piezoelectric and ferroelectric materials display electromechanically coupling and temperature dependent multi-physics behavior. In observation, measurements, modeling and simulation of these materials, multi-scale methods from quantum mechanics, molecular dynamics to macroscopic material properties measurement and structure performance analysis may be performed. Along with the improvement of single crystal growing techniques, better understanding of the polarization switching and phase transition mechanism will foster the applications of ferroelectric single crystals in sensing and actuating devices.

REFERENCES

1. Haertling, G. H. Ferroelectric ceramics: history and technology. *J. Am. Ceram. Soc.* **82**, 797-818 (1999).

2. Mason, W. P. Piezoelectricity, its history and applications. *J. Acoust. Soc. Am.* **70**, 1561-1566 (1981).

3. Ballato, A. Piezoelectricity: History and new thrusts. *Proceedings of the IEEE Ultrasonics Symposium* **1**, 575-583 (1996).

4. Dabkowski, A., Dabkowska, H. A., Greedan, J. E., Ren, W. & Mukherjee, B. K. Growth and properties of single crystals of relaxor PZN-PT materials obtained from high-temperature solution. *J. Cryst. Growth* **265**, 204-213 (2004).

5. Chen, Q. X. & Payne, P. A. Industrial applications of piezoelectric polymer transducers. *Meas. Sci. Technol.* **6**, 249-267 (1995).

6. Xu, Y. *Ferroelectric Materials and Their Applications*. North-Holland Elsevier Sci. Publ., Amsterdam (1991).

7. Smolenskii, G. A. Physical Phenomena in Ferroelectrics with Diffused Phase Transition. *J. Phys. Soc. Jpn. (Suppl.)* **28**, 26-37 (1970).

8. Park, S. E. & Shrout, T. R. Ultrahigh strain and piezoelectric behavior in relaxor based ferroelectric single crystals. *J. Appl. Phys.* **82**, 1804-1811 (1997).

9. Kuwata, J., Uchino, K. & Nomura, S. Phase transitions in the $Pb(Zn_{1/3}Nb_{2/3})O_3$-$PbTiO_3$ system. *Ferroelectrics* **37**, 579-582 (1981).

10. Park, S. E. & Shrout, T. R. Characteristics of relaxor-based piezoelectric single crystals for ultrasonic transducers. *IEEE T. Ultrason. Ferr.* **44**, 1140-1147 (1997).

11. Fan, H., Zhao, L., Tang, B., Tian, C. & Kim, H. E. Growth and characterization of PMNT relaxor-based ferroelectric single crystals by flux method. *Mat. Sci. Eng. B* **99**, 183-186 (2003).

12. Chen, W. & Ye, Z.-G. Top seeded solution growth and characterization of piezo-/ferroelectric $(1-x)Pb(Zn_{1/3}Nb_{2/3})O_3$-$xPbTiO_3$ single crystals. *J. Cryst. Growth* **233**, 503-511 (2001).

13. Fang, B. J., Xu, H. Q., He, T. H., Luo, H. S. & Yin, Z. W. Growth mechanism and electrical properties of $Pb[(Zn_{1/3}Nb_{2/3})_{0.91}Ti_{0.09}]O_3$ single crystals by a modified Bridgman method. *J. Cryst. Growth* **244**, 318-326 (2002).

14. Luo, H., Xu, G., Xu, H., Wang, P. & Yin, Z. Compositional homogeneity and electrical properties of lead magnesium niobate titanate single crystals grown by a modified Bridgman technique. *Jpn. J. Appl. Phys. Part 1* **39**, 5581-5585 (2000).

15. Messing, G. L., Sabolsky, E. M., Kwon, S. & Trolier-McKinstry, S. Templated grain growth of textured piezoelectric ceramics. *Euro Ceramics Vii, Pt 1-3* **206-2**, 1293-1296 (2002).

16. Sabolsky, E. M., Trolier-McKinstry, S. & Messing, G. L. Dielectric and piezoelectric properties of <001> fiber-textured $0.675Pb(Mg_{1/3}Nb_{2/3})O_3$-$0.325PbTiO_3$ ceramics. *J. Appl. Phys.* **93**, 4072-4080 (2003).

17. Park, S. E. E. & Hackenberger, W. High performance single crystal piezoelectrics: applications and issues. *Curr. Opin. Solid State Mater. Sci.* **6**, 11-18 (2002).

18. Kuwata, J., Uchino, K. & Nomura, S. Dielectric and piezoelectric properties of $0.91Pb(Zn_{1/3}Nb_{2/3})O_3$-$0.09PbTiO_3$ single crystals. *Jpn. J. Appl. Phys. Part 1* **21**, 1298-1302 (1982).

19. Uchino, K. High electromechanical coupling piezoelectrics: relaxor and normal ferroelectric solid solutions. *Solid State Ionics* **108**, 43-52 (1998).

20. Lopath, P. D., Park, S. E., Shung, K. K., & Shrout, T. R. Ultrasonic transducers using piezoelectric single crystal perovskite. *IEEE International Symposium on Applications of Ferroelectrics* **2**, 543-546 (1996).

21. Hackenberger, W., Rehrig, P. W., Ritter, T., & Shrout, T. Advanced piezoelectric materials for medical ultrasound transducers. *IEEE Ultrasonics Symposium.* **2**, 1101-1104 (2001).

22. Damjanovic, D. Piezoelectric properties of perovskite ferroelectrics: unsolved problems and future research. *Annales de Chimie Science des Materiaux* **26**, 99-106 (2001).

23. Ye, Z.-G. Crystal chemistry and domain structure of relaxor piezocrystals. *Curr. Opin. Solid State Mater. Sci.* **6**, 35-44 (2002).

24. IEEE standard on piezoelectricity. ANSI/IEEE Std 176-1987, 54. 1-29-1988. Inst. Electr. & Electron. Eng., New York, NY, USA.

25. B.Jaffe, W.R.Cook & H.Jaffe *Piezoelectric Ceramics*. London and New York (1971).

26. Berlincourt, D. & Krueger, H. H. A. Domain processes in lead titanate zirconate and barium titanate ceramics. *J. Appl. Phys.* **30**, 1804-1810 (1959).

27. Aizu, K. Possible species of ferromagnetic, ferroelectric and ferroelastic crystals. *Phys. Rev. B* **2**, 754-772 (1970).

28. Nye, J. F. *Physcical properties of crystals: their representation by tensors and matrices*. Oxford University Press, Oxford, London (1967).

29. Fujishiro, K. *et al.* Optical observation of heterophase and domain structures in relaxor ferroelectrics $Pb(Zn_{1/3}Nb_{2/3})O_3$-9%$PbTiO_3$. *Jpn. J. Appl. Phys. , Part 1* **37**, 5246-5248 (1998).

30. Uesu, Y. *et al.* Structural and optical studies of development of the long-range order in ferroelectric relaxor $Pb(Zn_{1/3}Nb_{2/3})O_3$-9%$PbTiO_3$. *Ferroelectrics* **217**, 319-325 (1998).

31. Ye, Z.-G., Dong, M. & Zhang, L. Domain structure and phase transitions in relaxor-based piezo-/ferroelectric (1-x)$Pb(Zn_{1/3}Nb_{2/3})O_3$-x$PbTiO_3$ single crystals. *Ferroelectrics* **229**, 223-232 (1999).

32. Zhang, L., Dong, M. & Ye, Z.-G. Flux growth and characterization of the relaxor-based $Pb[(Zn_{1/3}Nb_{2/3})_{1-x}Ti_x]O_3$ [PZNT] piezocrystals. *Mat. Sci. Eng. B* **78**, 96-104 (2000).

33. Noheda, B. *et al.* Polarization rotation via a monoclinic phase in the piezoelectric 92%$Pb(Zn_{1/3}Nb_{2/3})O_3$-8%$PbTiO_3$. *Phys. Rev. Lett.* **86**, 3891-3894 (2001).

34. Lu, Y. *et al.* Phase transitional behavior and piezoelectric properties of the orthorhombic phase of $Pb(Mg_{1/3}Nb_{2/3})O_3$-$PbTiO_3$ single crystals. *Appl. Phys. Lett.* **78**, 3109-3111 (2001).

35. Cox, D. E. *et al.* Universal phase diagram for high-piezoelectric perovskite systems. *Appl. Phys. Lett.* **79**, 400-402 (2001).

36. Noheda, B. *et al.* Stability of the monoclinic phase in the ferroelectric perovskite $PbZr_{1-x}Ti_xO_3$. *Phys. Rev. B* **63**, 1-6 (2001).

37. Ye, G., Noheda, B., Dong, M., Cox, D. & Shirane, G. Monoclinic phase in the relaxor-based piezoelectric/ferroelectric $Pb(Mg_{1/3}Nb_{2/3})O_3$-$PbTiO_3$ system. *Phys. Rev. B* **64**, 184114 (2001).

38. Noheda, B. Structure and high-piezoelectricity in lead oxide solid solutions. *Curr. Opin. Solid State Mater. Sci.* **6**, 27-34 (2002).

39. Akhilesh, K. S., Dhananjai, P. & Oksana, Z. Confirmation of M_B-type monoclinic phase in $Pb[(Mg_{1/3}Nb_{2/3})_{0.71}Ti_{0.29}]O_3$: A powder neutron diffraction study. *Phys. Rev. B* **68**, 172103 (2003).

40. Akhilesh, K. S. & Dhananjai, P. Evidence for M_B and M_C phases in the morphotropic phase boundary region of (1 - x)$Pb(Mg_{1/3}Nb_{2/3})O_3$-x$PbTiO_3$: A Rietveld study. *Phys. Rev. B* **67**, 064102 (2003).

41. Bai, F. *et al.* X-ray and neutron diffraction investigation of the structural phase transformation sequence under electric field in $0.7Pb(Mg_{1/3}Nb_{2/3})O_3$-$0.3PbTiO_3$ crystals. *cond-mat* 0402296 (2004).

42. La Orauttapong, D. *et al.* Phase diagram of the relaxor ferroelectric (1 - x)$Pb(Zn_{1/3}Nb_{2/3})O_3$-x$PbTiO_3$. *Phys. Rev. B* **65**, 144101 (2002).

43. Noheda, B., Cox, D. E., Shirane, G., Gao, J. & Ye, G. Phase diagram of the ferroelectric relaxor (1 - x)$Pb(Mg_{1/3}Nb_{2/3})O_3$-x$PbTiO_3$ crystals. *Phys. Rev. B* **66**, 054104 (2002).

44. Yin, J., Jiang, B. & Cao, W. Elastic, piezoelectric, and dielectric properties of $0.955Pb(Zn_{1/3}Nb_{2/3})O_3$-$0.045PbTiO_3$ single crystal with designed multidomains. *IEEE T. Ultrason. Ferr.* **47**, 285-291 (2000).

45. Zhang, R., Jiang, B. & Cao, W. Elastic, piezoelectric, and dielectric properties of multidomain $0.67Pb(Mg_{1/3}Nb_{2/3})O_3$-$0.33PbTiO_3$ single crystals. *J. Appl. Phys.* **90**, 3471-3475 (2001).

46. Zeng, H. R. *et al.* Domain orientation imaging of PMN-PT single crystals by vertical and lateral piezoresponse force microscopy. *J. Cryst. Growth* **267**, 194-198 (2004).

47. Jin, L., Xi, Z., Xu, Z. & Yao, X. Study of ferroelectric domain morphology in PMN-32% PT single crystals. *Ceram. Int.* **30**, 1695-1698 (2004).

48. Munoz-Saldana, J., Schneider, G. A. & Eng, L. M. Stress induced movement of ferroelastic domain walls in $BaTiO_3$ single crystals evaluated by scanning force microscopy. *Surf. Sci.* **480**, 402-410 (2001).

49. Yu, H. & Randall, C. A. Dendritic domain configurations in $Pb(Zn_{1/3}Nb_{2/3})O_3$-$PbTiO_3$ single crystals. *J. Appl. Phys.* **86**, 5733-5738 (1999).

50. Yu, H., Gopalan, V., Sindel, J. & Randall, C. A. Domain switching and electromechanical properties of pulse poled $Pb(Zn_{1/3}Nb_{2/3})O_3$-$PbTiO_3$ crystals. *J. Appl. Phys.* **89**, 561-567 (2001).

51. Ozgul, M. Polarization switching and fatigue anisotropy in relaxor-lead titanate ferroelectric single crystals, Ph.D. Dissertation. 2003. The Pennsylvania State University.

52. Liu, T. & Lynch, C. S. Ferroelectric properties of [110], [001] and [111] poled relaxor single crystals: measurements and modeling. *Acta Mater.* **51**, 407-416 (2003).

53. M.E.Lines & A.M.Glass *Principles and Applications of Ferroelectrics and Related Materials.* Clarendon Press, Oxford (1977).

54. Yin, J. & Cao, W. Coercive field of $0.955Pb(Zn_{1/3}Nb_{2/3})O_3$-$0.045PbTiO_3$ single crystal and its frequency dependence. *Appl. Phys. Lett.* **80**, 1043 (2002).

55. Mauck, L. D. The role of rate dependence and dissipation in the constitutive behavior of ferroelectric ceramics for high power applications, Ph.D. Dissertation. 2002. The Georgia Institute of Technology.

56. Mukherjee, B. K., Ren, W., Liu, S. F., Masys, A. J., & Yang, G. Non-linear properties of piezoelectric ceramics. *Proceedings of SPIE - The International Society for Optical Engineering* **4333**, 41-54 (2001).

57. Ujiie, R. & Uchino, K. Dynamical domain observation in relaxor ferroelectrics. *Ultrasonics Symposium Proceedings* **2**, 725-728 (1990).

58. Lynch, C. S. The effect of uniaxial stress on the electro-mechanical response of 8/65/35 PLZT. *Acta Mater.* **44**, 4137-4148 (1996).

59. Liu, S. F., Park, S. E., Shrout, T. R. & Cross, L. E. Electric field dependence of piezoelectric properties for rhombohedral $0.955Pb(Zn_{1/3}Nb_{2/3})O_3$-$0.045PbTiO_3$ single crystals. *J. Appl. Phys.* **85**, 2810 (1999).

60. Takemura, K., Ozgul, M., Bornand, V., Troller-McKinstry, S. & Randall, C. A. Fatigue anisotropy in single crystal $Pb(Zn_{1/3}Nb_{2/3})O_3$-$PbTiO_3$. *J. Appl. Phys.* **88**, 7272-7277 (2000).

61. Bornand, V., Trolier-McKinstry, S., Takemura, K. & Randall, C. A. Orientation dependence of fatigue behavior in relaxor ferroelectric-$PbTiO_3$ thin films. *J. Appl. Phys.* **87**, 3965-3972 (2000).

62. Ozgul, M., Takemura, K., Trolier-McKinstry, S. & Randall, C. A. Polarization fatigue in $Pb(Zn_{1/3}Nb_{2/3})O_3$-$PbTiO_3$ ferroelectric single crystals. *J. Appl. Phys.* **89**, 5100-5106 (2001).

63. Viehland, D., Amin, A. & Li, J. F. Piezoelectric instability in <011>-oriented $Pb(B_{1/3}^{I}B_{2/3}^{II})O_3$-$PbTiO_3$ crystals. *Appl. Phys. Lett.* **79**, 1006-1008 (2001).

64. Cao, H., Fang, B., Xu, H. & Luo, H. Crystal orientation dependence of dielectric and piezoelectric properties of tetragonal $Pb(Mg_{1/3}Nb_{2/3})O_3$-38%$PbTiO_3$ single crystal. *Mater. Res. Bull.* **37**, 2135-2143 (2002).

65. Ren, W., Liu, S. F. & Mukherjee, B. K. Piezoelectric properties and phase transitions of <001>-oriented $Pb(Zn_{1/3}Nb_{2/3})O_3$-$PbTiO_3$ single crystals. *Appl. Phys. Lett.* **80**, 3174 (2002).

66. Fu, H. & Cohen, R. E. Polarization rotation mechanism for ultrahigh electromechanical response in single-crystal piezoelectrics. *Nature* **403**, 281-283 (2000).

67. Viehland, D. Symmetry-adaptive ferroelectric mesostates in oriented $Pb(BI_{1/3}BII_{2/3})O_3$-$PbTiO_3$ crystals. *J. Appl. Phys.* **88**, 4794-4806 (2000).

68. Krueger, H. H. A. & Berlincourt, D. Effects of high static stress on the piezoelectric properties of transducer materials. *J. Acoust. Soc. Am.* **33**, 1339-1344 (1961).

69. Krueger, H. H. A. Stress sensitivity of piezoelectric ceramics: Part 1. Sensitivity to compressive stress parallel to the polar axis. *J. Acoust. Soc. Am.* **42**, 636-645 (1967).

70. Krueger, H. H. A. Stress sensitivity of piezoelectric ceramics: Part 3. Sensitivity to compressive stress perpendicular to the polar axis. *J. Acoust. Soc. Am.* **43**, 583-591 (1968).

71. Meeks, S. W. & Timme, R. W. Effects of one-dimensional stress on piezoelectric ceramics. *J. Appl. Phys.* **46**, 4334-4338 (1975).

72. Cao, H. & Evans, A. G. Nonlinear deformation of ferroelectric ceramics. *J. Am. Ceram. Soc.* **76**, 890-896 (1993).

73. Schaufele, A. B. & Hardtl, K. H. Ferroelastic properties of lead zirconate titanate ceramics. *J. Am. Ceram. Soc.* **79**, 2637-2640 (1996).

74. Stoll, W. A. & Lynch, C. S. Experimental measurements of electro-mechanical constitutive behavior of four compositions of PZT. *ISAF '96. Proceedings of the Tenth IEEE International Symposium on Applications of Ferroelectrics (Cat. No.96CH35948)* **2**, 911-914 (1996).

75. Chaplya, P. M. & Carman, G. P. Compression of piezoelectric ceramic at constant electric field: Energy absorption through non-180 degrees domain-wall motion. *J. Appl. Phys.* **92**, 1504-1510 (2002).

76. Samara, G. A., Venturini, E. L. & Schmidt, V. H. Pressure-induced crossover from long-to-short-range order in $[Pb(Zn_{1/3}Nb_{2/3})O_3]_{0.905}$-$(PbTiO_3)_{0.095}$ single crystal. *Appl. Phys. Lett.* **76**, 1327-1329 (2000).

77. Viehland, D. & Powers, J. Electromechanical coupling coefficient of <001>-oriented $Pb(Mg_{1/3}Nb_{2/3})O_3$-$PbTiO_3$ crystals: Stress and temperature independence. *Appl. Phys. Lett.* **78**, 3112-3114 (2001).

78. Viehland, D. & Powers, J. Effect of uniaxial stress on the electromechanical properties of $0.7Pb(Mg_{1/3}Nb_{2/3})O_3$-$0.3PbTiO_3$ crystals and ceramics. *J. Appl. Phys.* **89**, 1820-1825 (2001).

79. Shang, J. K. & Tan, X. Indentation-induced domain switching in $Pb(Mg_{1/3}Nb_{2/3})O_3$-$PbTiO_3$ crystal. *Acta Mater.* **49**, 2993-2999 (2001).

80. Fang, F. & Yang, W. Indentation-induced cracking and 90 degrees domain switching pattern in barium titanate ferroelectric single crystals under different poling. *Mater. Lett.* **57**, 198-202 (2002).

81. Lynch, C. S. On the development of multiaxial phenomenological constitutive laws for ferroelectric ceramics. *J. Intell. Mater. Syst. Struct.* **9**, 555-563 (1998).

82. Kamlah, M. & Tsakmakis, C. Phenomenological modeling of the non-linear electro-mechanical coupling in ferroelectrics. *Int. J. Solids Struct.* **36**, 669-695 (1999).

83. McMeeking, R. M. & Landis, C. M. A phenomenological multi-axial constitutive law for switching in polycrystalline ferroelectric ceramics. *Int. J. Eng. Sci.* **40**, 1553-1577 (2002).

84. Vanderbilt, D. & Cohen, M. H. Monoclinic and triclinic phases in higher-order Devonshire theory. *Phys. Rev. B* **63**, 094108 (2001).

85. Chen, W. & Lynch, C. S. A micro-electro-mechanical model for polarization switching of ferroelectric materials. *Acta Mater.* **46**, 5303-5311 (1998).

86. Chen, W. & Lynch, C. S. Model for simulating polarization switching and AF-F phase changes in ferroelectric ceramics. *J. Intell. Mater. Syst. Struct.* **9**, 427-431 (1998).

87. Landis, C. M., Wang, J., & Sheng, J. Micro-electromechanically Informed Phenomenological Constitutive Models for Ferroelectrics. *Proceedings of SPIE - The International Society for Optical Engineering* **5053**, 335-346 (2003).

88. Tadmor, E. B., Waghmare, U. V., Smith, G. S. & Kaxiras, E. Polarization switching in PbTiO3: an ab initio finite element simulation. *Acta Mater.* **50**, 2989-3002 (2002).

89. Su, C., Vugmeister, B. & Khachaturyan, A. G. Dielectric properties of material with random off-center defects: Monte Carlo simulation of relaxor ferroelectrics. *J. Appl. Phys.* **90**, 6345-6356 (2001).

90. Wang, X., Liu, M., Chan, L. W. & Choy, C. L. Monte Carlo simulation on dielectric and ferroelectric behaviors of relaxor ferroelectrics. *J. Appl. Phys.* **95**, 4282-4290 (2004).

91. Li, Y. L., Hu, S. Y., Liu, Z. K., & Chen, L. Q. Phase-field simulation of domain structure evolution in ferroelectric thin films. *Materials Research Society Symposium - Proceedings* **652**, 421-4210 (2001).

92. Yang, W. & Chen, L. Q. Computer simulation of the dynamics of 180° ferroelectric domains. *J. Am. Ceram. Soc.* **78**, 2554-2556 (1995).

93. Hu, H. L. & Chen, L. Q. Three-dimensional computer simulation of ferroelectric domain formation. *J. Am. Ceram. Soc.* **81**, 492-500 (1998).

94. Hu, H. L. & Chen, L. Q. Computer simulation of 90° ferroelectric domain formation in two-dimensions. *Mater. Sci. Eng. A* **A238**, 182-191 (1997).

95. Khachaturyan, A. G. Prospects of 3-dimensional nanoscale modeling of engineering materials. *Proceedings of the TMS Fall Meeting* 293-308 (2000).

96. Glinchuk, M. D. Relaxor ferroelectrics: From cross superparaelectric model to random field theory. *Br. Ceram. Trans.* **103**, 76-82 (2004).

97. Ghandi, K. & Hagood, N. W. Hybrid finite element model for phase transitions in nonlinear electromechanically coupled material. *Proceedings of SPIE - The International Society for Optical Engineering* **3039**, 97-112 (1997).

98. Hwang, S. C. & McMeeking, R. M. Finite element model of ferroelectric/ferroelastic polycrystals. *Proceedings of SPIE - The International Society for Optical Engineering* **3992**, 404-417 (2000).

99. Kessler, H., Kamlah, M., & Balke, H. Constitutive and finite element modeling of ferroelectric repolarization. *Proceedings of SPIE - The International Society for Optical Engineering* **4699**, 21-30 (2002).

100. Kim, S. J. Polarization switching of ferroelectric polycrystals: Finite element modeling and simulations. *Proceedings of SPIE - The International Society for Optical Engineering* **5053**, 387-394 (2003).

101. Landis, C. M. A new finite-element formulation for electromechanical boundary value problems. *Int. J. Numer. Methods Eng.* **55**, 613-628 (2002).

102. Li, F. & Fang, D. Simulations of domain switching in ferroelectrics by a three-dimensional finite element model. *Mech. Mater.* **36**, 959-973 (2004).

103. Hwang, S. C., Lynch, C. S. & McMeeking, R. M. Ferroelectric/ferroelastic interactions and a polarization switching model. *Acta Metall. Mater.* **43**, 2073-2084 (1995).

104. Huber, J. E., Fleck, N. A., Landis, C. M. & McMeeking, R. M. Constitutive model for ferroelectric polycrystals. *J. Mech. Phys. Solids* **47**, 1663-1697 (1999).

105. McMeeking, R. M. & Hwang, S. C. On the potential energy of a piezoelectric inclusion and the criterion for ferroelectric switching. *Ferroelectrics* **200**, 151-173 (1997).

106. Hom, C. L. & Shankar, N. A finite element method for electrostrictive ceramic devices. *Int. J. Solids Struct.* **33**, 1757-1779 (1996).

107. Essig, O. *et al.* Uniaxial stress and temperature dependence of field induced strains in antiferroelectric lead zirconate titanate stannate ceramics. *J. Eur. Ceram. Soc.* **19**, 1223-1228 (1999).

108. Chen, W. & Lynch, C. S. Finite element analysis of cracks in ferroelectric ceramic materials. *Eng. Fract. Mech.* **64**, 539-562 (1999).

109. Lucato, S. L. D. S., Lupascu, D. C., Kamilah, M., Rodel, J. & Lynch, C. S. Constraint-induced crack initiation at electrode edges in piezoelectric ceramics. *Acta Mater.* **49**, 2751-2759 (2001).

110. Wan, S. & Lynch, C. Crack growth of PZN crystals under cyclic electric field. *Proceedings of SPIE - The International Society for Optical Engineering* **4333**, 33-34 (2001).

111. Priya, S. *et al.* Modeling of fatigue behavior in relaxor piezocrystals: Improved characteristics by Mn substitution. *J. Appl. Phys.* **92**, 3923-3927 (2002).

112. Saitoh, S., Kobayashi, T., Harada, K., Shimanuki, S. & Yamashita, Y. Forty-channel phased array ultrasonic probe using $0.91Pb(Zn_{1/3}Nb_{2/3})O_3$-$0.09PbTiO_3$ single crystal. *IEEE T. Ultrason. Ferr.* **46**, 152-157 (1999).

113. Park, S. E., Lopath, P. D., Shung, K. K., & Shrout, T. R. Relaxor-based single-crystal materials for ultrasonic transducer applications. *Proceedings of SPIE - The International Society for Optical Engineering* **3037**, 140-147 (1997).

114. Jiang, W., Zhang, R., Jiang, B. & Cao, W. Characterization of piezoelectric materials with large piezoelectric and electromechanical coupling coefficients. *Ultrasonics* **41**, 55-63 (2003).

115. Dammak, H., Renault, A. E., Gaucher, P., Thi, M. P. & Calvarin, G. Origin of the giant piezoelectric properties in the [001] domain engineered relaxor single crystals. *Jpn. J. Appl. Phys. Part 1* **42**, 6477-6482 (2003).

116. Zhao, X. *et al.* Composition dependence of piezoelectric constant and dielectric constant tunability in the <001>-oriented $Pb(Mg_{1/3}Nb_{2/3})O_3$-$PbTiO_3$ single crystals. *Mater. Lett.* **58**, 2053-2056 (2004).

117. Chen, J., Panda, R., Beck, H., & Gururaja, R. New orientation cuts for enhanced electromechanical properties of PMN-PT and PZN-PT single crystals. *The Tenth US-Japan Seminar on dielectric and piezoelectric ceramics* 233-236 (2001).

118. Priya, S., Ryu, J., Cross, L. E., Uchino, K. & Viehland, D. Investigation of the ferroelectric orthorhombic phase in the $Pb(Zn_{1/3}Nb_{2/3})O_3$-$PbTiO_3$ system. *Ferroelectrics* **274**, 121-126 (2002).

119. Nosek, J. & Erhart, J. Some experimental investigations of electromechanical properties of $(PbZn_{1/3}Nb_{2/3}O_3)_{0.92}$-$(PbTiO_3)_{0.08}$ relaxor single crystals. *Microelectron. Eng.* **66**, 733-737 (2003).

120. Zhang, R., Jiang, B., Jiang, W. & Cao, W. Complete set of properties of $0.92Pb(Zn_{1/3}Nb_{2/3})O_3$-$0.08PbTiO_3$ single crystal with engineered domains. *Mater. Lett.* **57**, 1305-1308 (2003).

121. Barad, Y., Yu, L., Cheng, Y., Park, E. & Zhang, Q. M. Composition, temperature, and crystal orientation dependence of the linear electro-optic properties of $Pb(Zn_{1/3}Nb_{2/3})O_3$-$PbTiO_3$ single crystals. *Appl. Phys. Lett.* **77**, 1247-1249 (2000).

122. McLaughlin, E. A., Liu, T. & Lynch, C. S. Relaxor ferroelectric PMN-32%PT crystals under stress and electric field loading: I-32 mode measurements. *Acta Mater.* **52**, 3849-3857 (2004).

123. Uchino, K. Relaxor ferroelectric devices. *Ferroelectrics* **151**, 321-330 (1994).

124. Uchino, K. *Piezoelectric Actuators and Ultrasonic Motors*. Kluwer Academic Publishers, Boston (1996).

125. Kobayashi, T., Saitoh, S., Harada, K., Shimanuki, S. & Yamashita, Y. Growth of large and homogeneous PZN-PT single crystals for medical ultrasonic array transducers. *IEEE International Symposium on Applications of Ferroelectrics* 235-238 (1998).

126. Hackenberger, W., Rehrig, P., Pan, M. J., & Shrout, T. Single crystal piezoelectrics for advanced transducer and smart structures applications. *Proceedings of SPIE - The International Society for Optical Engineering* **4333**, 92-103 (2001).

127. Powers, J. M., Moffett, M. B., & Nussbaum, F. Single crystal naval transducer development. *IEEE International Symposium on Applications of Ferroelectrics* **1**, 351-354 (2000).

128. Gururaja, T. R., Panda, R. K., Chen, J., & Beck, H. Single crystal transducers for medical imaging applications. *Proceedings of the IEEE Ultrasonics Symposium* **2**, 969-972 (1999).

129. Harada, K., Shimanuki, S., Kobayashi, T., Saitoh, S. & Yamashita, Y. Growth of $Pb[(Zn_{1/3}Nb_{2/3})_{0.91}Ti_{0.09}]O_3$ single crystal of ultrasonic transducer for medical application. *J. Intell. Mater. Syst. Struct.* **10**, 493-497 (2000).

130. Lu, Y., Jeong, D. Y., Cheng, Z. Y., & Zhang, Q. M. A new kind of ultrasonic transducer for medical imaging by combining electromechanical and optical properties of PZN-PT single crystal. *Conference on Lasers and Electro-Optics Europe - Technical Digest* 309-310 (2001).

131. Zhao, X., Fang, B., Cao, H., Guo, Y. & Luo, H. Dielectric and piezoelectric performance of PMN-PT single crystals with compositions around the MPB: Influence of composition, poling field and crystal orientation. *Mat. Sci. Eng. B* **96**, 254-262 (2002).

132. Lu, Y., Jeong, D. Y., Cheng, Z. Y., Shrout, T. & Zhang, Q. M. Phase stabilities of "morphotropic" phases in $Pb(Zn_{1/3}Nb_{2/3})O_3$-$PbTiO_3$ single crystals. *Appl. Phys. Lett.* **80**, 1918 (2002).

133. Singh, A. K. & Pandey, D. Evidence for M_B and M_C phases in the morphotropic phase boundary region of (1- x)$[Pb(Mg_{1/3}Nb_{2/3})O_3]$-x$PbTiO_3$: A Rietveld study. *Phys. Rev. B* **67**, 064102 (2003).

134. Ye, Z.-G. & Dong, M. Morphotropic domain structures and phase transitions in relaxor-based piezo-/ferroelectric (1- x)$Pb(Mg_{1/3}Nb_{2/3})O_3$-x$PbTiO_3$ single crystals. *J. Appl. Phys.* **87**, 2312-2319 (2000).

135. Belegundu, U., Du, X. H., Cross, L. E. & Uchino, K. In situ observation of domains in 0.9$Pb(Zn_{1/3}Nb_{2/3})O_3$-0.1$PbTiO_3$ single crystals. *Ferroelectrics* **221**, 67-71 (1999).

136. Bertram, R., Reck, G. & Uecker, R. Growth and correlation between composition and structure of (1-x)$Pb(Zn_{1/3}Nb_{2/3})O_3$-x$PbTiO_3$ crystals near the morphotropic phase boundary. *J. Cryst. Growth* **253**, 212-220 (2003).

137. Chen, K.-P., Zhang, X.-W. & Luo, H.-S. Electric-field-induced phase transition of <001> oriented $Pb(Mg_{1/3}Nb_{2/3})O_3$-$PbTiO_3$ single crystals. *J. Phys. : Condens. Matter* **14**, 571-576 (2002).

138. Viehland, D. & Li, J. F. Anhysteretic field-induced rhombhohedral to orthorhombic transformation in <110>-oriented 0.7$Pb(Mg_{1/3}Nb_{2/3})O_3$-0.3$PbTiO_3$ crystals. *J. Appl. Phys.* **92**, 7690-7692 (2002).

139. Viehland, D., Li, J. F., Gittings, K. & Amin, A. Electroacoustic properties of <110>-oriented $Pb(Mg_{1/3}Nb_{2/3})O_3$-$PbTiO_3$ crystals under uniaxial stress. *Appl. Phys. Lett.* **83**, 132-134 (2003).

140. Tu, C.-S., Shih, I. C., Schmidt, V. H. & Chien, R. E-field-induced polarization rotation in $Pb(Mg_{1/3}Nb_{2/3})_{1-x}Ti_xO_3$ crystal. *Appl. Phys. Lett.* **83**, 1833-1835 (2003).

141. Tu, C. S., Tsai, C. L., Chen, J. S. & Schmidt, V. H. Orientation dependence and electric-field effect in the relaxor-based ferroelectric crystal $(PbMg_{1/3}Nb_{2/3}O_3)_{0.68}(PbTiO_3)_{0.32}$. *Phys. Rev. B* **65**, 104113 (2002).

142. Han, J. & Cao, W. Electric field effects on the phase transitions in [001]-oriented (1 - x)$Pb(Mg_{1/3}Nb_{2/3})O_3$-x$PbTiO_3$ single crystals with compositions near the morphotropic phase boundary. *Phys. Rev. B* **68**, 134102-134106 (2003).

143. Asamitsu, A., Moritomo, Y., Tomioka, Y., Arima, T. & Tokura, Y. A structural phase transition induced by an external magnetic field. *Nature* **373**, 407-409 (1995).

144. Fiebig, M., Lottermoser, T., Frohlich, D., Goltsev, A. V. & Pisarev, R. V. Observation of coupled magnetic and electric domains. *Nature* **419**, 818-820 (2002).

145. Li, W., Guo, S., Tang, Y. & Zhao, X. Phase transition induced by thermal and electric fields in electron-irradiated poly (vinylidene fluoride-trifluoroethylene) copolymers. *J. Phys. D: Appl. Phys.* **36**, 2382-2385 (2003).

146. Allen, R. E. Structural phase transitions in solids with applied stresses and fields, and effect of isotopic impurities on the free energy. *J. Chem. Phys.* **64**, 552-553 (1976).

147. George, A. M., Iniguez, J. & Bellaiche, L. Anomalous properties in ferroelectrics induced by atomic ordering. *Nature* **413**, 54-57 (2001).

148. Feng, Z., Luo, H., Guo, Y., He, T. & Xu, H. Dependence of high electric-field-induced strain on the composition and orientation of $Pb(Mg_{1/3}Nb_{2/3})O_3$-$PbTiO_3$ crystals. *Solid State Commun.* **126**, 347-351 (2003).

149. Xu, G., Luo, H., Xu, H. & Yin, Z. Third ferroelectric phase in PMNT single crystals near the morphotropic phase boundary composition. *Phys. Rev. B* **64**, 020102 (2001).

150. Schmidt, V. H., Chien, R., Shih, I. C. & Tu, C.-S. Polarization rotation and monoclinic phase in relaxor ferroelectric PMN-PT crystal. *AIP Conf. Proc.* **677**, 160-167 (2003).

151. Tu, C.-S., Huang, L. W., Chien, R. & Schmidt, V. H. E-field and temperature dependent transformation in <102>-cut PMN-PT crystal. *AIP Conf. Proc.* **677**, 152-159 (2003).

152. Yin, J., Jiang, B., & Cao, W. Determination of elastic, piezoelectric and dielectric properties of $Pb(Zn_{1/3}Nb_{2/3})O_3$-$PbTiO_3$ single crystals. *Proceedings of SPIE - The International Society for Optical Engineering* **3664**, 239-246 (1999).

153. Yin, J., Jiang, B. & Cao, W. Elastic, piezoelectric, and dielectric properties of $0.955Pb(Zn_{1/3}Nb_{2/3})O_3$-$0.045PbTiO_3$ single crystal with designed multidomains. *IEEE T. Ultrason. Ferr.* **47**, 285-291 (2000).

154. Damjanovic, D., Budimir, M., Davis, M. & Setter, N. Monodomain versus polydomain piezoelectric response of $0.67Pb(Mg_{1/3}Nb_{2/3})O_3$-$0.33PbTiO_3$ single crystals along nonpolar directions. *Appl. Phys. Lett.* **83**, 527-529 (2003).

155. Priya, S., Jungho, R., Uchino, K. & Viehland, D. Mechanical aging behavior of oriented $Pb(Mg_{1/3}Nb_{2/3})O_3$-$PbTiO_3$ and $Pb(Zn_{1/3}Nb_{2/3})O_3$-$PbTiO_3$ single crystals. *Appl. Phys. Lett.* **79**, 2624-2626 (2001).

156. Shur, V. Y., Rumyantsev, E., Nikolaeva, E., Shishkin, E., Baturin, I., Shur, A., Lupascu, D. C., Randall, C., & Ozgul, M. Fatigue effect in bulk ferroelectrics. *Proceedings of SPIE - The International Society for Optical Engineering* **4699**, 40-50 (2002).

157. Ozgul, M., Trolier-McKinstry, S. & Randall, C. A. Influence of electrical cycling on polarization reversal processes in $Pb(Zn_{1/3}Nb_{2/3})O_3$-$PbTiO_3$ ferroelectric single crystals as a function of orientation. *J. Appl. Phys.* **95**, 4296-4302 (2004).

158. Ozgul, M., Furman, E., Trolier-McKinstry, S. & Randall, C. A. Polarization relaxation anisotropy in $Pb(Zn_{1/3}Nb_{2/3})O_3$-$PbTiO_3$ single-crystal ferroelectrics as a function of fatigue history. *J. Appl. Phys.* **95**, 2631-2638 (2004).

159. Tan, X., Xu, Z., Shang, J. K. & Han, P. Direct observations of electric field-induced domain boundary cracking in <001> oriented piezoelectric $Pb(Mg_{1/3}Nb_{2/3})O_3$-$PbTiO_3$ single crystal. *Appl. Phys. Lett.* **77**, 1529-1531 (2000).

160. Yin, J. & Cao, W. Effective macroscopic symmetries and materials properties of multidomain $0.955Pb(Zn_{1/3}Nb_{2/3})O_3$-$0.045PbTiO_3$ single crystals. *J. Appl. Phys.* **92**, 444 (2002).

161. Liu, T. & Lynch, C. S. Crystal Variant Based Modeling of Relaxor Single Crystals. *Proceedings of SPIE - The International Society for Optical Engineering* **5053**, 347-356 (2003).

162. Viehland, D., Ewart, L., Powers, J. & Li, J. F. Stress dependence of the electromechanical properties of <001>-oriented $Pb(Mg_{1/3}Nb_{2/3})O_3$-$PbTiO_3$ crystals: Performance advantages and limitations. *J. Appl. Phys.* **90**, 2479-2483 (2001).

163. McLaughlin, E. A., Liu, T. & Lynch, C. S. Relaxor ferroelectric PMN-32%PT crystals under stress and electric field loading II - 33 mode measurements. (submitted for publication) (2004).

164. Aburatani, H., Harada, S., Uchino, K., Furuta, A. & Fuda, Y. Destruction mechanisms in ceramic multilayer actuators. *Jpn. J. Appl. Phys. Part 1* **33**, 3091-3094 (1994).

165. Furuta, A. & Uchino, K. Dynamic observation of crack propagation in piezoelectric multilayer actuators. *J. Am. Ceram. Soc.* **76**, 1615-1617 (1993).

166. Aburatani, H., Harada, S., Uchino, K., Furuta, A. & Fuda, Y. Destruction mechanisms in ceramic multilayer actuators. *Jpn. J. Appl. Phys. Part 1* **33**, 3091-3094 (1994).

167. Suo, Z. Models for breakdown-resistant dielectric and ferroelectric ceramics. *J. Mech. Phys. Solids* **41**, 1155-1176 (1993).

168. Hao, T. H., Gong, X. & Suo, Z. Fracture mechanics for the design of ceramic multilayer actuators. *J. Mech. Phys. Solids* **44**, 23-48 (1996).

169. Gong, X. & Suo, Z. Reliability of ceramic multilayer actuators: a nonlinear finite element simulation. *J. Mech. Phys. Solids* **44**, 751-769 (1996).